Towards experimentation at a Future Linear Collider

R. Pöschl

ORSAY
n° d'ordre:

LAL 10-08
Février 2010

UNIVERSITÉ PARIS XI - LABORATOIRE DE L'ACCÉLÉRATEUR LINÉAIRE

Mémoire d'Habilitation à Diriger des Recherches

par

Roman PÖSCHL

Towards Experimentation at a Future Linear Collider

soutenu le 22 Février 2010

Jury :

Président :	Dr. Guy WORMSER	-	LAL Orsay
Rapporteurs :	Prof. Dr. Joachim MNICH	-	DESY Hambourg
	Dr. Claude VALLÉE	-	CPPM Marseille
	Dr. Marc WINTER	-	IPHC Strasbourg
Examinateurs :	Dr. Jean-Claude BRIENT	-	LLR Palaiseau
	Dr. Laurent SERIN	-	LAL Orsay

Abstract

This document highlights aspects of the research program for a future linear electron positron collider enabling precision physics at the TeV scale where phenomena reaching beyond the Standard Model of particle physics are expected to appear. The most advanced proposal for such a machine is the International Linear Collider (ILC) which is designed for centre-of-mass energies between 90 GeV and 1 TeV. Earlier precision measurements suggest the existence of the Higgs boson with a mass of around 120 GeV. Employing nominal parameters on beam characteristics and luminosity, the ILC promises to arrive at a precision of 2-3% on the Higgs-strahlung cross section and of around 30 MeV on the mass of the Higgs boson. The detectors to be operated at the ILC will feature highly granular calorimeters. This new type of calorimeters is the main tool to achieve the envisaged jet energy resolution of $30\%/\sqrt{E}$. The electromagnetic calorimeter will use tungsten as absorber material and it is currently favoured to employ silicon diodes as the active material. The document describes details of the successful R&D program for this calorimeter in terms of mechanics and the development of the read out electronics which will be interleaved with the calorimeter layers. The status of the development of the silicon wafers is outlined as well. The results obtained in beam test campaigns with a first prototype confirm the parameters employed in the studies for the Letter of Intent published in 2009 by the detector concept group ILD.

Résumé

Ce mémoire accentue des aspects du programme de recherche pour un futur collisionneur linéaire des électrons et positrons permettant de faire de la physique de précision à l'echelle de TeV où l'apparition des phénomènes au-delà du Modèle Standard de la physique de particules est attendue. La proposition la plus mature pour une telle machine est l'*International Linear Collider* (ILC) conçue pour des énergies dans le centre de masse entre 90 GeV et 1 TeV. Les résultats obtenus avec des expériences de précision précédentes suggèrent l'existence du boson de Higgs ayant une masse d'environ 120 GeV. En assumant des paramètres nominaux pour les faisceaux et la luminosité, l'ILC est prometteur d'atteindre une précision de 2-3% sur la section efficace de la Higgs-strahlung et d'environ 30 MeV sur la masse du boson de Higgs. Les détecteurs qui seront opérés au sein de l'ILC comprendront des calorimètres à haute granularité. Ce nouveau type de calorimètre constitue l'outil principal pour atteindre une résolution en énergie des jets de $30\%/\sqrt{E}$. Le calorimètre électromagnétique sera composé par tungstène comme matériel absorbant et il est actuellement favorisé d'employer des diodes de silicium comme matériel actif. Le document décrit des détails du programme de R&D pour ce calorimètre par rapport à la mécanique et du développement de l'électronique frontale qui sera integrée dans les couches du calorimètre. En plus, l'état actuel du développement des galettes de silicium est abordé. Les résultats obtenus dans les campagnes de test en faisceau avec un premier prototype confirment les paramètres appliqués dans les études de la "Letter of Intent" publiée par le groupe de concept ILD en 2009.

Remerciements

Je voudrais remercier tout le personnel du Laboratoire de l'Accélérateur Linéaire (LAL) à Orsay ainsi que le Directeur Dr. Guy Wormser à sa tête. Les conditions opimales de travail dont je bénéfice depuis maintenant 6 ans forment la base pour en être arriver ici. Je profite de la collaboration et du soutien de tous les services disponibles au LAL.

Je souhaite remercier les Prof. Dr. Joachim Mnich, Dr. Marc Winter et Dr. Claude Vallée pour avoir pris le temps d'être rapporteurs de ce mémoire. Je voudrais également remercier le Dr. Jean-Claude Brient et le Dr. Laurent Serin en tant qu'examinateurs de la soutenance de mon habilitation.

Je ne serais pas arrivé à ce jour-ci sans le soutien, les conseils professionnels et amicaux du Dr. Françcois Richard. Sans nombre sont les petits quarts d'heure dans son bureau qui m'ont permis de m'orienter dans la bonne direction et de prendre des décisions et mesures adaptées. Il m'a convaincu avec le Dr. Philippe Bambade de rejoindre le groupe ILC au LAL et je tiens à dire que je n'ai jamais regretté cette decision pas facile à l'époque. Une pensée pour Dr. Vincent Lepeltier, décédé en 2008, le groupe leader qui m'a laissé toute la liberté d'évoluer au sein du groupe ILC. Son successeur, Dr. Fabian Zomer, m'a donné de la confiance pour diriger la partie "Physique et Détecteur" des activités ILC au LAL. Avant de rejoindre le groupe ILC du LAL, j'avais déjà le plaisir de travailler avec le Prof. Dr. Jean-Claude Bizot et Dr. Christian Pascaud au sein du groupe H1 du LAL.

Je voudrais remercier le Dr. Michele Faucci-Giannelli et encore le Dr. François Richard pour la lecture des passages de mon mémoire avec un esprit critique. Je suis un peu fier de voir évoluer les (ex-)étudiants Philippe Doublet, Dr. Hengne Li et Dr. Manqi Ruan. J'avais et j'ai toujours l'honneur de les accompagner un peu sur leur parcours professionnel.

La collaboration CALICE donne un exemple exceptionnel pour un travail commun et sans frontières. Je suis toujours convaincu de cette idée non-habituelle d'établir des collaborations déjà pendant la phase R&D d'un projet. Ce mémoire est aussi l'occasion de remercier tous mes collègues, chercheurs et ingénieurs avec lesquels j'ai le plaisir de collaborer. Je suis très reconnaissant aux porte-parole de CALICE, Dr. Jean-Claude Brient et Dr. Felix Sefkow de m'avoir confié des responsabilités importantes dans cette collaboration internationale.

Enfin merci à ma petite famille Diana et Luis, merci de votre amour et d'être là. Mes parents Rosemarie et Herbert Pöschl, même si loin, sont toujours dans mon cœur.

Je suis fier d'être votre mari, beau-père et fils.

Orsay, le 22 Février 2010

Contents

Prologue

In science, the gain of knowledge is a fascinating interplay between precise experiments and theoretical conclusions. A nice example for this interplay is the development of the laws of the celestial motion of planets by Johannes Kepler at the end of the 16th Century. He interpreted the wealth of information collected by Tycho Brahe in his observatory and deduced from that his famous Kepler laws. Around the same time, the first telescopes allowed Galileo Galilei, and again Kepler, the discovery of the moons of Jupiter. All these observations and calculations supported strongly the heliocentric system with the sun as the central body. Even if these examples are not directly related to the topic covered in this document, they illustrate the importance of an excellent experimental apparatus and of independent thinking which mutually benefit from each other. The discovery of new fundamental laws of nature can change the way of thinking of a society. The list of successful interplays between experiment, observation and theory is of course much, much longer than the initial examples given here.

During the 20th century, physics has made an enormous progress in understanding the fundamental laws of nature. In terms of the microcosm, the main conclusions are summarised in the Standard Model of particle physics. It states that all matter can be built from twelve particles and their anti-particles. The interaction between these particles can be explained by the existence of four forces. The establishment of the Standard Model is largely based on experiments with particle accelerators with energies of up to several 100 GeV and the correct interpretation of the data. A missing piece of the Standard Model is the so-called Higgs boson. It is assumed that particles acquire mass by their interaction with the Higgs boson. Its discovery is one of the main motivations for the construction of the Large Hadron Collider, LHC, which started data taking in 2008 and collides beams of protons at a centre-of-mass energy of up to 14 TeV. It is a world wide consensus, that the next machine after the LHC will be a linear electron positron collider. Today, the most advanced proposal for such a machine is the International Linear Collider (ILC) which is designed for centre-of-mass energies between 90 GeV and 1 TeV. While it will not reach as high energies as the LHC, it promises results with higher precision than the LHC.

I always consider it as a privilege to work in science and in particular in the field of particle physics. One topic which fascinates me since long is the tight interplay between symmetries and fundamental laws of nature. My studies of physics at the University of Dortmund motivated me to investigate Quantum Chromodynamics and I got the opportunity to join the H1 Collaboration at DESY in 1994. My service work for the experiment in software and hardware concerned the installation, the maintenance and the event reconstruction of the backward calorimeter of the H1 collaboration, called SpaCal. As physics studies, I measured dijet cross sections and could show their sensitivity to the momentum distribution of the constituents of

the proton. During my first PostDoc at LAL, I have worked on the Level 2 Trigger of the H1 Trigger system at LAL Orsay. After the end of this PostDoc term, I switched subject and joined the R&D effort for the physics and the detectors of the ILC. My work at and with DESY gave me a natural proximity to the project. As a DESY Fellow, I have joined the ILC effort in 2003 for two reasons. One reason is the outstanding potential for the discovery and understanding of new physics. On the other hand, I saw the opportunity to have a sizable impact on the project as many items of the project were not and are still not finally decided. One of these items is the positron source. I joined the E166 experiment at SLAC which had as the aim to demonstrate the production of polarised positrons with an helical undulator. The comparitively small size of the experiment ($\sim$30 collaborators) offered one of the rare occasions today in particle physics to follow an experiment from the "cradle to the grave", meaning from the conceptual stages to the results which rendered the proof of polarised positron production with an helical undulator.

The calorimeters at the ILC will be particularly challenging. The envisaged precision at the ILC requires an extreme high longitudinal and lateral segmentation of the calorimeters. My "history" and my experience which I had with work on calorimeters motivated me to work on this challenging R&D effort. I started to work on this subject already during my term as a DESY Fellow and continued after my return to LAL in 2006. As outlined above, the Higgs boson will be central to the discovery of new physics. Therefore, I have conducted and supervised a study of Higgs boson production at the ILC. Nevertheless, I am also still in the phase of learning a lot on the physics of the Higgs boson. This document is also an expression of this phase of ongoing studying.

Parallel to my direct work in research, I consider it very important to form students and thus to teach on the subjects I am working on. My teaching activities comprised classes at universities for graduate students as well as invited lectures at international graduate schools. Moreover, I have supervised stages of students, a diploma thesis and meanwhile three PhD theses. The contact with students and the need to well explain complicated topics and to guide them in the sometimes complicated environment of large international collaborations constitutes an essential part of my work.

This document describes steps towards the experimental program of the ILC in which I am involved as member of the FLC group of LAL since 2006. This is namely:

- Detector R&D for a silicon tungsten electromagnetic calorimeter, SiW Ecal, within the CALICE collaboration. This R&D I have conducted either as software coordinator of CALICE, the responsible of beam test data taking or as the coordinator of the SiW Ecal project. Currently, I am responsible for the realisation of a technological prototype and got entrusted with the technical coordination of the CALICE collaboration as a whole.

- Optimisation of the ILD detector by a simulation study of Higgs Boson production at the ILC. The study presented here did become one of the most

important results of the Letter of Intent of the ILD detector.

The document starts with a review of important results obtained in the past decades in particle physics and an introduction to the physics of the Higgs boson. These chapters are mainly motivated by the arguments given at the beginning of this prologue, namely to underline the interconnection between precise experiment and correct interpretation of the data. After a brief introduction to the ILC itself, the document describes the status of the R&D program for the SiW Ecal. After that, the study of Higgs production at the ILC is presented. The document closes with a summary of the main results.

Chapter 1

Selected Results of Particle Physics Experiments

Contents

Particle physics seeks to discover the fundamental laws of nature, namely to understand fundamental, i.e. non-composed, particles and the interactions between these particles. This chapter gives an outline of the theoretical framework and the main conclusions which can be drawn so far. These conclusions are verified in dedicated experiments out of which a selection of results will be presented.

1.1 Charges, Symmetries and the Standard Model of Particle Physics

Extending the concept of classical mechanics to quantum mechanics, the equation of motions in a given system can be derived from a Lagrangian density $\mathcal{L}$ which contains the kinetic and potential energies of all the objects in the system. The quantum state of the system is given by the number of particles in various energy states of the system. A set of field operators create and annihilate particles into or from a corresponding quantum state. The dynamical properties of the system are determined by the dynamical properties of these operators.

Quantum Electrodynamics

Quantum Electrodynamics or *QED* is the quantum field theory which describes electromagnetic interactions. The field of the electrically charged electron can be represented by the complex operator $\psi(x)$. The Lagrangian density of the free field is

given by:

$$\mathcal{L} = i\bar{\psi}(x)\gamma^{\mu}\partial_{\mu}\psi(x) - m\bar{\psi}(x)\psi(x) \tag{1.1}$$

where the γ^{μ} are the Dirac matrices appearing since the electron is a spin $1/2$ particle (fermion) and can be thought of as a relativistic generalisation of the Pauli spin matrices.

The request for the symmetry under a global transformation of the phase of the wave, i.e. $\psi(x) \rightarrow \psi(x)e^{i\alpha}$ results in the conservation of the electric charge. Imposing a *local* phase invariance,

$$\psi(x) \rightarrow \psi(x)e^{i\alpha(x)} \tag{1.2}$$

introduces a covariant derivative

$$D_{\mu} = \partial_{\mu} - ieA_{\mu} \tag{1.3}$$

which gives raise to the gauge field A_{μ}. The gauge field A_{μ} transforms as

$$A_{\mu} = eA_{\mu} + \frac{1}{e}\partial_{\mu}\alpha(x) \tag{1.4}$$

which leads to the new Lagrangian

$$\mathcal{L} = i\bar{\psi}(x)\gamma^{\mu}D_{\mu}\psi(x) - m\bar{\psi}(x)\psi(x) = \bar{\psi}(x)(i\gamma^{\mu}\partial_{\mu} - m)\psi(x) + e\bar{\psi}(x)\gamma^{\mu}A_{\mu}\psi(x). \tag{1.5}$$

Only the last Lagrangian is invariant under the gauge transformation defined in 1.2. The request for local gauge invariance has lead to the introduction of a vector field A_{μ} which can be associated with the photon. The transformation described before is classified as a unitary transformation in one dimension. These kind of transformations which belong to the unitary symmetry group $U(1)$ are generated by a single parameter and are thus abelian. The abelian nature of the symmetry group manifest itself in the observation that the photons do not interact with each other.

The Lagrangian 1.5 contains a term which describes the interaction between a fermion with spin $1/2$ and a vector boson with spin 1. The interaction term in the Lagrangian density reads

$$e\bar{\psi}\gamma^{\mu}A_{\mu}\psi. \tag{1.6}$$

The coupling between the electrons or their anti-partners, the positrons, and the photons is proportional to the elementary electric charge e and the *dimensionless* coupling constant of QED α reads $e^2/4\pi$ in natural units and adopting the rationalised Heavyside-Lorentz system of electromagnetic units, which sets the dielectric constant ε_0 to unity [1]. Adding finally the kinetic term for the photon field, the Lagrangian for QED is obtained:

$$\mathcal{L} = \bar{\psi}(x)(\gamma^{\mu}\partial_{\mu} - m)\psi(x) + e\bar{\psi}(x)\gamma^{\mu}A_{\mu}\psi(x) - \frac{1}{4}F^{\mu\nu}F_{\mu\nu}. \tag{1.7}$$

The electrons (and positrons) have heavier partners, the μ and τ leptons, to which the theory of Quantum Electrodynamics can be applied in exactly the same manner. The ideas developed above for quantum electrodynamics can now be generalised in order to describe other forces present in nature.

Electroweak Interactions

The comparatively long lifetime of e.g. the muon gave rise to the postulation of *weak interactions*. The muon decay $\mu^- \rightarrow e^- + \bar{\nu}_e + \nu_\mu$, where $\bar{\nu}_e$ and ν_μ are neutrally charged neutrinos, is a *charged current* process. At low energies these reactions happen at a rate proportional to the Fermi coupling constant G_F. This coupling constant is one of the most precisely determined quantity in particle physics. Its value is listed to be $G_F = 1.16637(1) \times 10^{-5}\,\mathrm{GeV}^{-2}$ [2]. It is important to point out that this coupling constant has a dimension of an inverse mass squared. It can thus not be entirely the counterpart of the electromagnetic coupling constant introduced above. Today, it is well known, that the weak interaction is transmitted by heavy particles (in contrast to the photon), a fact which will be elaborated further below.

The weak interactions exhibit a maximal violation with respect to *P*arity and *C*harge transformations. In case of charged currents, the gauge bosons of the weak interaction couple only to left-handed fermions which may motivate the formulation of a quantum field theory which includes only left-handed particles. The two particles e and ν, and likewise for the μ and τ sector, can be considered as two different states of the same particle. They form a doublet $\chi_L = (\nu, e)_L$ with respect to the *isospin* T. Both particles are considered to have a total isospin of $T = 1/2$ differing in the third component T_3 of that isospin. A charged current reaction can hence be written in the following form

$$\left.\begin{array}{l} g[\bar{u}_\nu \gamma^\mu \frac{1}{2}(c_V - c_A\gamma^5)u_e](W^+)^\mu \\ g[\bar{u}_e \gamma^\mu \frac{1}{2}(c_V - c_A\gamma^5)u_\nu](W^-)^\mu \end{array}\right\} = g\bar{\chi}\gamma_\mu \tau^\mp \chi (W^\pm)^\mu \quad \text{with} \quad c_V = c_A = 1. \tag{1.8}$$

The entire current is of $V - A$ form as it combines a vector current V with an axial vector current A. The latter introduces the parity violation of the interaction by means of the projection operator $(1 - \gamma^5)$. In Equation 1.8, $W^\pm_\mu$ represent the charged bosons which are exchanged in a charged current reaction and to which the iso-doublet couples with strength g. The transition between the two isospin states introduces the ladder operators $\tau^\mp = \frac{1}{2}(\tau_1 \mp \tau_2)$ where $\frac{1}{2}\tau_{1,2}$ are the first two Pauli spin matrices. Together with the third Pauli matrix $\frac{1}{2}\tau_3$, the spin matrices form a set of linear independent 2×2 matrices from which every element of the group $SU(2)$ can be built. The irreducible representations of the group $SU(2)$ can be used to describe rotations in n-dimensions with n larger than one. Two $SU(2)$ transformation operations do not commute with each other which has the observable consequence that the bosons which can be assigned to this symmetry group interact among themselves.

Reactions of the type $\bar{\nu}_\mu e^- \rightarrow \bar{\nu}_\mu e^-$ [3] can be described by the existence of a neutral current which is however different from the one described by QED. It would be now tempting to describe this neutral current in the form

$$g\bar{\chi}\gamma_\mu \tau^3 \chi (W^3)^\mu \tag{1.9}$$

thus extending the pair of charged bosons by a neutral boson completing an isospin triplet with a total isospin of $T = 1$. The three bosons would then differ in the third

component T_3 of the isospin. The entire theory comprising the left handed fermions and bosons would then required to be invariant under $\mathrm{SU}(2)_L$ transformations. The neutral current, however, couples to left and to right handed fermions, i.e. $c_V, c_A \neq 1$ in 1.8, and can thus not be incorporated immediately into such a quantum field theory. The electromagnetic interaction on the other hand allows for the coupling to left and right handed particles. The weak and the electromagnetic interaction can be combined into two orthogonal combinations out of which one allows for the completion of the triplet of weak currents while the other is a copy of the electromagnetic interaction to the *hyper-charge* Y giving rise to the gauge boson B_μ and the corresponding coupling strength g'. Formally, this means that the two symmetry groups $SU(2)_L$ and $U(1)_Y$ are joined to the common symmetry group $SU(2)_L \times U(1)_Y$ and the theory is required to be invariant under these combined transformations. It is thus only the unification of the weak interaction and the electromagnetic interaction to the *electroweak interaction* which leads to a consistent theoretical treatment of the observed charged and neutral currents [4, 5, 6]. The quantum numbers Y and T_3 are related to the electric charge Q of a particle via:

$$Q = T_3 + Y/2. \tag{1.10}$$

The $SU(2)_L \times U(1)_Y$ eigenstates and the observed mass eigenstates of the neutral bosons, i.e. the Z boson and the photon, are related by the *weak mixing angle* $\sin\theta_W$. This relation reads:

$$\begin{aligned} A_\mu &= B_\mu \cos\theta_W + W^3_\mu \sin\theta_W \quad \text{and} \\ Z_\mu &= -B_\mu \sin\theta_W + W^3_\mu \cos\theta_W . \end{aligned} \tag{1.11}$$

It should be noted that after the orthogonal combination, the features of QED are entirely retained and the introduced couplings are related to the elementary electric charge e via

$$e = g \sin\theta_W = g' \cos\theta_W \tag{1.12}$$

The gauge boson sector of the electroweak theory consists of four bosons, three heavy bosons $\mathrm{W}^\pm$, Z and one mass-less uncharged boson, the photon, introduced above for the electromagnetic interaction. The origin of the mass of the vector bosons which are a priori not predicted by the theory will be outlined in Chapter 2.

Strong Interactions

Particles subject to the *strong interaction* carry a colour charge, which can appear in three different values, typically labelled *red, green and blue*. The quantum field theory of the strong force *Quantum Chromodynamics* or *QCD* describes the interactions between coloured spin 1/2 particles, called *quarks*, mediated by gluons. The underlying symmetry group is the non-abelian group $SU(3)$. Therefore, the *gluons*, themselves do carry a colour charge and interact among each other. Interactions between the coloured particles happen proportional to the strong coupling constant α_s. This coupling constant increases with decreasing energy corresponding to an

increase in distance between the colour charges. It is plausible that this increase of the strong force is the source for the (colour) confinement of quarks and gluons inside hadrons, also called infrared slavery. As a consequence it is impossible to observe free quarks in an experiment but only a jet of colourless hadrons emerging from it.

The Standard Model

The synthesis of the considerations above is described by the *Standard Model of Particle Physics* which can be summarised as follows:

- All matter is composed of 12 fundamental fermions, six leptons and six quarks and the corresponding anti-particles. According to the introduced $SU(2)_L \times U(1)_Y$ symmetry in terms of isospin and hyper-charge, the different lepton types and quark flavors are grouped into three left-handed isospin doublets and right handed isospin singlets. The Table 1.1 lists the doublets and singlets together with their isopin quantum numbers and their electrical charge. The existence of three quark families allows for the violation of the invariance against combined transformations of *C*harge and *P*arity. CP violation contributes to the asymmetry between matter and anti-matter in the universe. It has been experimentally observed in Kaon and B-Meson systems. A detailed introduction to the physics of CP violation can be found in the literature [7].

  Quarks are often distinguished between *up-type* quarks listed in the upper part of the quark doublets and the corresponding *down-type* quarks.

- The Standard Model describes two forces via which these particles interact among each other. One force is the electroweak force which decouples into the electromagnetic and the weak force towards small energies. The weak force is mediated by the massive vector bosons $W^{\pm}$, Z and acts on all fermions listed in Table 1.1. The electromagnetic force, mediated by the massless photon, acts only on particles with the electrical charge Q. The strong force, mediated by massless gluons, acts on particles carrying a colour charge like the quarks in Table 1.1.

- The masses of the particles can be explained by the existence of a scalar field, the Higgs field. Its field quantum, the Higgs boson, is a key ingredient to the Standard Model which has not been observed so far. The Chapter 4 will introduce in detail the measurement of the Higgs boson at the future International Linear Collider (ILC).

Perturbative Calculations

Apart from phase space and normalisation factors, the cross section for a given process to happen is proportional to the square of the transition matrix element

Family			T	T_3	Q
$\begin{pmatrix} \nu_e \\ e \end{pmatrix}_L$	$\begin{pmatrix} \nu_\mu \\ \mu \end{pmatrix}_L$	$\begin{pmatrix} \nu_\tau \\ \tau \end{pmatrix}_L$	$1/2$	$+1/2$	0
				$-1/2$	-1
ν_{eR}	$\nu_{\mu R}$	$\nu_{\tau R}$	0	0	0
e_R	μ_R	τ_R	0	0	-1
$\begin{pmatrix} u \\ d \end{pmatrix}_L$	$\begin{pmatrix} c \\ s \end{pmatrix}_L$	$\begin{pmatrix} t \\ b \end{pmatrix}_L$	$1/2$	$+1/2$	$+2/3$
				$-1/2$	$-1/3$
u_R	c_R	t_R	0	0	$+2/3$
d_R	s_R	b_R	0	0	$-1/3$

Table 1.1: *Fundamental fermions in the Standard Model. "L" and "R" stand for left-handed and right-handed fermions, T and T_3 are the total weak-isospin and its third component, and Q is the electric charge. The fermions are subdivided into leptons listed in the upper part of the table and quarks listed in the lower part of the table. Note that the results presented in this document are insensitive to, and independent of, any small ($< 20\,MeV$) neutrino masses.*

$|\langle i|S|f\rangle|^2$. Here, i and f indicate the initial and the final state of the process and S is the interaction Hamiltonian carrying the annihilation and creation operators of the initial and final state particles. In principle, the expression before is an element of the so called S-Matrix which contains all possible transition probabilities. The precise form of the transition matrix elements depends thus on the number of particles in the initial and final state and the number of interactions which are to be taken into account. As a given interaction is characterised by the coupling constant, e.g. α for QED, the expansion of the S-Matrix results in a power series of this coupling constant depending on the amount of contributions, or corrections, to a given process taken into account.

In particle physics every process, or element of the S-Matrix, can be depicted by *Feynman Diagrams* containing the initial and final state particles as well as the intermediate virtual particles. The Figure 1.1 shows the Feynman Diagrams for lowest order or *tree level* fermion pair production in e^+e^- annihilation. The e^+e^--pair annihilates into one of the electrically neutral vector bosons, the Z or the photon. Subsequently these bosons decay into the final state fermion pair. The annihilation process is also called the s-channel in contrast to the t or u-channels in which the intermediate particles are exchanged between the initial state particles.

The Figure 1.2 shows diagrams for higher order correction given e.g. by the loop in the internal photon line. These diagrams contain more than two interaction vertices. At higher orders, either additional particles are created or contributions

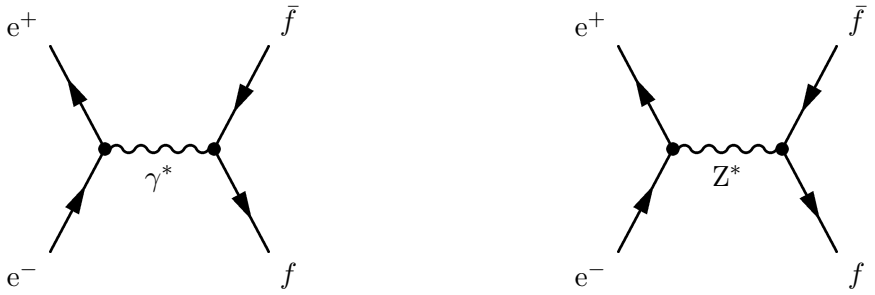

Figure 1.1: *The lowest-order s-channel Feynman diagrams for* $e^+e^- \to f\bar{f}$*. For* e^+e^- *final states, the photon and the Z boson can also be exchanged via the t-channel or u-channel.*

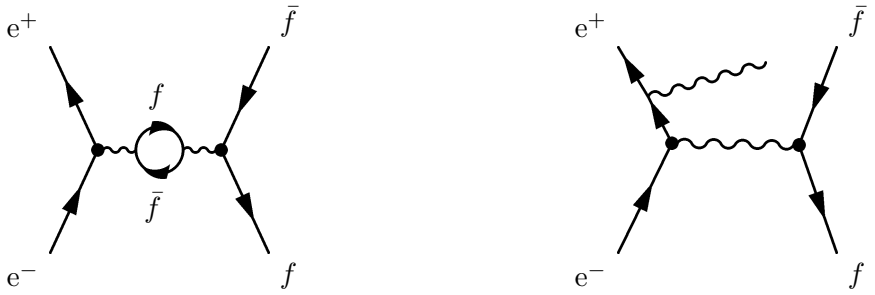

Figure 1.2: *Examples for higher order QED corrections to fermion-pair production. The left hand side shows the vacuum polarisation diagram and the right hand side the radiation of an additional photon.*

from intermediate, virtual particles have to be taken into account. These *higher order* corrections have two consequences:

- The virtual corrections lead to a redefinition or *renormalisation* of the coupling constants which in turn are proportional to the square of the relevant charge for the interaction. In QED, the vacuum polarisation illustrates the fact that within a quantum field theory, owing to the Heisenberg Uncertainty Principle [8], an electron for example can be considered as being surrounded by a cloud of e.g. electron-positron pairs [9]. These screen the "true" charge of the electron at a given distance from the charge. Due to the abelian nature of QED, the photons do not carry a electrical charge and thus do not contribute to the screening. With higher energies one can probe closer distances to the charge and the observed charge appears less screened. Therefore, the coupling constant α of QED becomes dependent on the energy at which a process in happening and increases with increasing energy. The coupling constant α_s of the strong interaction decreases with incresing energy since the colour charge of the gluons leads to an anti-screening, i.e. the colour charge appears larger at large distances than at small distances. The resulting increase of α_s towards small energies gives an intuitive explanation for the fact that quarks do not exist as free particles but are confined within hadrons.

- The virtual corrections may comprise additional, heavy particles which are

not producible as real physical states in the actual process but which are part of the theory. Considering correctly higher order corrections may thus deliver important hints for the existence of new particles.

1.2 Electroweak Measurements in the Pre-LEP/SLC era

The interference between the neutral electromagnetic current and the neutral weak current leads to predictions on the production rate of e.g. lepton pairs in different hemispheres of the detectors. Electromagnetic interactions preserve the parity, thus leading to equal production rates in opposite detector hemispheres. On the contrary, the coupling to the Z boson leads to a forward-backward asymmetry of the final state leptons. The predicted behaviour of the asymmetry has indeed been observed in a number of e^+e^- collision experiments at centre-of-mass energies of up to $\sqrt{s} \approx 60\,\mathrm{GeV}$, for a compilation of results see [10]. As an example, the Figure 1.3 shows a measurement at $\sqrt{s} = 35\,\mathrm{GeV}$ obtained at the PETRA storage ring at DESY for μ and τ lepton pair production [11]. The observation is compared with a prediction assuming photon exchange only. The asymmetry increases with centre-of-mass energies corresponding to an increased influence of the Z boson to the production cross section. The onset and magnitude of the asymmetry allows to predict the mass of the Z boson to be of the order of 90 GeV.

The SpS at CERN, which collided protons and anti-protons at a centre-of-mass energy of 540 GeV, was conceived to produce the massive bosons W and Z directly in experiment. The two experiments UA1 and UA2 were able to record signals of these bosons by means of their decays into two leptons and the reconstruction of the invariant mass of that di-lepton pair or by reconstruction of the transverse mass of this di-lepton pair. The values as published by the two collaborations for the reconstructed mass of the W and Z, M_W and M_Z are [12, 13, 14, 15]:

$$m_\mathrm{W} = 81^{+5}_{-3}\,\mathrm{GeV}\ \ (\mathrm{UA1}) \quad \text{and} \quad m_\mathrm{W} = 80^{+10}_{-6}\ \ (\mathrm{UA2}) \tag{1.13}$$

and

$$m_\mathrm{Z} = 95.2 \pm 2.5\,\mathrm{GeV}\ \ (\mathrm{UA1}) \quad \text{and} \quad m_\mathrm{Z} = 91.9 \pm 1.3 \pm 1.4\ \ (\mathrm{UA2}) \tag{1.14}$$

The direct measurements allow to test essential predictions of the electroweak theory. Firstly, the known W mass is related to the weak mixing angle via

$$G_F = \frac{e^2\sqrt{2}}{8 m_\mathrm{W}^2 \sin^2\theta_W}. \tag{1.15}$$

The values of the W boson mass obtained in these discoveries are in agreement with the expectation of the electroweak theory which predicts a value of $\sin\theta_W \approx 0.25$. Details on precision measurements of this observable will be reported in the next section. In addition, the measurements confirmed another elementary

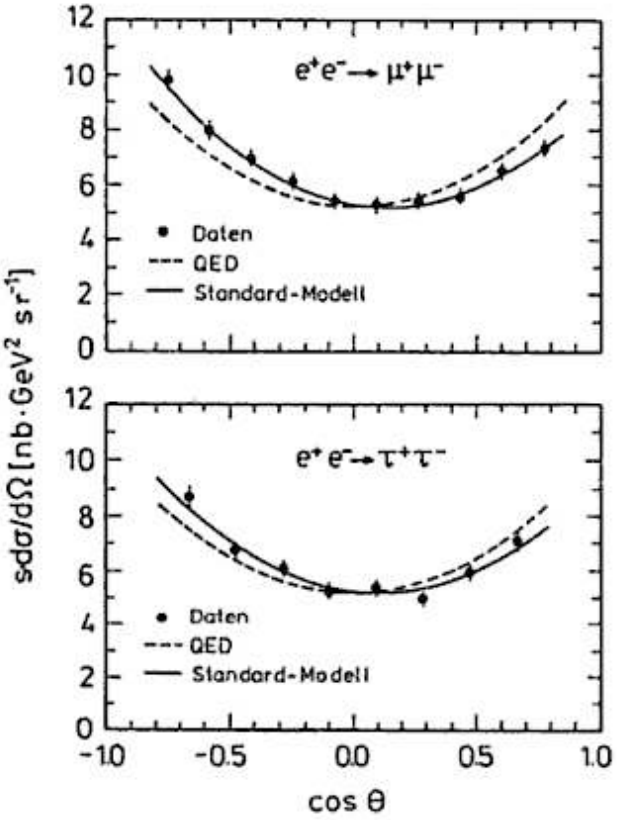

Figure 1.3: *Differential cross section of lepton pair production observed with the JADE Detector at PETRA. The measurement show a clear production asymmetry between large and small values of the polar angle θ, measured w.r.t. the direction of the incoming electron.*

prediction of the electroweak theory, namely a well defined relation between the mass of the W and that of the Z boson:

$$\frac{m_{\mathrm{W}}}{m_{\mathrm{Z}}} = \cos\theta_W. \tag{1.16}$$

This equality holds exactly for electroweak interactions at tree level.

The fundamental measurements presented before motivated experiments at a centre-of-mass energy compatible with the Z boson mass, $90 \lesssim m_{\mathrm{Z}} \lesssim 100\,\mathrm{GeV}$. Around this energies a huge rate of Z is expected which naturally enabled the high precision tests of the electroweak theory. These experiments at the accelerators LEP and SLC were realised in the late 1980s and their results will be discussed in the following section.

1.3 Electroweak Precision Measurements at LEP and SLC

The discovery of the heavy bosons clearly established the electroweak theory as a viable approach to describe the 'non strong' interactions and was followed by a phase of precision tests of this theory. Notably by the accelerators LEP and SLC high precision tests were made possible. These machines allowed for collisions of electron and positrons at centre-of-mass energies between the mass of the Z boson passing the W pair production threshold up to more than 200 GeV, a domain where it could have been expected to discover the Higgs boson (see below). In the following, the two colliders are briefly introduced.

- LEP [16], short for Large Electron Positron Ring, was operated at CERN between 1989 and 2000. It was a storage ring of 26.7 km circumference in which high energetic electrons and positrons were brought at four points into collisions. At these four collision points the experiments ALEPH, DELPHI, L3 and OPAL were operated. The results from LEP which will be cited are obtained by combinations of the individual results of these four experiments. Note, that the LEP operation is divided into a LEPI part, for measurements at an energy corresponding to the Z mass and a LEPII part for measurements at the WW pair threshold and beyond. The maximum centre-of-mass energy reached at LEP was 209 GeV.

- SLC [17], short for Stanford Linear Collider, consisted of a linear accelerator and a system of arcs. The electrons and positrons were accelerated to up to 50 GeV in the 3 km long linear part. Subsequently they were injected into two arcs in opposite directions and brought into collision in the centre of the SLD detector. A remarkable feature of the SLC accelerator is that it could produce collisions with longitudinally polarised electrons.

The Figure 1.4 [19] gives a list of important Standard Model observables based on results mainly from LEP and SLC which will partially be outlined in this section and in Section 1.5. For a detailed discussion on these and the other observables see [18] and corresponding updates [19]. The figure includes in its right part the difference between the measured value and its expectation from a global fit of these observables based on the Standard Model. At LEP and SLC, the Z boson is produced resonantly leading thus to a strong increase of the production cross section at the centre-of-mass energy at the actual value of the mass. Figure 1.5 shows the e^+e^- cross section as a function of the centre-of-mass energy. The strong maximum at around 90 GeV is clearly visible. By performing a scan of the centre-of-mass energy around the maximum of the cross section, the mass of the Z boson can finally be determined. Subsequent running at the energy corresponding to the Z boson mass lead to a measurement of the Z mass with extremely small errors. The current world average based on LEP data yields the value

$$m_{\mathrm{Z}} = 91.1874 \pm 0.0021\,\mathrm{GeV}. \tag{1.17}$$

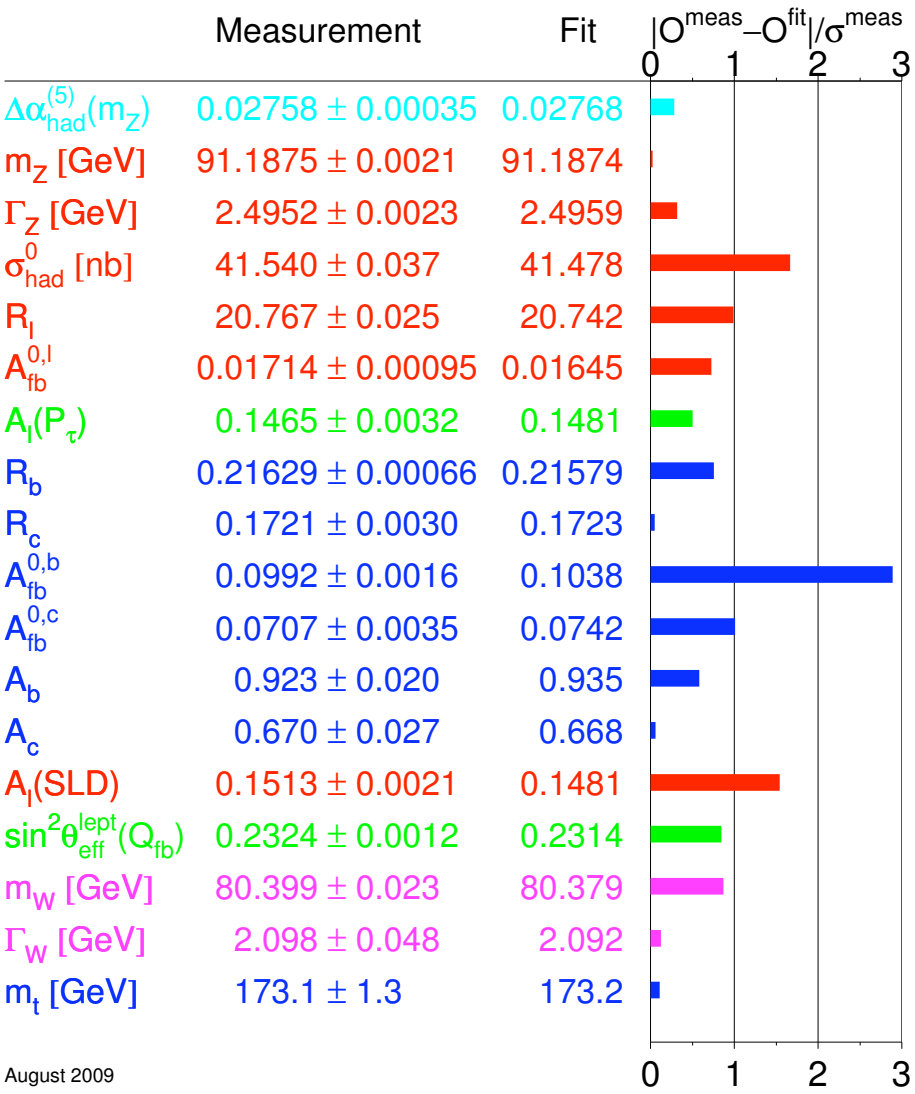

Figure 1.4: *Comparison of the measurements with the expectation of the Standard Model based on a global χ^2 fit. Also shown is the pull of each measurement, where pull is defined as the difference of measurement and expectation in units of the measurement uncertainty. The given values reflect the status as of August 2009.*

The total decay width of the Z boson is measured to be $\Gamma_Z = 2.4952 \pm 0.0023$. Within the Standard Model, the Z decays exclusively into fermions. The partial widths of the decays into quarks and electrically charged leptons have been determined with large accuracy. From these partial widths and the total decay width, the decay width for invisible Z decays can be inferred. The results of LEP allows for the important conclusion that there are not more than three left-handed, light neutrinos. More precisely, the derived number of left-handed, light neutrinos neutrinos is $N_\nu = 2.9840 \pm 0.0082$.

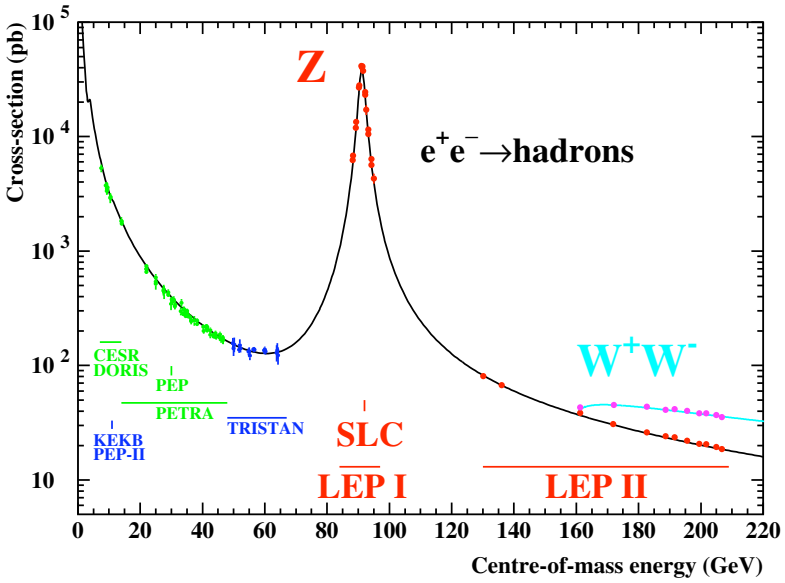

Figure 1.5: *The hadronic cross-section as a function of centre-of-mass energy. The solid line is the prediction of the Standard Model, and the points are the experimental measurements. Also indicated are the energy ranges of various* e^+e^- *accelerators. The cross-sections have been corrected for the effects of photon radiation [18].*

As already indicated above, the asymmetric production of fermions in opposite hemispheres of the detector is a crucial prediction of the electroweak theory. The forward-backward asymmetry is defined as:

$$A_{FB} = \frac{N^F - N^B}{N^F + N^B} \tag{1.18}$$

Here $N^{F/B}$ indicate the number of charged fermions found in the forward (F) or backward (B) detector hemisphere with respect to the direction of the incoming electron. In case of a polarised electron beam, asymmetries of measured cross sections can be defined. In these cases the asymmetries reads

$$A_{LR} = \frac{N^L - N^R}{N^L + N^B} \frac{1}{\langle |\mathcal{P}_e| \rangle} \tag{1.19}$$

for the left-right asymmetry. The superscripts L and R indicate the number of charged fermions measured for different values of the electron beam polarisation $\mathcal{P}_e$. It is intuitively clear that both asymmetries are sensitive to the parity violating effects predicted by the electroweak theory and to the weak mixing angle for the coupling to leptons $\sin^2\theta^{\text{lept.}}_{\text{eff.}}$. The subscript "eff." indicates that in contrast to e.g. Equation 1.16 it is defined at one loop level. As can be inferred from Figure 1.4, the asymmetry A_{FB} agrees with the Standard Model prediction for light quarks as e.g. the c quark. On the other hand, the LEP experiments report an asymmetry for b quarks which is significantly smaller than predicted by the Standard Model. The asymmetry for b quarks leads, however, to the most precise value reported by LEP on $\sin^2\theta^{\text{lept.}}_{\text{eff.}}$ with

$$\sin^2\theta^{\text{lept.}}_{\text{eff.}} = 0.23221 \pm 0.00029. \tag{1.20}$$

The measurement of the left-right asymmetry A_{LR} with polarised beams is an alternative way to determine $\sin^2\theta^{\text{lept.}}_{\text{eff.}}$. The analysis published by SLD takes all final state into account but electrons, in order to count only resonant Z decays. The current world average for the leptonic left-right asymmetry is:

$$A_{LR} = A_l = 0.1513 \pm 0.0021 \tag{1.21}$$

from which $\sin^2\theta^{\text{lept.}}_{\text{eff.}}$ can be deduced to be:

$$\sin^2\theta^{\text{lept.}}_{\text{eff.}} = 0.23098 \pm 0.00026 \tag{1.22}$$

It is striking, that the most precise value reported by LEP on $\sin^2\theta^{\text{lept.}}_{\text{eff.}}$ extracted from A_{FB} for b quarks disagrees by about four standard deviations with the value found by SLD which is the most precise individual determination of $\sin^2\theta^{\text{lept.}}_{\text{eff.}}$. The clarification of the $A_{FB,LR}$ puzzle and hence on the disagreement in $\sin^2\theta^{\text{lept.}}_{\text{eff.}}$ will be one of the most important measurements at a future linear collider where the asymmetry can be determined using the top quark and where again polarised beams can be employed.

The mass of the W boson has been determined at LEP as well. At LEP data were recorded at or above the WW pair production threshold, i.e. in events of the type $\mathrm{e^+e^-} \to \mathrm{W^+W^-}$. At these energies the WW pairs are produced double resonantly leading to a production cross section which is about 8 times higher than that of single W boson production which would be energetically favoured. The W bosons are reconstructed by means of their leptonic and hadronic decays. The well known initial state is exploited to account for wrong jet pairing and or missing momentum due to the neutrinos escaping the detection. The average of the LEP measurements is [20]:

$$m_{\mathrm{W}} = 80.376 \pm 0.033\,\mathrm{GeV}. \tag{1.23}$$

Its decay width has been determined to:

$$\Gamma_{\mathrm{W}} = 2.196 \pm 0.083\,\mathrm{GeV}. \tag{1.24}$$

1.4 Studies of Electroweak Physics and Quantum Chromodynamics at HERA

HERA is a storage ring which was operated between 1992 and 2007 and in which electrons of 27.6 GeV were collided with protons of 920 GeV at two interaction points equipped with the experiments H1 and ZEUS.

The proton is known to be composed of quarks and gluons, also called partons, which carry a momentum fraction x of the total momentum of the proton. The electric charge of the proton is given by the combined charges of its three *valence quarks*, two u quarks and one d quark. The electron scatters off the partons of the proton via the exchange of one of the vector bosons with a virtuality of Q^2. At a high energy transfer y to the proton, it is broken up which motivates the term *Deep Inelastic Scattering* or *DIS*. The final state of the scattering process consists of the scattered electron or neutrino and one or several quarks leading to jets observed in a detector. A sketch of the deep inelastic scattering process is shown in Figure 1.6.

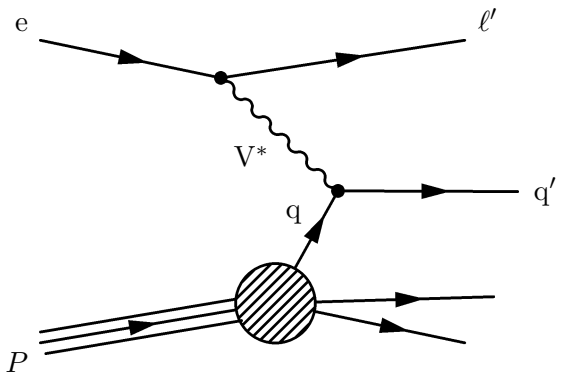

Figure 1.6: *Sketch of deep inelastic electron proton scattering. The incoming electron* e *scatters off a parton* q *of the proton* P *under the exchange of a virtual boson* V* (V = Z, W, γ). *The final state consists of an electron* ℓ' (ℓ = e, ν), *the scattered quark* q′ *and the proton remnant.*

The virtuality of the exchanged vector boson covers a wide range in Q^2. The range starts a $Q^2 \approx 0$ when a nearly real photon is exchanged and extends up to $Q^2 \approx 10^4\,\text{GeV}$ where the reaction happens mostly via the exchange of a heavy vector boson. This considerable momentum range permits the testing of theoretical predictions in a large region of phase space. Particularly, it allows for the verification of two key hypothesis of the electroweak theory:

- The electromagnetic force and the weak have equal strength at energies comparable with the masses of the massive vector bosons.
- The cross section for charged weak bosons coupling to the 'wrong' helicity is exactly zero.

Figure 1.7 [25] shows the charged and neutral cross section as measured in deep inelastic scattering reactions at HERA. At low Q^2, the cross section is dominated by pure photon exchange. In this kinematic region, the exchange of the heavy bosons $W^{\pm}$ and Z is strongly suppressed which explains the small values of the charged current cross section there. At $Q^2 \approx 10^4\,\mathrm{GeV}$, where the photon and Z exchange contributions to the neutral current cross sections are of similar size to those of $W^{\pm}$ exchange, the two cross sections join each other and remain equal in magnitude towards larger values of Q^2. This observation is the experimental manifestation of the unification of the electromagnetic and weak coupling strengths in deep inelastic scattering processes. Note also, that the experiment has been conducted with electrons and positrons in the initial state. The differences between the actual values of the cross section can be explained by the helicity dependency of the electroweak interactions in case of the neutral current cross section and by the quark content of the proton (uud) which enhances the interaction probability for electrons in case of the charged current cross section.

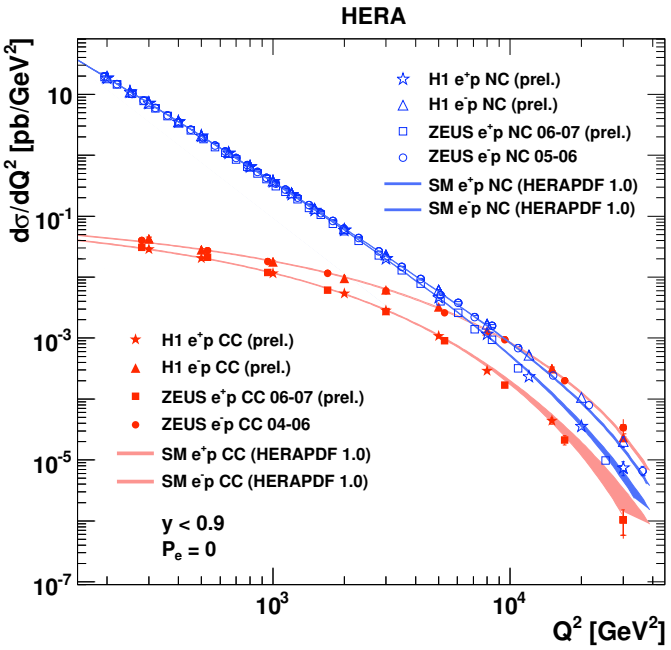

Figure 1.7: *The Q^2 dependences of the NC (circles) and CC (squares) cross sections $\mathrm{d}\sigma/\mathrm{d}Q^2$, shown for several years of data taking. The results are compared with the corresponding Standard Model expectations based on the HERAPDF1.0 parameterisation of the proton structure.*

Spin Rotators embedded into the HERA accelerator allow for the setup of different spin states of the electron beam. Thus, beams with right or left-handed polarisation of the electrons or positrons can be brought into collision with the pro-

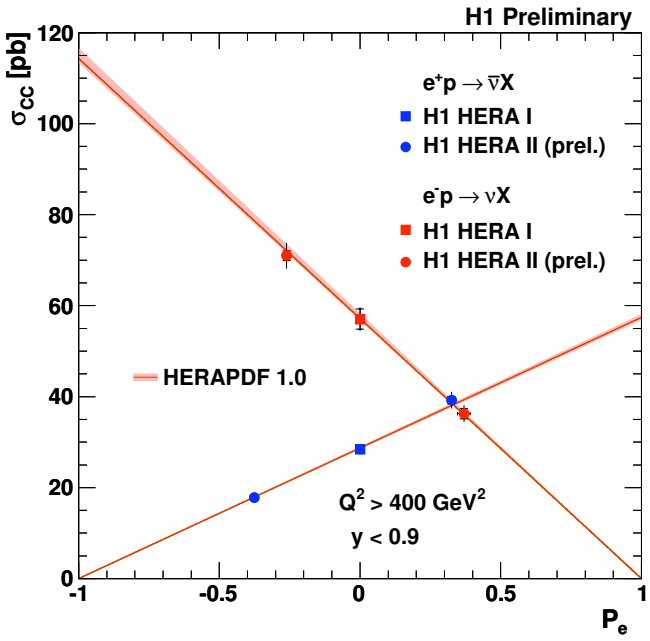

Figure 1.8: *The dependence of the e^+p CC cross section on the lepton beam polarisation P_e. The inner and outer error bars represent the statistical and total errors, respectively. The data are compared with Standard Model predictions based on the HERAPDF1.0 parameterisation of the proton structure.*

ton beam. The precision of the determination of the polarisation of the electron beam with Compton Polarimeters is quoted to be 5% [22]. Precisions of better than 1% were reached with a Fabry-Perot Polarimeter built by the H1 group of LAL Orsay [23, 24]. The W bosons couple only to left-handed electrons or right-handed positrons. Therefore, the charged current cross section for a right-handed electron or a left-handed positron beam is expected to vanish. Figure 1.8 [25] shows the charged current cross section as a function of the beam polarisation. By comparison with a theoretical prediction, it can be concluded that the charged current cross section is compatible with zero for left-handed positrons (right handed electrons), i.e. a beam polarisation of -1, $(+1)$, and increases with the change of the beam polarisation towards $+1$, (-1) according to the parity violating nature of the weak interaction.

Parallel to the studies of the electroweak interactions, the electron proton collisions allow for the investigation of the strong interaction and its underlying theory, QCD. As indicated above, the quarks in the proton interact among themselves due to their colour charge. This interaction is mediated by gluons. These gluons in turn can fluctuate into quark-antiquark pairs. Therefore, the proton can be considered as a dynamic object with a rich particle content. The electron on the other hand can

be considered as a probe for the resolution of the sub-structure of the proton. The resolution power is given by the virtuality of the exchanged vector boson. Following the Heisenberg Uncertainty Relation, a large virtuality allows for resolving small spatial structures. Hence, with increasing Q^2 the probability of observing partons carrying a small fraction x of the proton momentum increases while that of observing partons carrying a large fraction decreases. These so called *scaling violations* are thus a manifestation of effects of the strong interactions among the partons within the proton. Formally, the described predictions are expressed in terms of the proton structure functions $\tilde{F}_i(x, Q^2)$. The *reduced* double differential cross section for neutral current deep-inelastic scattering has the well known form:

$$\sigma^{\pm}_{r,\mathrm{NC}} = \frac{\mathrm{d}^2\sigma^{e^{\pm}p}_{\mathrm{NC}}}{\mathrm{d}x\mathrm{d}Q^2} \cdot \frac{Q^4 x}{2\pi\alpha^2(y+1)} = \tilde{F}_2 \mp \frac{y-1}{y+1} x\tilde{F}_3 - \frac{y^2}{y+1}\tilde{F}_L \ . \tag{1.25}$$

In its reduced form, the cross section reflects directly the dependency of the measurement on the proton structure. The result of the most recent measurement of the reduced cross section in a large phase space region is given in Figure 1.9 [21]. It clearly shows the rise towards large values of Q^2 in particular for small values of the fractional momentum x. The precise measurements are excellently described by a fit, here called HERAPDF1.0 fit, which incorporates the QCD predictions for the measurements which strongly supports QCD to be the correct theory for strong interactions.

The gluons in the proton can only be produced by radiation off the coloured quarks. As the probability for a radiation of a high energetic gluon is very small, it is very unlikely to observe a gluon with a momentum fraction $x \approx 1$ in the proton. The probability for this observation is expressed in the gluon density x_g. Indeed, as shown in Figure 1.10, the gluon density rapidly approaches 0 when x approaches 1.

Due to the radiation of a gluon, a quark may gain a sizable transverse momentum. In a frame, e.g. the Breit Frame, in which the incoming virtual boson and the parton collide head on, this leads to the creation of two particles with high transverse momentum; one given by the radiated gluon and the other given by the quark recoiling against this gluon, see Figure 1.11

Thus, the investigation of final states with two jets with large transverse momentum allows for direct tests of Quantum Chromodynamics. The jet cross section is directly proportional to the strong coupling constant α_s and the electron proton collisions permit to cover a large range of scales in one single experiment. The Figure 1.12 [26] shows the latest result published by the H1 Collaboration. The energy scale over which α_s has been determined spans two orders of magnitude. The most precise value of $\alpha_s(m_Z)$ from jet measurements is obtained for the region $150 < Q^2 < 15000$ and is reported to be [27]:

$$\alpha_s(m_Z) = 0.1168 \pm 0.0007(\mathrm{exp.})^{+0.0046}_{-0.0030}(\mathrm{th.}) \pm 0.0016 \tag{1.26}$$

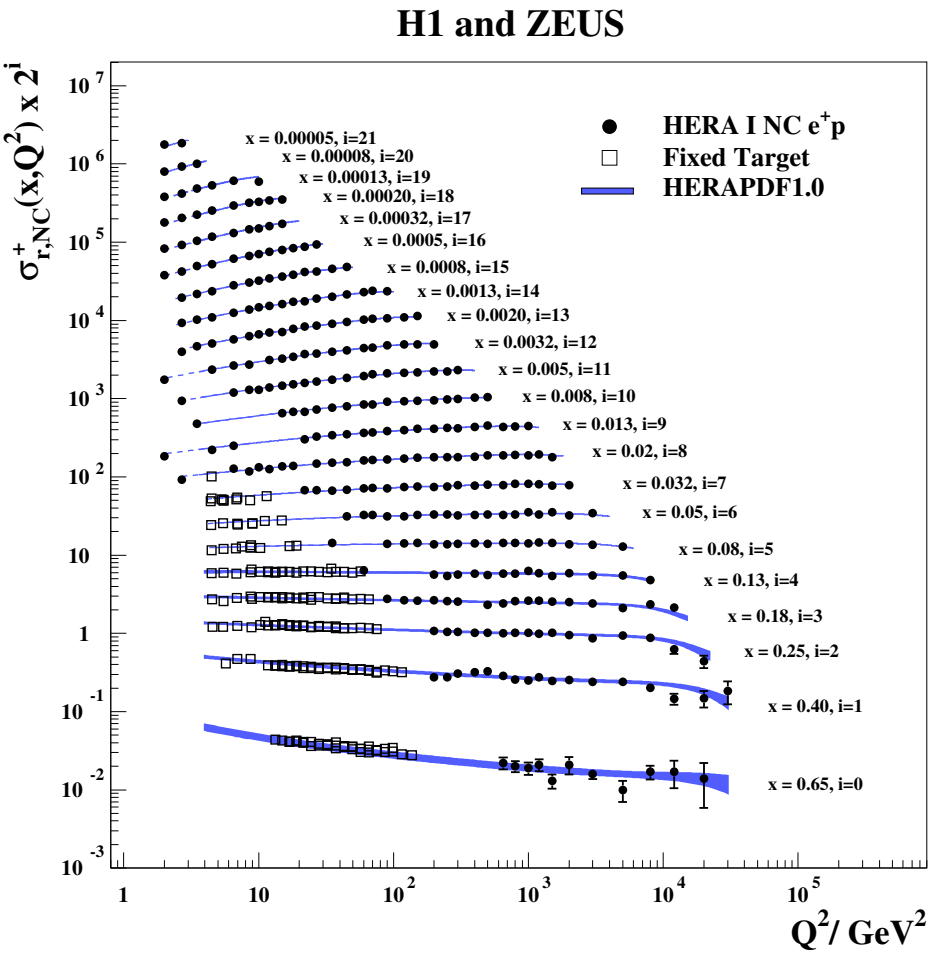

Figure 1.9: *HERA combined NC e^+p reduced cross section and fixed-target data as a function of Q^2. The HERAPDF1.0 fit is superimposed. The bands represent the total uncertainty of the fit. Dashed lines are shown for Q^2 values not included in the QCD analysis.*

which agrees very well with the world averages $\alpha_s(m_Z) = 0.1176 \pm 0.0020$ [2] and $\alpha_s(m_Z) = 0.1184 \pm 0.0007$ [28].

The shape of the curve confirms the QCD prediction that at large scales the partons in the proton are asymptotically free, while towards small scales the colour forces increase and lead to the confinement of quarks within hadrons.

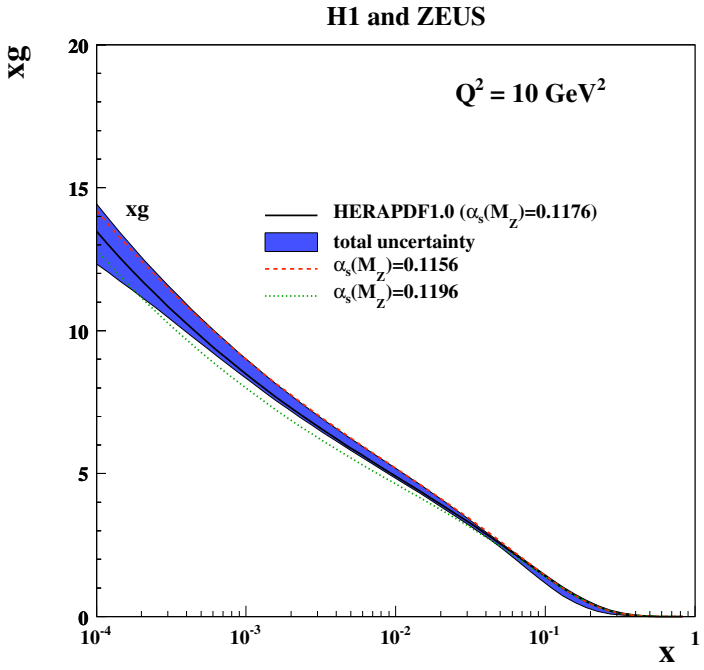

Figure 1.10: *The gluon density x_g from HERAPDF1.0 compared for different values of α_S. The band shows total uncertainties of the HERAPDF1.0 fit.*

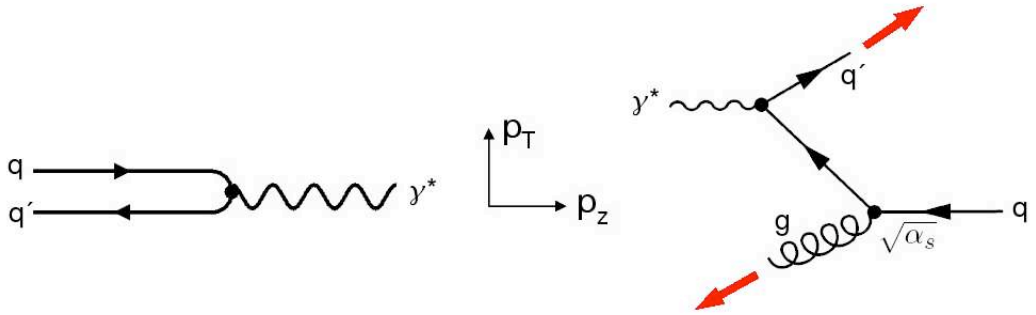

Figure 1.11: *DIS process in the Breit Frame. Left: Without QCD effects, the incoming quarks bounces back from the photon and gains no transverse momentum. Right: The radiation of a gluon off the quark leads to a quark and a gluon with sizable transverse momentum which manifest themselves as jets in the detector. Jet cross section are hence sensitive to the coupling constant of the strong force α_s.*

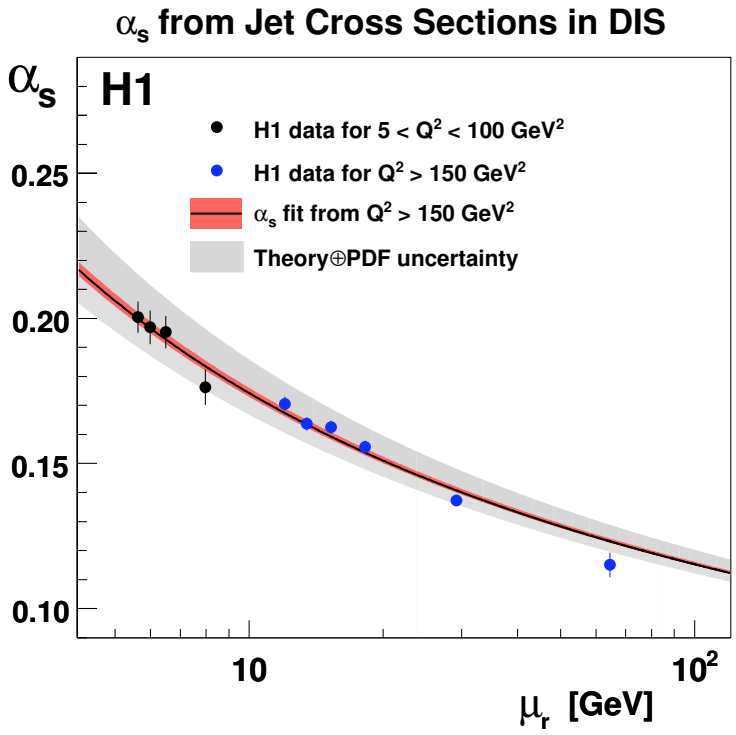

Figure 1.12: *The strong coupling constant α_s as a function of the energy scale μ_r as determined from jet cross sections in DIS.*

1.5 Top Quark and W Boson production at the Tevatron

The discovery of the *bottom* or b quark [29] and the consequent application of the GIM mechanism [30] which in case of the c quark was introduced to suppress non-observed flavor changing neutral currents, results in the prediction of the existence of the t or *top* quark. Another more subtle motivation is that higher order corrections with triangular fermion loops give rise to unrenormalisable divergences. It turns out that these divergences cancel if the following relation holds [31]:

$$\frac{1}{2}\sum N(Q_\nu^2 + Q_\ell^2 + N_c(Q_u^2 + Q_d^2)) = 0 \tag{1.27}$$

Here the Q_i represent the electric charge of the neutrinos, the charged leptons and the up-type and down-type quarks. N_C is the number of color charges. For three lepton families, the equation is fulfilled if there are six quark flavours grouped in three families. The masses of these quarks are strongly different. While the lightest quark, the u quark has a mass as small as 1.5...3.3 MeV [2], the heaviest among the quarks, the t quark has a mass of the order of a gold atom. With that mass it is roughly 40 times heavier than the next heaviest quark, the b quark. The top quark was discovered in 1995 at the $p\bar{p}$ collider Tevatron [32, 33]. The accelerator is operated at a centre-of-mass energy of up to 1.96 TeV. The protons and anti-

protons are brought into collision at two interaction points at which the experiments CDF and D0 are installed. In a few events the colliding proton and anti-proton constituents carry enough energy for the production of a $t\bar{t}$ pair. Due to its large mass, the t quark has a large phase space for decays and thus a short lifetime which is of the order of 10^{-26} s. The t quark decays predominantly into a W boson and a b quark. The mass of the top can be reconstructed by correctly detecting and reconstructing the decay products. The b quark hadronises to form a jet and the W can either be identified by its leptonic decay products or by two jets yielding the W mass. The Figure 1.13 shows the latest result of the value of the mass of the top as published by the D0 collaboration. The D0 collaboration reports a value of $m_{\mathrm{t}} = 173.7 \pm 1.8$ [34] which is in good agreement with the current world average [19] of:

$$m_t = 173.1 \pm 1.3\,\mathrm{GeV} \tag{1.28}$$

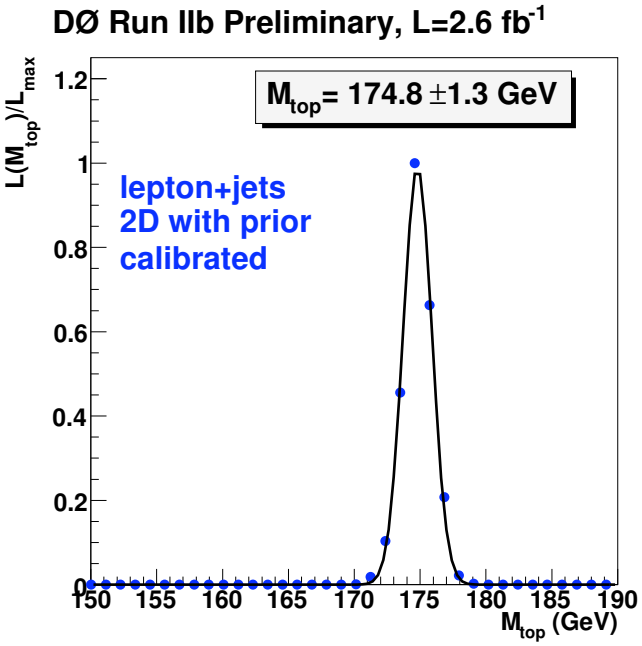

Figure 1.13: *Determination of the t quark mass by the D0 Collaboration.*

Naturally, the Tevatron is also a production facility for W bosons. As was the case for SpS, the most precise measurement are obtained in the leptonic channel, i.e. $\mathrm{W} \to \ell^{\pm} + \nu_{\ell}$. The neutrino escapes detection but by employing conservation of transverse momentum, the mass can be reconstructed from the reconstructed transverse momentum of the detected charged lepton. This method leads to a transverse mass with a Jacobian peak at $m_{\mathrm{W}}/2$. The Figure 1.14 shows a recent determination of the W mass [35]. The current average combining all recent Tevatron and LEP

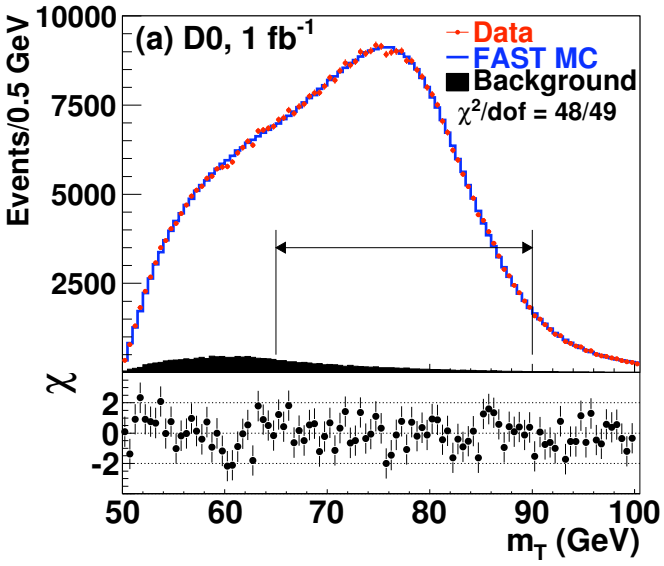

Figure 1.14: *Determination of the* W *mass by the D0 Collaboration.The figure shows in its upper part the comparison between data and the theoretical prediction. In the lower part the* χ^2 *values of this comparison are displayed. In addition the range used for the actual mass determination is indicated.*

results of the W mass and its decay width is given to be [19]:

$$m_{\mathrm{W}} = 80.399 \pm 0.023\,\mathrm{GeV} \tag{1.29}$$

$$\Gamma_{\mathrm{W}} = 2.098 \pm 0.048\,\mathrm{GeV} \tag{1.30}$$

In contrast to the experiments described in Sections 1.2 to 1.5 the Tevatron is still scheduled to take data until the end of 2011. Thus, the measurements from this accelerator will continue to improve the precision of the electroweak parameters, in particular those of the W boson mass and the top quark mass.

1.6 Open Questions and Future Experiments

The sections above outlined the theoretical framework of the Standard Model of particle physics and how it has been impressively confirmed by data throughout the last decades. The missing ingredient to complete the Standard Model is the Higgs boson which is considered to be at the origin of the mass of the particles. It is however also true that the Standard Model leaves a number of very important questions open and features several severe inconsistencies. A few of these open questions and inconsistencies are summarised in the following:

- Does the Higgs boson exist and if yes, is it the Higgs boson as expected from the Standard Model?

- As will become clearer in Chapter 2, the electroweak theory is a spontaneous broken symmetry. What is at the origin of this symmetry breaking?

- What is at the origin of the dramatic hierarchy in the masses of the fermions? The lightest neutrino has a mass of not more than 2 eV [2] while the heaviest quark as a mass of about 175 GeV. Thus, the range spans eleven orders of magnitude. As of today there is no explanation for this striking difference.

- Gravity is not included into the Standard Model as the relativistic treatment of the theories introduced so far requires an Euclidean metric of the space-time. That means that the metric tensor $g_{\mu\nu}$ has no off-diagonal elements. As gravity effects lead to a curved space-time, the current theories are only valid for cases in which gravitational effects can be neglected. This is justified due to the small value of the Newton Constant $G_N \approx 10^{-38}\,\mathrm{GeV}^{-2}$ at current accessible energy ranges with accelerators. It is however expected that gravity becomes strong at the Planck scale $\Lambda_P \approx 10^{19}\,\mathrm{GeV}$. The formulation of a theory which unifies all interactions including gravity is one of the big challenges in particle physics.

Beyond these questions inherently open within the framework of particle physics, there are questions opened by astrophysical observations, for example.

- The visible matter in the universe accounts only for roughly 4% of the total mass of the universe. About 25% of the other 96% is assigned to weakly interacting particles. The Standard Model contains no particle and has no mechanism which could explain the abundance of this *Dark Matter* in the universe.

The answer to these questions requires higher energies than could be achieved hitherto. In autumn 2008 the Large Hadron Collider (LHC) was turned on at CERN at Geneva. This accelerator provides proton-proton collisions at a centre-of-mass energy of up to 14 TeV. The main motivations for the construction of this machine are the discovery of the Higgs boson and the search for dark matter candidates.

The impressive establishment of the electroweak theory as being correct up to the so far accessible energies, is based on a tight interplay between hadron accelerators on one hand (SpS, Tevatron) and electron-positron colliders on the other hand (PETRA, TRISTAN, LEP, SLC). Whatever will be discovered at the LHC, the precision which can be obtained at this machine is limited by the complicated structure of the initial state hadrons and the huge background expected from QCD induced reactions at the LHC. Deep understanding of the physics beyond the Standard Model requires thus the parallel running of a precision machine.

In this context the case for a high energy electron positron collider is striking. Therefore, this document concentrates on studies towards the realisation of such a

collider. In particular, the precision which will be obtained in the experiments at this collider will be highlighted.

Chapter 2

Introduction to Higgs Boson Physics

Contents

This chapter is dedicated to the physics of the Higgs boson. The Higgs boson is the missing piece of the Standard Model of particle physics. Most presumably its existence will explain the masses of the particles contained in the Standard Model and more general will help to understand the origin of electroweak symmetry breaking. The theoretical introduction in this chapter will follow the presentations in [1, 36, 37]. After the introduction of the theoretical framework, the role of the Higgs boson in theories beyond the Standard Model will be discussed. Further, it will be explained how to observe the Higgs boson at lepton colliders and an outline on current theoretical and experimental limits on its mass will be given.

2.1 The Higgs Mechanism - The Origin of Mass?

To motivate the introduction of the Higgs boson, two facts should be repeated. First, the weak interactions require the existence of heavy gauge bosons which are in many ways similar to the photon, but they do have a non-zero mass. However, second, the incorporation of massive gauge bosons by hand into e.g. the Lagrangian of QED, Equation 1.7, breaks the gauge invariance of a theory. The ideas which lead to a natural incorporation of massive gauge bosons will be outlined by the example of a charged particle with a spin 0 with the following Lagrangian density:

$$\mathcal{L} = [\partial^\mu \phi^\star(x)][\partial_\mu \phi(x)] - \mu^2 |\phi(x)|^2 - \lambda |\phi(x)|^4 \tag{2.1}$$

Here, $\phi(x)$ is a complex field with

$$\phi(x) = \frac{1}{\sqrt{2}}[\phi_1(x) + i\phi_2(x)] \tag{2.2}$$

The Lagrangian density 2.1 is required to be invariant under the local $U(1)$ phase transformation:

$$\phi(x) \rightarrow \phi'(x) = \phi(x)e^{i\alpha(x)}, \quad \phi^\star(x) \rightarrow \phi'^\star(x) = \phi^\star(x)e^{-i\alpha(x)}. \tag{2.3}$$

As outlined in Chapter 1, this can only be achieved by introducing a *massless* vector field by replacing the partial derivative ∂_μ by the covariant derivative $D_\mu = \partial_\mu - ieA_\mu$

The Lagrangian expressed in terms of the covariant derivative reads:

$$\mathcal{L} = [\partial^\mu + ieA^\mu]\phi^\star(x)[\partial_\mu - ieA_\mu]\phi(x) - \mu^2|\phi(x)|^2 - \lambda|\phi(x)|^4 - \frac{1}{4}F^{\mu\nu}F_{\mu\nu}, \tag{2.4}$$

where again $F^{\mu\nu}F_{\mu\nu}$ is the Lagrangian energy density of the free vector field. The term

$$\mathcal{V}(\phi) = \mu^2|\phi(x)|^2 + \lambda|\phi(x)|^4 \tag{2.5}$$

represents the potential energy density of the spin-0 field. In order to make the potential developing a minimum the first requirement is $\lambda > 0$. In Figure 2.1 the potential is illustrated for two choices of the sign of μ^2. In case $\mu^2 > 0$ the potential

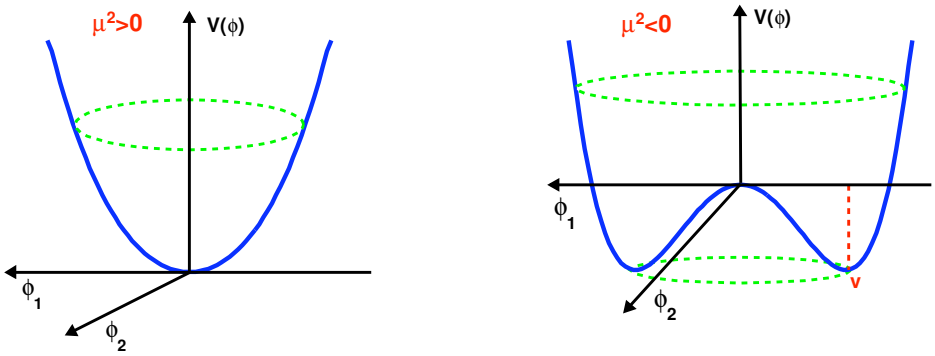

Figure 2.1: *Potential energy density* $\mathcal{V}(\phi) = \mu^2|\phi(x)|^2 + \lambda|\phi(x)|^4$ *for* $\lambda > 0$ *and opposite signs of the mass scale* μ^2. *For* $\mu^2 < 0$ *a circle of minima is developing at* $\mathcal{V}(\phi) = v$.

develops a unique minimum for the value $\mathcal{V}(\phi) = 0$ which corresponds to the vacuum state of the field with the vacuum expectation value $< 0|\phi(x)|0 >$. Trivially,

this vacuum state is also invariant under the phase transformation introduced in Equation 2.3. In case $\mu^2 < 0$, however, the potential develops two extreme values. One at $\mathcal{V}(\phi) = 0$ and a circle of minima for values

$$\mathcal{V}(\phi) = \phi_0 = \left(\frac{-\mu^2}{2\lambda}\right)^{1/2} e^{i\gamma(x)} = v e^{i\gamma(x)}.$$

In this case, the extreme value at $\mathcal{V}(\phi) = 0$ is a local maximum and the slightest perturbation makes the field leaving this state to change to the energetically favoured state with the vacuum expectation value $< 0|\phi(x)|0 >= v$. Along the circle, there is an infinite number of ground state possible for the field. Hence, the vacuum state is not invariant anymore against the gauge transformation. The situation in which the ground state of a system does not exhibit the same symmetry properties as its corresponding Lagrangian density is known as *spontaneous symmetry breaking*. The application of perturbation theory makes only sense for small changes w.r.t. to a stable state. Due to the phase invariance of the Lagrangian density the phase of the ground state can be chosen to be 0. The deviations from the stable ground state can be expressed through

$$\phi(x) = \frac{1}{\sqrt{2}}[v + \sigma(x) + i\eta(x)] \tag{2.6}$$

By this, the field is decomposed into a radial and a azimuthal part. Inserting this expression for the field, the Lagrangian density of Equation 2.1 is modified into, see e.g. [38]:

$$\begin{aligned}
\mathcal{L} = & \left[\frac{1}{2}(\partial_\mu\sigma)^2 - \frac{1}{2}(2\lambda v^2\sigma^2)\right] + \left[\frac{1}{2}(\partial_\mu\eta)^2\right] \\
& - \frac{1}{4}F^{\mu\nu}F_{\mu\nu} + \frac{1}{2}e^2v^2A_\mu A^\mu \\
& + ev(\partial_\mu\eta)A^\mu \\
& + \Big\{e[\sigma(\partial_\mu\eta) - \eta(\partial_\mu\sigma)]A^\mu + ve^2\sigma A_\mu A^\mu + \frac{e^2}{2}(\sigma^2+\eta^2)(A_\mu A^\mu) \\
& - v\lambda(\sigma^3 + \sigma\eta^2) - \frac{1}{4}\lambda(\sigma^4 + 2\sigma^2\eta^2 + \eta^4)\Big\} + \left(\frac{v^2\sqrt{\lambda}}{2}\right)
\end{aligned} \tag{2.7}$$

Upon inspection of the Lagrangian density 2.7 the following can be deduced:

- The expansion of the scalar field described by Equation 2.1 around the stable minimum gives rise to one massive scalar particle, corresponding to the field $\sigma(x)$, with mass $\sqrt{2\lambda}v$ and one massless scalar particle, corresponding to the field $\eta(x)$ which is a so-called (Nambu-)Goldstone Boson [39]. The massive scalar particle corresponds to the oscillations of the field in radial direction. As the potential increases at least quadratically in this direction, the appearance of a mass can be interpreted as the inertia with which the field reacts on this restoring force. The quanta of this field are thus massive spin-0 particles. As

the potential is constant in azimuthal direction there is no 'need' for an inertia of the field $\eta(x)$. Hence, the quanta of this field remain massless.

- The gauge field A_μ has acquired a mass:

$$m_A = ev. \tag{2.8}$$

The introduced mechanism has created a scenario with a stable vacuum of the scalar field $\sigma(x)$ and a massive vector boson. Despite of these achievements, the Lagrangian density has still several shortcomings:

- The massless scalar particle, the Goldstone boson, does not correspond to any observed particle in nature and there is nowadays no theory which requires the existence of such a particle.
- The term in the third row of Equation 2.7 is difficult to interpret. Being bilinear in the fields η and A_μ it does not correspond to an interaction term as it would contain an incomplete set of in and outgoing particles. It can therefore not be concluded that the Lagrangian density 2.7 describes a system of independent particles.
- The number of degrees of freedom have changed after spontaneous symmetry breaking! Originally there were

$$\begin{aligned} &2 \quad (\text{complex scalar field}) \\ &+2 \quad (\text{transverse polarisation of the massless photon}) \\ &\text{-----} \\ &=4. \end{aligned}$$

After the breaking of the symmetry there are:

$$\begin{aligned} &1 \quad (\sigma \text{ field}) \\ &1 \quad (\eta \text{ field}) \\ &+3 \quad (\text{massive vector field}) \\ &\text{-----} \\ &=5. \end{aligned}$$

These obvious shortcomings can be remedied by recognising that the imaginary part of the field definition in Equation 2.6 can be interpreted as the first series of the Taylor expansion of $e^{i\frac{\eta}{v}}$ according to:

$$\begin{aligned} (v+\sigma(x))e^{i\frac{\eta(x)}{v}} &\approx (v+\sigma(x))(1+i\frac{\eta(x)}{v}) \\ &= \underbrace{v+\sigma(x)+i\eta(x)}_{\phi(x)} + i\underbrace{\frac{\sigma(x)\eta(x)}{v}}_{\approx 0} \end{aligned} \tag{2.9}$$

The field $\eta(x)$ can thus be converted to be the phase transformation of an entirely real field of the form $v+\sigma(x)$. Again, the gauge invariance of the Lagrangian permits to choose the vacuum state of the system to lie along the real axis of Figure 2.1. It follows also from gauge invariance that the Lagrangian will be independent of the phase. Defining

$$\begin{aligned} \phi(x) &= \frac{1}{\sqrt{2}}(v+\sigma(x))e^{i\eta(x)/v} \text{ and thus} \\ A_\mu &\rightarrow A_\mu + \frac{1}{ev}\partial_\mu \eta, \end{aligned} \tag{2.10}$$

the Lagrangian density 2.7 can be expressed as

$$\begin{aligned} \mathcal{L} = &\left[\frac{1}{2}(\partial_\mu \sigma)^2 - \frac{1}{2}(2\lambda v^2 \sigma^2)\right] \\ &- \frac{1}{4}F^{\mu\nu}F_{\mu\nu} + \frac{1}{2}e^2 v^2 A_\mu A^\mu \\ &+ \left\{ v e^2 \sigma (A_\mu A^\mu) + \frac{1}{2}e^2\sigma^2(A_\mu A^\mu) - \lambda v \sigma^3 - \frac{1}{4}\lambda\sigma^4 \right\} \\ &+ \left(\frac{v^2\sqrt{\lambda}}{2}\right) \end{aligned} \tag{2.11}$$

It is now composed of a real massive scalar with a vacuum state which is invariant under the $U(1)$ phase transformation and a massive vector field A_μ. The Goldstone Boson does not appear anymore in the Lagrangian. It has been 'gauged away' into the *longitudinal* degree of freedom of the vector boson. In fact the mechanism at work is a generalisation of the Gupta-Bleuler mechanism [40] which in QED prevents the existence of scalar and massive photons. Here, the scalar degree of freedom is suppressed again, but the longitudinal degree of freedom is kept which is equivalent to a vector boson having acquired a mass. The total number of degrees of freedom is again four with one degree attributed to the scalar field and three degrees attributed to the *three* possible polarisation states of the vector field. The massive scalar field is called a *Higgs particle*. The procedure described in the previous is called the *Higgs Mechanism* [41]. The key points of this Higgs Mechanism and the main conclusions will be once more summarised in the following.

- The domain $\mu^2 < 0$ for the mass parameter of the scalar potential in the Lagrangian 2.7 results in a stable minimum different from zero. Regarding small changes of the field around that minimum leads the appearance of a massive scalar particle and a massless Goldstone boson
- The request for *local* gauge invariance of the Lagrangian leads to the appearance of massive vector or gauge bosons in the theory. At the same time, gauge invariance allows to interpret the field attributed to the Goldstone boson as the phase of the gauge transformation of a real field $\sigma(x)$. The procedure ends with *one* scalar particle and a massive gauge boson with three polarisation degrees of freedom.

- The Lagrangian in 2.11 does not reflect anymore the symmetry of the original Lagrangian as a $U(1)$ phase transformation would alter the Lagrangian. In this sense the symmetry is (spontaneously) broken. It would be, however more appropriate to say that the symmetry is *hidden* as a) it is derived from a Lagrangian with the given symmetry properties and b) it is still present in the dynamics of the Lagrangian given by the partial derivatives w.r.t. that field.

The Lagrangian contains tri-linear, σAA, and quadri-linear, i.e. $\sigma\sigma AA$ interactions between the gauge boson and the the scalar field σ. The coupling strengths of these interactions are proportional to the mass of the gauge boson and read:

$$g_{\sigma AA} = e^2 v = \frac{m_A^2}{v} \quad \text{and} \quad g_{\sigma\sigma AA} = e^2 = \frac{m_A^2}{v^2}. \tag{2.12}$$

Finally, the Lagrangian contains also triple and quartic self-interaction terms of the scalar field $\sigma(x)$. The self-couplings read

$$\begin{array}{ll} \lambda v & \text{for the triple coupling, and} \\ \frac{1}{4}\lambda & \text{for the quartic coupling.} \end{array} \tag{2.13}$$

The discussion conducted in this section describes a model which is not realised in nature. If there would be a scalar charged Higgs particle, the photon would have a mass which is according to current knowledge not the case. The discussed model is however excellent to introduce the main ideas of the Higgs Mechanism which can now be applied to other more complicated theories.

2.2 A Higgs Doublet - Particle Masses in the Electroweak Theory

As pointed out in Chapter 1, the need to generate massive vector bosons becomes apparent for the electroweak interactions. The way how this is realised is a straightforward application of what has been described in Section 2.1. Following the $SU(2)_L \times U(1)_Y$ symmetry of the electroweak theory, the minimal choice to create the Higgs Potential is a $SU(2)_L$ isospin *doublet* with hyper-charge $Y = 1$

$$\Phi = \begin{pmatrix} \phi^+ \\ \phi^0 \end{pmatrix} \quad \text{with} \quad \begin{array}{l} \phi^+ = (\phi_1 + i\phi_2)/\sqrt{2} \\ \phi^0 = (\phi_3 + i\phi_4)/\sqrt{2} \end{array} \tag{2.14}$$

with a vacuum expectation value of:

$$\phi_0 = \frac{1}{\sqrt{2}} \begin{pmatrix} 0 \\ v \end{pmatrix} \tag{2.15}$$

Proceeding as in Section 2.1, the field in Equation 2.14 can be expressed in terms of the vacuum expectation value and a set of real fields, $\sigma(x)$, $\eta_i(x)$:

$$\Phi = \frac{1}{\sqrt{2}} \begin{pmatrix} 0 \\ v + \sigma(x) \end{pmatrix} e^{\frac{\boldsymbol{\eta}\mathbf{t}}{v}} \tag{2.16}$$

with $t_i = \frac{1}{2}\tau_i$ being the $SU(2)_L$ generators associated with the weak isospin T. The vacuum expectation value 2.15 does not remain invariant under a phase transformation as in 2.16. On the other hand, it remains invariant after an electromagnetic gauge transformation according to

$$\phi_0 \rightarrow \phi_0' = \phi_0 e^{i\alpha Q} = \frac{1}{\sqrt{2}} \begin{pmatrix} 0 \\ v \end{pmatrix} e^{i\alpha \frac{\tau_3 - Y\cdot 1}{2}} \phi_0 \approx \left(1 + i\alpha \begin{pmatrix} 1 & 0 \\ 0 & 0 \end{pmatrix}\right) \phi_0 = \phi_0. \quad (2.17)$$

In that way, the $SU(2)_L \times U(1)_Y$ symmetry is spontaneously broken to the $U(1)_Q$ symmetry of the electromagnetic interaction which ensures that the photon remains massless. The introduced doublet in 2.14 has four degrees of freedom, two charged ones and two neutral ones. By setting the real parameters in 2.16 to zero, the three Goldstone bosons associated with the broken $SU(2)_L \times U(1)_Y$ symmetry are absorbed into the longitudinal degrees of freedom of the three vector bosons $\mathrm{W}^{\pm}$ and Z which become therefore massive. The remaining degree of freedom can be associated with a neutral scalar boson $\sigma(x)$, the *Higgs boson* H of the electroweak theory. The predicted masses are:

$$m_\gamma = 0, \quad m_{\mathrm{W}^{\pm}} = \frac{gv}{2}, \quad m_{\mathrm{Z}} = \frac{v\sqrt{g^2 + g'^2}}{2}. \quad (2.18)$$

Similar to Equation 2.12, the couplings of the massive vector bosons to the Higgs boson are given to be

$$g_{HVV} = e^2 v = \frac{m_V^2}{v} \quad \text{and} \quad g_{HHVV} = e^2 = \frac{m_V^2}{v^2} \quad \text{with} \quad V = W, Z. \quad (2.19)$$

The measurement of the couplings between the vector bosons and Higgs boson constitute one of the most important measurements to be conducted after the discovery of the Higgs boson. As will be explained below, such a measurement is particularly sensitive to physics beyond the Standard Model.

Fermion Masses

So far only the creation of masses of vector bosons have been addressed. It is however an experimental fact that also fermions do have masses. For massless particles the helicity is a Lorentz invariant quantity. A change of the helicity of a particle is thus equivalent to the acquiring of mass. This change of helicity can be accomplished by the interaction of a massless particle with the Higgs field which in turn leads to an effective mass of the particle. While this coupling to the Higgs field for the ad initio massless bosons appears "naturally" by the Higgs Mechanism, the coupling of e.g. electrons to the Higgs Field is introduced by hand in a gauge invariant way as follows:

$$\mathcal{L}_{mass,f} = \lambda_e \left[(\bar{\nu}_e, \bar{e})_L \begin{pmatrix} \phi^+ \\ \phi^0 \end{pmatrix} e_R + \bar{e}_R (\phi^+, \phi^0) \begin{pmatrix} \nu_e \\ e \end{pmatrix} \right], \quad (2.20)$$

with λ_e being the *Yukawa coupling* parameter. Replacing the doublet in 2.20 with the one in 2.16 yields the following expression:

$$\mathcal{L}_{mass,f} = -m_e(\bar{e}_L e_R + \bar{e}_R e_L) - \frac{m_e}{v}(\bar{e}_L e_R + \bar{e}_R e_L)h, \quad (2.21)$$

with

$$m_e = \frac{\lambda_e v}{\sqrt{2}}. \tag{2.22}$$

The coupling of the fermions to the Higgs doublet has thus lead to a mass term for the electrons. The value of the mass is not predicted by the theory. It has to be measured in the experiment. The second term in 2.21 however *predicts* the coupling of the electron to the Higgs boson. This coupling is exactly proportional to the mass of the electron, a fact which repeats when the mechanism is applied for the other fermions. Measuring the coupling of the Higgs to fermions will thus constitute another most crucial test of the theory if the Higgs boson is discovered.

2.3 Models with Two Higgs Doublets

Already in the Standard Model there is no fundamental reason to assume that the Higgs sector must be minimal, i.e. consists of one scalar doublet only. The simplest extension which is compatible with gauge invariance is the so-called *Two Higgs Doublet Model* or *2DHM*. In this model a second doublet is added with the same quantum numbers as the one defined in Equation 2.14.

$$\Phi_1 = \begin{pmatrix} \phi_1^+ \\ \phi_1^0 \end{pmatrix} \quad \text{and} \quad \Phi_2 = \begin{pmatrix} \phi_2^+ \\ \phi_2^0 \end{pmatrix} \tag{2.23}$$

For the further discussion it will be assumed that no CP violation is introduced by the two doublets.

Due to spontaneous symmetry breaking, the potential associated with the fields in Equation 2.23 develops a minimum for:

$$\phi_{0,1} = \frac{1}{\sqrt{2}} \begin{pmatrix} 0 \\ v_1 \end{pmatrix}, \quad \text{and} \quad \phi_{0,2} = \frac{1}{\sqrt{2}} \begin{pmatrix} 0 \\ v_2 \end{pmatrix}. \tag{2.24}$$

A very important parameter in 2DHM models is the ratio of the vacuum expectation values which is defined as:

$$\tan\beta = \frac{v_1}{v_2}. \tag{2.25}$$

Expanding the fields around the minima, three of eight scalar degrees of freedom are absorbed into the massive vector bosons $W^{\pm}$ and Z. The remaining five degrees of freedom give rise to *five* Higgs Particles:

- One CP odd scalar: A^0.
- A pair of charged Higgs bosons: $H^{\pm}$.
- Two CP even scalars: h^0,H^0.

The masses of the CP odd and the charged Higgs bosons are

$$m^2_{\mathrm{A}^0} = \frac{m^2_{12}}{\sin\beta\cos\beta} - \frac{1}{2}(v_1+v_2)^2(2\lambda_5 + \lambda_6\tan^{-1}\beta + \lambda_7) \tag{2.26}$$

$$m^2_{\mathrm{H}^\pm} = m^2_{\mathrm{A}^0} + \frac{1}{2}(v_1+v_2)^2(\lambda_5 - \lambda_4), \tag{2.27}$$

where m_{12} is a mass parameter appearing in the potential associated with the scalar fields in 2.23. The λ_i are the corresponding constants for the couplings among the Higgs fields.

The mass eigenstates of the two neutral CP even scalars mix according to the following matrix:

$$\begin{aligned}\mathcal{M}^2 = m^2_{\mathrm{A}^0} &+ \begin{pmatrix} s^2_\beta & -s_\beta c_\beta \\ -s_\beta c_\beta & c^2_\beta \end{pmatrix} \\ &+ (v_1+v_2)^2 \begin{pmatrix} \lambda_1 c^2_\beta + 2\lambda_6 s_\beta c_\beta + \lambda_5 s^2_\beta & (\lambda_3+\lambda_4)s_\beta c_\beta + \lambda_6 c^2_\beta + \lambda_7 s^2_\beta \\ -(\lambda_3+\lambda_4)s_\beta c_\beta + \lambda_6 c^2_\beta + \lambda_7 s^2_\beta & \lambda_2 s^2_\beta + 2\lambda_7 s_\beta c_\beta + \lambda_5 c^2_\beta \end{pmatrix}\end{aligned} \tag{2.28}$$

where $s_\beta = \sin\beta$ and $c_\beta = \cos\beta$. The eigenvalues of the matrix 2.28 yield the masses of the two neutral CP even Higgs bosons

$$m^2_{\mathrm{h}^0,\mathrm{H}^0} = \frac{1}{2}\left(\mathcal{M}^2_{11} + \mathcal{M}^2_{22} \pm \sqrt{(\mathcal{M}^2_{11} - \mathcal{M}^2_{22})^2 + 4(\mathcal{M}^2_{12})^2}\right) \tag{2.29}$$

The mixing angle α is obtained via:

$$\sin 2\alpha = \frac{2\mathcal{M}^2_{12}}{\sqrt{(\mathcal{M}^2_{11} - \mathcal{M}^2_{22})^2 + 4(\mathcal{M}^2_{12})^2}} \tag{2.30}$$

$$\cos 2\alpha = \frac{\mathcal{M}^2_{11} - \mathcal{M}^2_{12}}{\sqrt{(\mathcal{M}^2_{11} - \mathcal{M}^2_{22})^2 + 4(\mathcal{M}^2_{12})^2}} \tag{2.31}$$

The CP conserving 2HDM introduces six additional free parameters:

- The mixing angle α.
- The ration of the vacuum expectation values, $\tan\beta$
- Four Higgs boson masses m_{A^0}, m_{h^0}, m_{H^0} and $m_{\mathrm{H}^\pm}$.

The masses of the Standard Model vector bosons become:

$$m_{\mathrm{W}} = g\frac{\sqrt{v_1^2+v_2^2}}{2}, \quad m_{\mathrm{Z}} = \frac{\sqrt{(v_1^2+v_2^2)(g^2+g'^2)}}{2}, \quad M_\gamma = 0 \tag{2.32}$$

The extension of the Higgs sector from one to five Higgs particles alter the couplings of the Higgs bosons to the Standard Model vector bosons. The couplings depend now not only on the mass but on an additional coupling factor given by the

introduced angles α and β. In addition, new tri-linear couplings between the neutral Higgs Particles and the vector bosons are introduced. While the coupling constants to the bosons are universal, the altered couplings to fermions are model dependent. The scalar doublets can be arranged such that one of the doublets couples only to down type quarks and charged leptons while the other one couples only to the up-type quarks. This model is also known as the 2DHM *Type II* and has e.g. the advantage that is suppresses Flavor Changing Neutral Currents which have not been observed so far. The coupling factors to the various particle types are summarised in Table 2.1.

	h	H	A
$W^{\pm}$	$\sin(\beta-\alpha)$	$\cos(\beta-\alpha)$	0
Z	$\sin(\beta-\alpha)$	$\cos(\beta-\alpha)$	0
up-type quarks	$\cos\alpha/sin\beta$	$\sin\alpha/\sin\beta$	$\cot\beta$
down-type quarks	$\sin\alpha/cos\beta$	$\cos\alpha/\cos\beta$	$\tan\beta$
charged leptons	$\sin\alpha/\cos\beta$	$\cos\alpha/\cos\beta$	$\tan\beta$

Table 2.1: *Modifications of the couplings between the Standard Model gauge bosons and neutral Higgs bosons as function of the parameters α and β introduced in the 2DHM Type II model. For a CP-conserving 2DHM, the CP-odd Higgs does not couple to the gauge bosons.*

2.4 Towards an Extension of the Standard Model - Supersymmetrie

It is well justified to assume that the Standard Model is only an effective theory which is only valid up to some scale Λ. The first reason for this assumption is that it does not provide a mechanism to incorporate gravity. On the other hand it is obvious that latest at energy scales of the order of Λ_P, gravitational effects cannot be neglected. A second reason is the quest for an unification of the forces into one. Grand Unification Theories [43] provide a framework which implies that the coupling constants of the electromagnetic, the weak and the strong force approach each other at a scale $\Lambda_{GUT} \sim 10^{14} - 10^{16}\,\text{GeV}$. However, as can be seen in the left part of Figure 2.2, the coupling constants do not meet each other at one single point which indicates one shortcoming of the Standard Model when extrapolating it to high energies.

If the Standard Model is only valid up to some scale, then higher corrections do not lead to satisfactory results. As shown in Section 2.1, spontaneous symmetry breaking gives a mass $m_{\text{H}}^0 = \sqrt{2\lambda}v$ to the Higgs boson. Higher order processes like those shown in Figure 2.3 contribute corrections to the bare value of the mass which turn out to be quadratically divergent. The assumption of the validity of the Standard Model up to some scale Λ implies to cut off the loop integrals associated

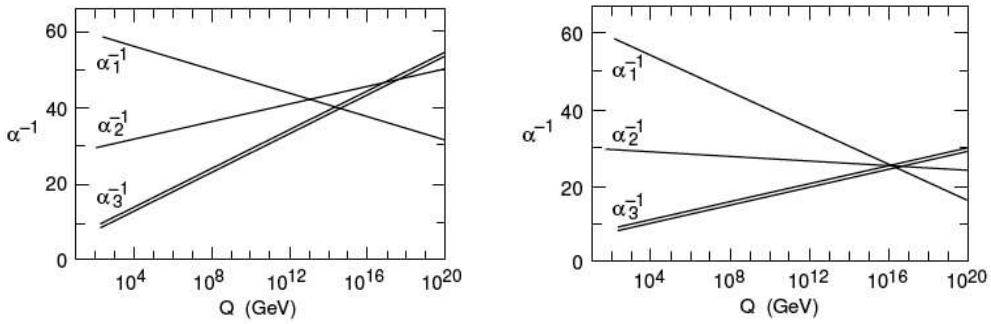

Figure 2.2: *Running of the gauge couplings as a function of the energy. The left part indicates the case for the Standard Model where the coupling constants miss each other. The right part indicates the case for an extension of the Standard Model as w.g. given by the MSSM (see text).*

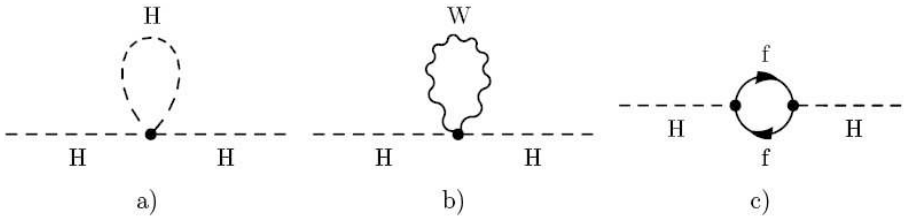

Figure 2.3: *One loop corrections to the Higgs boson mass arising from a) Higgs boson loop; b) gauge boson loop; c) fermion loop.*

with the corrections at that scale. The corrected Higgs mass then reads [42]

$$m_{\mathrm{H}}^2 = (m_{\mathrm{H}}^0)^2 + \frac{3\Lambda^2}{8\pi^2 v^2}[m_{\mathrm{H}}^2 + 2m_{\mathrm{W}}^2 + m_{\mathrm{Z}}^2 - 4m_t^2] \tag{2.33}$$

If the Standard Model would be valid up to Λ_{GUT} or even Λ_P, then these quantum corrections can be very large. A fine arrangement of 16 digits between the bare Higgs mass and the corrected mass would be needed to render a Higgs boson between 100 GeV and 1 TeV, which is the currently favoured region for the value of the Higgs mass within the Standard Model, see Section 2.6. The need for a fine arrangement is also known as the *naturalness* or *hierarchy* problem. Although radiative corrections for fermions and vector bosons diverge only logarithmically, the whole particle spectrum is sensitive to the choice of the scale Λ since all particles gain their mass by the interaction with the scalar Higgs boson.

Supersymmetry, or short SUSY, is a quantum field theory that provides means to remedy the hierarchy problem and to address other open questions listed Section 1.6. It introduces a new boson for each fermion and vice versa. Formally Supersymmetry

is realised by defining an operator Q which transforms Bosons $|B>$ into fermions $|f_\alpha>$ and vice versa, i.e.

$$Q_\alpha|f_\alpha>=|B> \quad Q_\alpha|B>=|f_\alpha> \tag{2.34}$$

The new particles do contribute with *opposite* sign to the loop corrections associated with the diagrams in Figure 2.3. Hence, the quadratically divergent terms are largely cancelled. The new particles also alter the energy dependency of the coupling constants such that they meet at one point at the scale $\Lambda_{GUT} \approx 10^{16}$ GeV, see Figure 2.2. The numerous advantages of SUSY are diluted by the fact that as of today no super-symmetric particle has been observed. Hence, SUSY must be broken at energy scales accessible with experiments described in Chapter 1. Several proposals to achieve this symmetry breaking do exist [44, 45]:

- *Spontaneous* flavour-blind SUSY breaking in a hidden sector, typically at the GUT scale, mediated e.g. by gravity as is the case for mSUGRA. For an overview see [44].

- *Direct* SUSY breaking by adding a term to the super-symmetric Langrangian which allows for soft SUSY breaking. This means that only logarithmically divergent terms are included instead of quadratically divergent terms as in case of the Standard Model Higgs boson. This proposal is realised in the *Minimal Supersymmetric Model* or *MSSM*.

The latter will be introduced in the following. In particular, the impact on the Higgs sector will be emphasised

The Higgs Sector in the Minimal Supersymmetric Model

A detailed discussion of the MSSM can be found elsewhere [47]. Here, only the most important features as relevant for this document are summarised. In the MSSM each fermion of the Standard Model gets assigned *exactly* one bosonic partner and each boson of the Standard Model gets also assigned *exactly* one fermionic partner. A most notables feature of the MSSM is that its Lagrangian contains only terms respecting a new discrete quantum number

$$R = (-1)^{3(B-L)+s} \tag{2.35}$$

which is 1 for each Standard Model particle and -1 the super-partners. As a consequence super-symmetric particles can only be produced in pairs and the lightest super-symmetric particle is stable. The MSSM thus provides a candidate for cosmic dark matter.

The Higgs Sector of the MSSM is a 2HDM of Type II, see Section 2.3, with a Higgs potential whose dimension-four terms respect supersymmetry [46]. This allows for putting further constraints on the parameters defined in Equations 2.27

to 2.31. Within the MSSM the masses of the CP odd and Charged Higgs read

$$m^2_{\mathrm{A}^0} = m^2_{12}(\tan\beta + \cot\beta) \tag{2.36}$$
$$m^2_{\mathrm{H}^\pm} = m^2_{\mathrm{A}^0} + m^2_{\mathrm{W}}. \tag{2.37}$$

The masses of the two neutral CP even Higgs scalar are modified into:

$$m^2_{\mathrm{h}^0,\mathrm{H}^0} = \frac{1}{2}\left(m^2_{\mathrm{A}^0} + m^2_{\mathrm{Z}} \pm \sqrt{(m^2_{\mathrm{A}^0} + m^2_{\mathrm{Z}})^2 + (2m_{\mathrm{Z}} m_{\mathrm{A}^0}\cos 2\beta)^2}\right), \tag{2.38}$$

with the mixing angle

$$\cos 2\alpha = -\cos 2\beta \frac{m^2_{\mathrm{A}^0} - m^2_{\mathrm{Z}}}{m^2_{\mathrm{H}^0} - m^2_{\mathrm{h}^0}} \tag{2.39}$$
$$\sin 2\alpha = -\sin 2\beta \frac{m^2_{\mathrm{H}^0} + m^2_{\mathrm{h}^0}}{m^2_{\mathrm{H}^0} - m^2_{\mathrm{h}^0}} \tag{2.40}$$

Within the MSSM there are only two free parameters in the Higgs sector, typically chosen to be m_A and $\tan\beta$. On tree level, the MSSM predicts a *light* Higgs boson with a mass $m_{\mathrm{h}^0} \leq m_{\mathrm{Z}}|cos2\beta| \leq m_{\mathrm{Z}}$. Such a particle would have been detected at LEP. It is however interesting to note that radiative corrections including the top quark and its super-partner may drive the mass of the lightest super-symmetric Higgs boson up to a mass of 135 GeV which is well accessible by the LHC or a future lepton collider. In the next section the production mechanisms of Higgs bosons at lepton colliders will be introduced.

2.5 Higgs Boson Production at Lepton Colliders

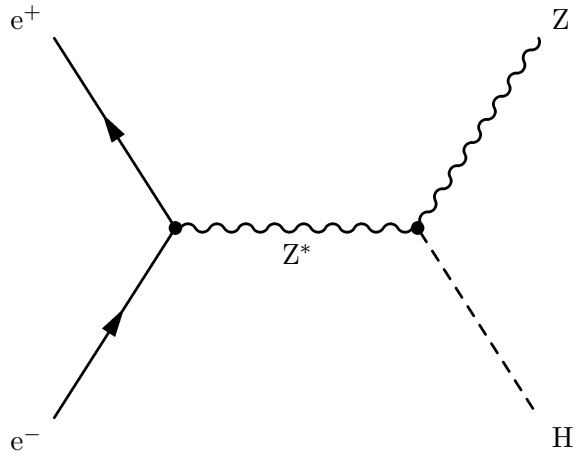

Figure 2.4: *Feynman diagram for the Higgs-strahlung process at lepton colliders. The Higgs boson* H *is radiated off a virtual* Z *boson created in the electron-positron annihilation. The final state consists of a* Z *boson and the Higgs boson.*

If the mass of the Higgs boson is comparable to the centre-of-mass energy of the e^+e^- collision, i.e. $m_H \approx \sqrt{s}$, the production of the Standard Model Higgs boson is expected to happen mainly through the *Higgs-strahlung* process, see Figure 2.4. Here, the electron and the positron annihilate into a virtual Z boson which goes on-shell via radiation of a Higgs boson. In lowest order, the cross section of the Higgs-strahlung process is given by the following formula:

$$\sigma_{HZ}(e^+e^- \to ZH) = \frac{G_F^2 m_Z^4}{96\pi s}(g_{Ve}^2 e + g_{Ae}^2)\lambda_{2b}^{1/2}\frac{\lambda_{2b} + 12m_Z^2/s}{(1 - m_Z^2/s)^2}. \tag{2.41}$$

Here, $\sqrt{s}$ is the centre-of-mass energy, g_{Ve} and g_{Ae} are the couplings of the initial state electron to the Z boson and $\lambda_{2b} = (1 - m_H^2/s - m_Z^2/s)^2 - 4m_H^2 m_Z^2/s^2$ is the two-particle phase space function. The maximum of the cross section is reached at $\sqrt{s} \approx m_Z + \sqrt{2}m_H$ and vanishes according to $1/s$ in the asymptotic limit. Note, that the formula 2.41 does not take into account the effect of a finite width of the Z boson. Therefore, the predicted cross section approaches 0 close to the kinematic limit of ZH production. Figure 2.5 illustrates the behaviour of the cross section as a function of the centre-of-mass energy and the value of the mass of the Higgs boson.

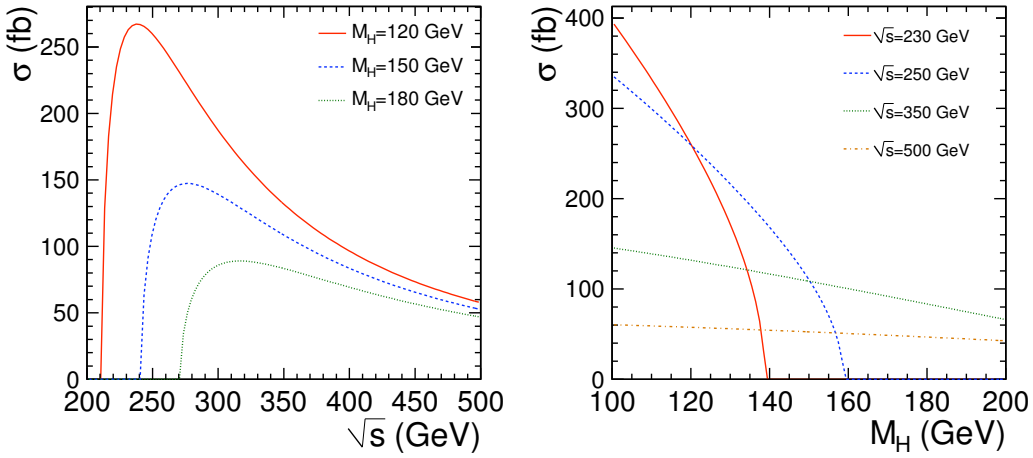

Figure 2.5: *Cross section (σ) of the Higgs-strahlung process in the Standard Model, as a function of centre-of-mass energy ($\sqrt{s}$) (left) and as a function of Higgs mass (m_H) (right).*

Figure 2.6 depicts the generation of the Higgs boson via WW fusion and ZZ fusion. Their cross section exhibits an energy dependence $\sigma \sim m_V^{-2}\log(s/m_H)$ with V = W, Z. These processes become hence important in the limit $m_H/\sqrt{s} \ll 1$. The ZZ fusion is however suppressed since the neutral current couplings are smaller than the charged current couplings. For a Higgs boson mass in the range $100 \lesssim$

$m_{\mathrm{H}} \lesssim 1000\,\mathrm{GeV}$ the WW fusion process dominates the Higgs boson production cross section for centre-of-mass energies $\sqrt{s} > 500\,\mathrm{GeV}$.

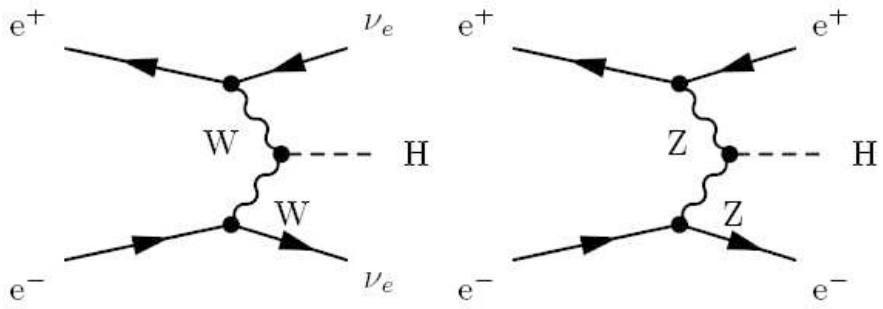

Figure 2.6: *Higgs production by the fusion of the heavy vector bosons* WW *and* ZZ*. Compared with the Higgs-strahlung process their contribution to Higgs production is suppressed by an additional power in the electroweak coupling. Their contribution to Higgs boson production increase, however, with increasing centre-of-mass energy.*

For the Higgs-strahlung, the angular distribution of the final state Higgs and Z bosons is determined by the quantum numbers of the Higgs boson, $J^P = 0^+$, in terms of spin and parity. The differential cross section reads:

$$\frac{\mathrm{d}\sigma_{\mathrm{HZ}}(\mathrm{e^+e^-} \to \mathrm{ZH})}{\mathrm{d}\cos\theta} \sim \lambda_{2b}^2 \sin^2\theta + 8m_{\mathrm{Z}}^2/s \;, \tag{2.42}$$

Here, θ is the polar angle in the centre-of-mass frame of the $\mathrm{e^+e^-}$-collision between the Higgs boson and the electron beam axis. In the asymptotic limit $s \gg m_{\mathrm{Z}}^2$ the Z boson is produced in a state of longitudinal polarisation [48]. In that case, the expansion of the final state into a sum of orbital momentum eigenstates receives only contributions from terms $\sim \sin^2\theta$. At the production threshold, the differential cross section gets independent of θ. The development of the angular distribution is depicted in Figure 2.7. Note, that if on the other hand a pseudo-scalar, i.e. $J^P = 0^-$, would be produced in association with the Higgs, the Z would be produced in a transversely polarised state and the angular distribution would be proportional to $(1 + \cos^2\theta)$ [50].

The lifetime of the Higgs Boson depends on its mass m_{H}. The heavier the Higgs boson is, the more decay channels open and therefore the larger the decay width gets. In turn, the lifetime of the Higgs boson increases with decreasing m_{H}. For $m_{\mathrm{H}} \approx 100\,\mathrm{GeV}$ the decay width of the Higgs is expected to be of the order of a few MeV. Examples for Higgs boson decays are given in Figure 2.8.

From the Yukawa couplings, the partial decay widths of the Higgs boson to fermions can be derived. The partial decay width of the Standard Model Higgs boson into fermions reads on tree level [42]:

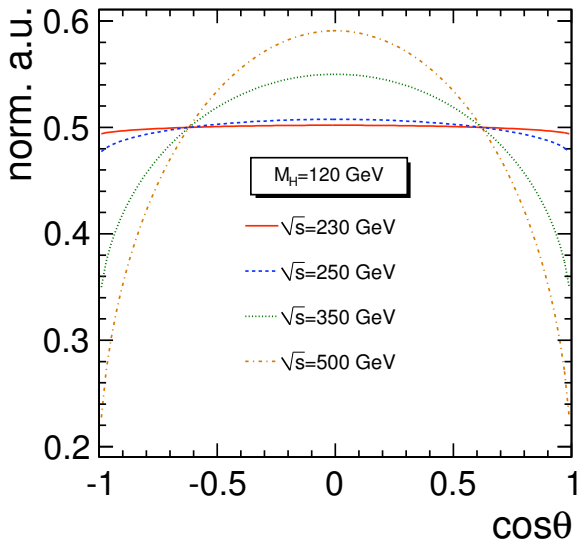

Figure 2.7: *Angular distribution of Higgs-strahlung* $e^+e^- \to HZ$ *as a function of* $cos\theta$ *for* $m_H = 120$ GeV *for different centre-of-mass energies . The angular dependency approaches a* $\sin^2\theta$ *shape with increasing centre-of-mass energy since the* Z *boson is preferably produced in a longitudinal polarisation mode at energies* $\sqrt{s} \gg m_Z$.

$$\Gamma(H \to f\bar{f}) = \frac{g_{Hff}^2}{4\pi}\frac{N_C}{2}M_H\left(1-\frac{4m_f^2}{M_H^2}\right)^{3/2}, \tag{2.43}$$

where N_C is a colour factor which is $N_C = 1$ for leptons and $N_C = 3$ for coloured quarks.

The partial widths for a Higgs boson decaying into two real gauge bosons, $H \to VV$ with $V = W$ or Z, are given on tree level by [42]

$$\Gamma(H \to VV) = \frac{G_F m_H^3}{16\sqrt{2}\pi}\,\delta_V\,\sqrt{1-4x}\,(1-4x+12x^2)\,, \quad x = \frac{M_V^2}{M_H^2} \tag{2.44}$$

with $\delta_W = 2$ and $\delta_Z = 1$. The latter become dominant if the mass m_H of the Higgs boson is larger than 140 GeV.

The branching ratios for the Higgs boson decaying into Standard Model fermions and massive vector bosons and the resulting total decay width are shown in Figure 2.9 as a function of the mass of the Higgs boson.

At tree level, no decays into gluons of photons occur. These gauge bosons can, however, be produced at one loop level as shown in Figure 2.8.

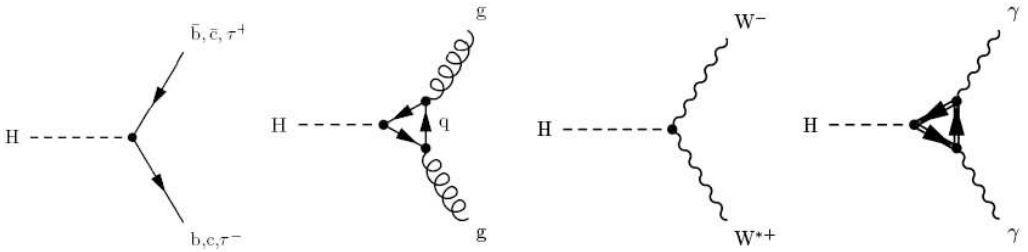

Figure 2.8: *Decay modes of the Higgs boson. The decay into gluons happens via heavy quark loops. Decays into photons are realised via* W *loops.*

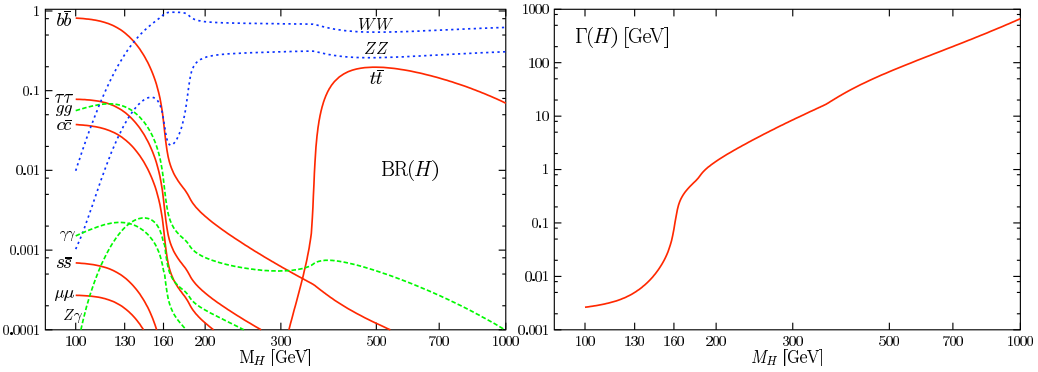

Figure 2.9: *The branching ratios (left) and the total decay width (right) of the Standard Model Higgs boson as a function of its mass [42].*

Production of Neutral Higgs bosons in the 2HDM

In the case of two Higgs doublets, the production of the light and heavy neutral CP even Higgs Bosons via radiation of the Z boson

$$\mathrm{e^+e^-} \rightarrow \mathrm{Z^*} \rightarrow \mathrm{hZ(HZ)} \tag{2.45}$$

is complemented by the associated Higgs pair production.

$$\mathrm{e^+e^-} \rightarrow \mathrm{Z^*} \rightarrow \mathrm{hA(HA)} \tag{2.46}$$

The production cross sections are related to the Higgs-strahlung cross section of the Standard Model as follows:

$$\begin{aligned} \sigma_{\mathrm{hZ}} &= \sin^2(\beta-\alpha)\sigma_{\mathrm{HZ}}^{SM} \\ \sigma_{\mathrm{HZ}} &= \cos^2(\beta-\alpha)\sigma_{\mathrm{HZ}}^{SM} \\ \sigma_{\mathrm{hA}} &= \cos^2(\beta-\alpha)\bar{\lambda}\sigma_{\mathrm{HZ}}^{SM} \\ \sigma_{\mathrm{HA}} &= \sin^2(\beta-\alpha)\bar{\lambda}\sigma_{\mathrm{HZ}}^{SM} \end{aligned} \tag{2.47}$$

The factor $\bar{\lambda}$ accounts for the different behaviour near the kinematic threshold. As can be seen, the parameters introduced by the choice of two Higgs doublets

modify the production rate of the associated Higgs bosons. Thus, in case of the observation of a 'Higgs like' particle, the comparison with the expected production rate from the Standard Model bears crucial information for new physics. The angular dependence of the production cross section is given as:

$$\frac{\mathrm{d}\sigma}{\mathrm{d}\cos\theta} \sim \begin{cases} \lambda_{2b}^2 \sin^2\theta + 8m_\mathrm{Z}^2/s & \text{for} \quad \mathrm{e^+e^-} \to \mathrm{Z^*} \to \mathrm{hZ(HZ)} \quad \text{and,} \\ \sin^2\theta & \text{for} \quad \mathrm{e^+e^-} \to \mathrm{Z^*} \to \mathrm{hA(HA).} \end{cases} \tag{2.48}$$

The difference in the angular distribution can be explained by the fact that the final state of the second reaction is composed of two spin-0 particles only.

2.6 Theoretical and Experimental bounds on the Higgs Boson Mass

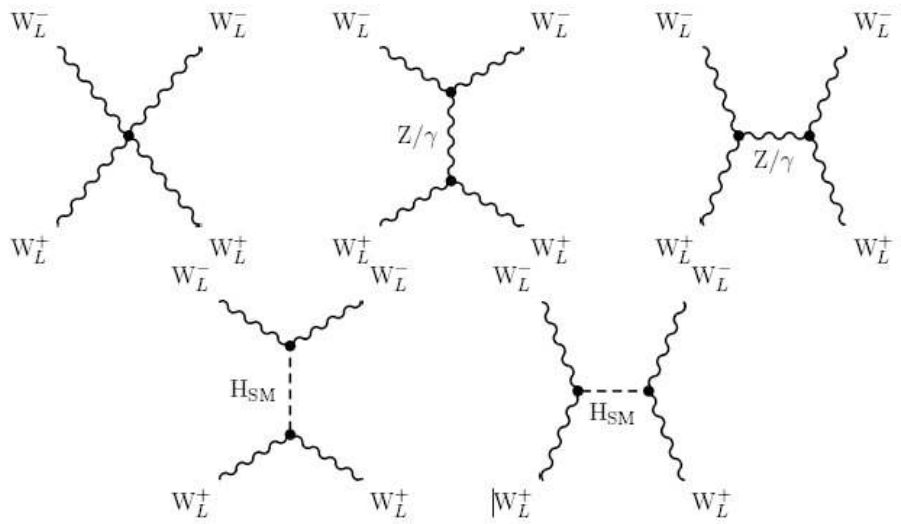

Figure 2.10: *Feynman Graphs contributing to* $\mathrm{W_L W_L}$ *scattering. The violation of unitarity for* $\sqrt{s} \to \infty$*, created by the upper graphs, is prevented by the exchange of the Higgs boson as shown in the lower graphs.*

The following discussion on bounds on the Higgs boson mass will be led within the Standard Model and that it remains valid up to a mass scale Λ at which gravitational effects cannot longer be neglected. It follows largely the discussion in [48]. Without the existence of a scalar Higgs particle, the amplitude of longitudinal W scattering would violate unitarity for $\sqrt{s} \to \infty$. The contributions to the longitudinal W scattering amplitude including the exchange of the Higgs boson are shown in Figure 2.10. The cross section is expected however to remain well within the unitarity bounds for Higgs mass values well below $m_\mathrm{H} \leq 1.2\,\mathrm{TeV}$ [49]. Taking also final states with longitudinally polarised Z boson pairs and Higgs pairs into account,

the bound can be refined to $m_{\mathrm{H}} \leq 1\,\mathrm{TeV}$. If there is no Higgs at all or the Higgs is heavier than approximately 1 TeV, a strong force between the gauge bosons has to be considered.

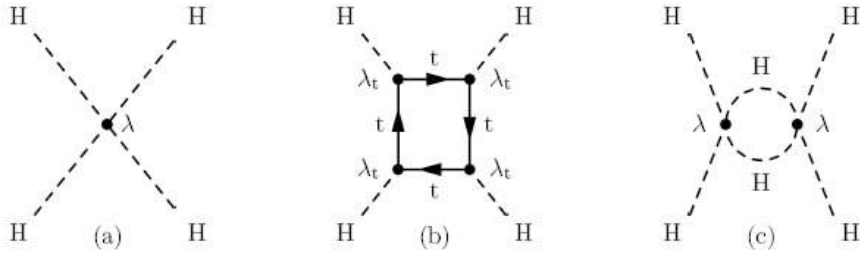

Figure 2.11: *Leading order (a) and dominant loop corrections including a Higgs boson (b) and a top quark (c) loop to the Higgs self coupling process.*

Further bounds can be derived when regarding higher order contributions to the Higgs self coupling as displayed in Figure 2.11. In this case, the quartic coupling constant λ gets scale dependent and dependent on the Yukawa coupling to the top quark. For a heavy Higgs mass, the correction containing the top quark loop can be neglected which has the consequence that the coupling constant would grow to infinity with increasing energy giving rise to infinitely strong interactions. From conventional $\lambda\phi^4$ theory the functional dependence of λ on a mass parameter μ_r^2 is given to be

$$\lambda(\mu_r^2) = \frac{\lambda(v^2)}{1 - \frac{3\lambda(v^2)}{8\pi^2}\log\frac{\mu_r^2}{v^2}}\,, \tag{2.49}$$

which, using $\lambda(v^2) = m_{\mathrm{H}}^2/2v^2$, can be re-written into:

$$m_{\mathrm{H}}^2 = \frac{v^2}{\frac{1}{2\lambda(\mu_r^2)} + \frac{3}{8\pi^2}\log(\frac{\mu_r^2}{v^2})}\,. \tag{2.50}$$

Requiring finally $\lambda(\Lambda) < \infty$ leads to an *upper* bound on the Higgs mass which reads:

$$m_{\mathrm{H}}^2 \leq \frac{v^2}{\frac{3}{8\pi^2}\log(\frac{\Lambda^2}{v^2})}\,. \tag{2.51}$$

If on the other hand the Higgs is too light, the coupling constant will take a negative slope with increasing energy up to the point where it turns negative. At this point the potential would no longer allow for a stable ground state. The negative slope can only be counterbalanced by a minimum value of the Higgs boson mass. Again, this value depends on the cut-off Λ. The Figure 2.12 summarises the discussion before and shows upper and lower bounds as a function of the cut-off scale Λ for a top quark mass of $\mathrm{m_t} = 175\,\mathrm{GeV}$. It is visible that for values of the order

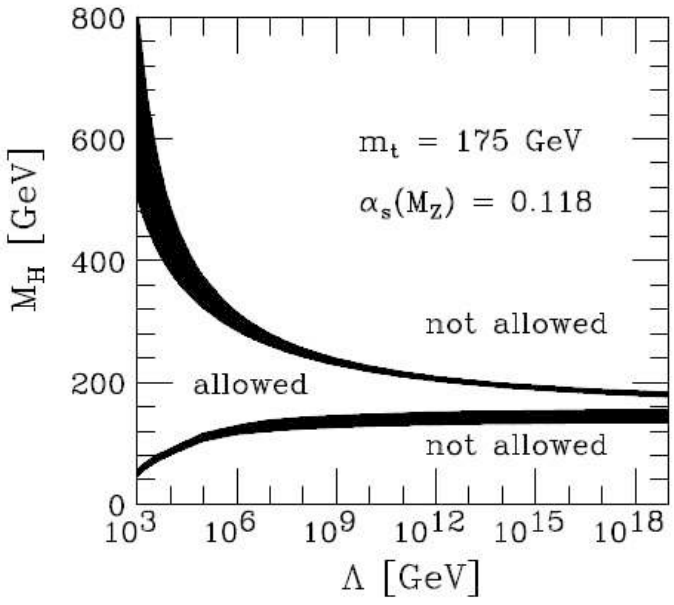

Figure 2.12: *Upper and lower bounds on the Higgs mass from corrections to the Higgs self-coupling process. The upper bound is given by the requirement of a small value of the quartic coupling λ (perturbative bound) while the lower bound is given by allowing only positive values for λ (stability bound). The figure is taken from [53].*

of $\Lambda = 10^{19}$ GeV, the allowed mass of the Higgs boson is restricted to a very small window of $130 \leq m_{\mathrm{H}} \leq 190$ GeV. Any deviation from these or similar values would implicate the existence of the new physics below the GUT scale. It should be noted that the detailed value depends considerably on the mass of the top quark and of the value of the strong coupling constant α_s. A detailed discussion on current bounds on the Higgs boson mass can be found in [51]. Note that in [52] it is argued that the stability requirement which leads to the *lower* bound on the Higgs mass appears as an intrinsic property of the theory rather than as an additional constraint.

The Higgs boson interacts predominantly with heavy particles. Although it has not been observed so far, the Higgs boson may contribute to the measured masses of particles via virtual higher order corrections. Due to its preference for heavy particles it is straightforward to understand that in particular the measured masses of the W boson and the top quark allow for the determination of constraints on the mass of the Higgs Boson. The Figure 2.13 [19] shows the uncertainties on the 68% confidence level of the top mass and the W mass. The green band shows the prediction of these masses based on the Standard Model for various Higgs Masses using the world average of G_F. The prediction does not take into account values of the Higgs mass already excluded by LEP and recently by Tevatron, see below. The measured values of m_{W} and m_t agree within one standard deviation with the predictions derived from low Higgs masses. In total the current electroweak precision

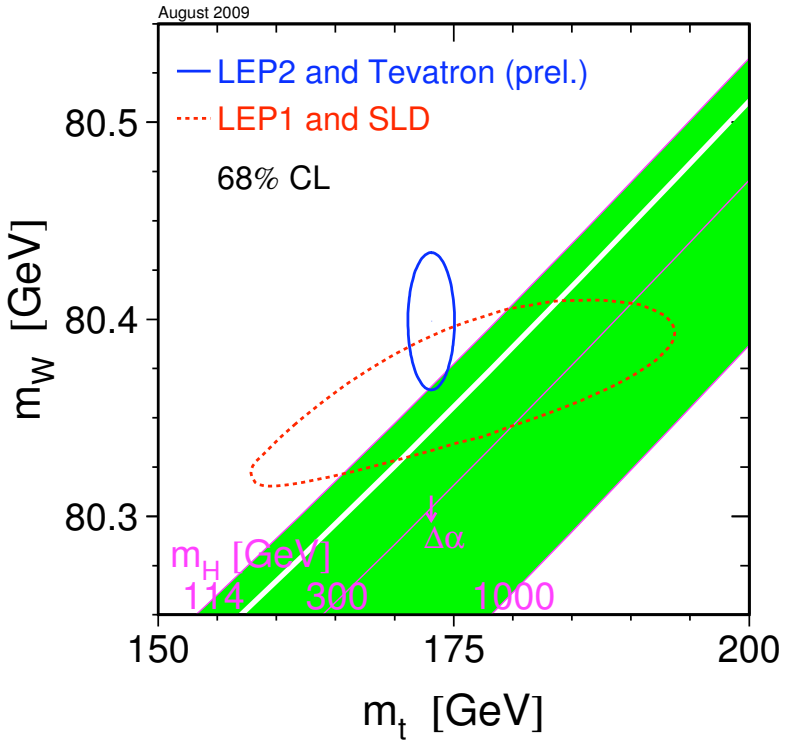

Figure 2.13: *The 68% confidence level contours on m_t and m_{W}. While the solid contour indicates the uncertainty from direct measurements the dotted contour indicate that from indirect measurements. The shaded diagonal region shows the prediction for various values of the Higgs mass based on the value for G_F.*

data favour a value of the Higgs Mass of $m_{\mathrm{H}} = 87^{+35}_{-26}\,GeV$ [19].

Experimental searches of the Higgs boson at LEP were based largely on the Higgs-strahlung process, see Figure 2.4. The lower limit from LEP which has already been indicated in Figure 2.13 is $m_h > 114.4\,\mathrm{GeV}$. This lower limit, given on the 95% confidence level, was obtained since the four LEP experiments have not observed a significant number of candidates even when applying tight selection cuts, see Figure 2.14. The most recent results on direct Higgs searches are obtained at the Tevatron. It has its highest sensitivity for the region $150 \lesssim m_{\mathrm{H}} \lesssim 180\,\mathrm{GeV}$. where the process $\mathrm{H} \rightarrow \mathrm{WW}$ is the dominant decay channel. The Figure 2.15 shows the exclusion limit at the 95% confidence level that the Higgs boson with a mass m_{H} is produced at a rate of $x \cdot \sigma_{\mathrm{SM}}$, where σ_{SM} is the prediction rate according to the Standard Model for a given Higgs boson mass. The Tevatron results exclude a Standard Model Higgs boson with a mass $163 < m_{\mathrm{H}} < 166\,\mathrm{GeV}$ [55].

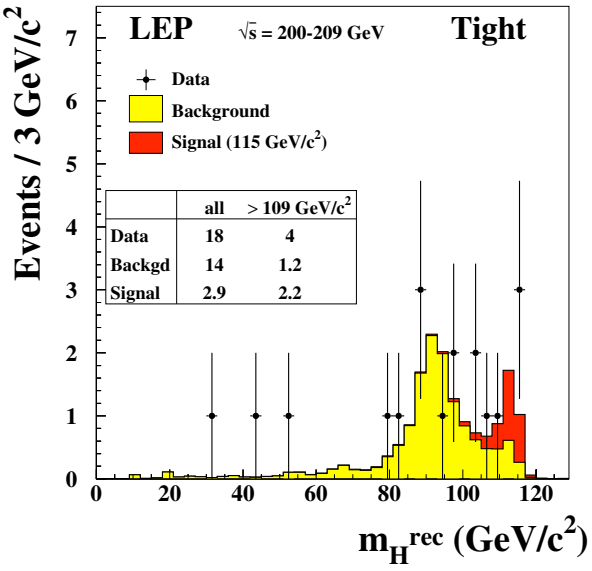

Figure 2.14: *Distribution of the reconstructed Higgs boson mass m_{H}^{rec} obtained in $\mathrm{e^+e^-}$ collisions at LEP for a tight selection scenario. The histogram shows in yellow (lightly shaded) the Monte Carlo prediction for the background and in red (heavily shaded) for an assumed Standard Model boson mass of 115 GeV. The points with error bars show the data.*

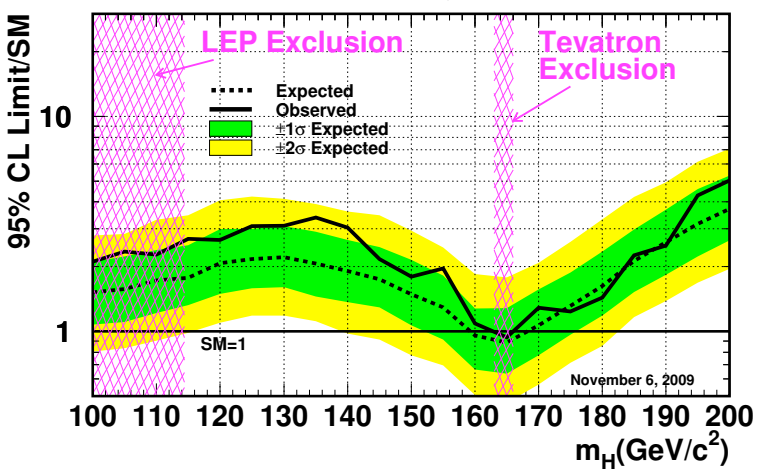

Figure 2.15: *Full Line: Observed upper limit on the cross section for Higgs production normalised to the Standard Model expectation. The dashed line show the same ratio for background to Higgs production. Between $163 < m_{\mathrm{H}} < 166\,\mathrm{GeV}$ the existence of a Higgs boson can be excluded at the 95% confidence level.*

Concluding Remarks

The arguments in this chapter have underlined that the Higgs boson is central to a broad program of discovery. Within the frame of the Standard Model or its minimal super-symmetric extension, it is very likely that there exists a Higgs boson with a mass not much above 100 GeV. One of the main goals of the LHC is to discover the Higgs boson. Detailed information on the true nature of the Higgs boson can however only be achieved by high precision measurements as possible at a e^+e^- collider. The next chapters will present the preparation of the construction of a linear e^+e^- collider, the ILC, which will operate at energies between the mass of the Z boson, i.e. approximately 90 GeV up to energies of approximately 1 TeV. This machine will thus play a key role in particular in answering questions concerning the existence and nature of the Higgs boson.

Chapter 3

A Silicon Tungsten Electromagnetic Calorimeter for a Linear Collider Detector

Contents

The next major worldwide project in high energy particle physics will be a linear electron positron collider at the TeV scale. This machine will complement and extend the scientific results of the LHC currently operated at CERN. The most advanced proposal for such a machine is the International Linear Collider (ILC). The experimentation at this machine could start around the year 2020. This chapter will introduce the concept of the ILC and briefly outline the CLIC, short for *C*ompact *LI*near *C*ollider concept which is another proposal for a linear electron-positron collider. After that the section will focus on the layout of the experiments to be operated at these machines. Therein mostly the status and prospects of the R&D for an electromagnetic silicon tungsten calorimeter will be highlighted. For background on term techniques concerning accelerator and detector physics as relevant for this chapter the reader is referred to the literature [56, 57, 58, 59].

3.1 The ILC Concept

The next electron positron machine is to be operated at a centre-of-mass energy of about 500 GeV or more. In circular accelerators or storage rings charged particles loose energy due to synchrotron radiation. The energy loss per turn of a particle with mass m and an energy E can be expressed as

$$\frac{\Delta E}{\text{Turn}} \sim \frac{\gamma^4}{r} \quad \text{with}\, \gamma = \frac{E}{m}. \tag{3.1}$$

Here r is the radius of the circular accelerator or storage ring. Thus a doubling of the beam energy would results in a 16-fold larger energy loss due to the synchrotron radiation. This loss can only insufficiently be compensated by enlarging the radius of the accelerator. In case of doubling the beam energy, the circumference of e.g. LEP would have had to become $16 \cdot 26.7 = 427.2\,\mathrm{km}$, which is clearly unrealistic. The huge increase in energy loss motivates to conceive the next generation electron positron collider as an entirely linear accelerator. As demonstrated in Chapter 1, a linear accelerator, SLC, was already very successfully operated at SLAC [17]. The energy losses by linear acceleration can be neglected even at the energies of several 100 GeV as envisaged for the linear collider discussed in this document. However, as can be already deferred from Figure 1.5, the processes which are to be studied have relatively small cross sections at several hundred GeV, provided there is no new resonance at this energy. The luminosity, the parameter for the collision frequency of the particles, has thus to be correspondingly high. At circular accelerators, this can be achieved by recycling the colliding bunches which would be obviously much more difficult to achieve in a linear accelerator. For a linear accelerator the luminosity $\mathcal{L}$ can be defined as [61]:

$$\mathcal{L} \sim \frac{\eta P_w}{\sqrt{s}} \times \left(\frac{\delta_E}{\varepsilon_{y,N}}\right)^{1/2} \times H_D \tag{3.2}$$

In this equation η is the transfer efficiency of the wall-plug power P_w. Further δ_E is the fractional beam loss due to synchrotron radiation and beam-strahlung caused by the space-charge field of the beams. H_D is the luminosity enhancement factor which appears as one colliding beam has a focusing effect on the other colliding beam. For the machines discussed in this document, this value is typically $H_D \approx 2$. Finally, $\varepsilon_{y,N}$ is the emittance of the beam which is an invariant of the beam particle motions and proportional to the product of vertical beam size and beam divergence.

The basic requirements for a linear electron positron collider are:

- According to the considerations in Chapters 1 and 2, the physics program requires centre-of-mass energies between 90 and 500 GeV upgradable to 1 TeV.
- A high instantaneous luminosity of about $2\times10^{34}\,\mathrm{cm}^{-2}\mathrm{s}^{-1}$. The operational efficiency should be high enough to provide an integrated luminosity of $500\,\mathrm{fb}^{-1}$ in four years.
- As outlined in Chapter 1, beam polarisation is essential for precision measurements of electroweak observables. Therefore, the electron and positron beams are required to be polarised. Beam energy and polarisation must be stable and measurable at a level of about 0.1%.

Following an international evaluation process, it turned out that a technology based on superconducting accelerating cavities is best suited to meet these goals [60]. This result is thus at the basis of the ILC concept. The ILC is designed to be operated with 9-cell niobium cavities cooled by super-fluid Helium to 2 K [61, 62]. An example of such a cavity is shown in Figure 3.1. In comparison with other concepts based on normalconducting cavities two major advantages can be highlighted.

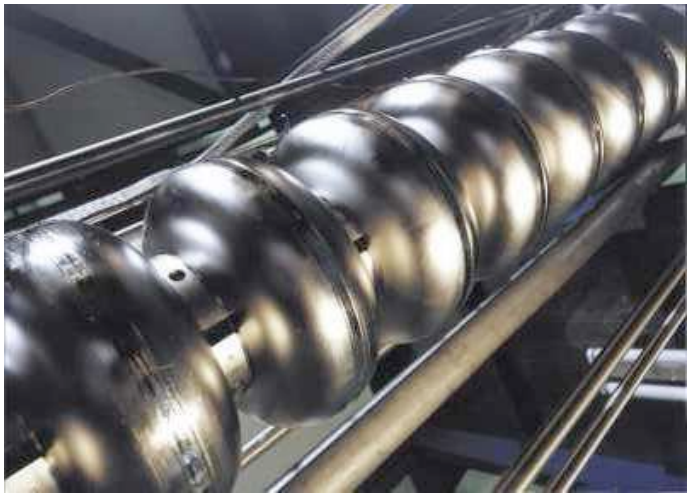

Figure 3.1: *Nine cell superconducting niobium cavities operated at a frequency of 1.3 GHz RF as envisaged for the accelerating structures of the International Linear Collider, ILC. The length of the cavity is approximately 1 m.*

- Due to the comparatively high quality factor of typically 10^{10}, the power transfer of the accelerating radio frequency wave to the beam is very high which allows for keeping the overall power consumption of the accelerator at a reasonable level. High beam power is the first essential requirement to obtain a high rate of electron proton collisions. As the ohmic losses and therefore thermal effects are very small the cavities can be driven over a relatively long time. This allows for the generation of long bunch trains with a large time separation between particle bunches. A bunch train will last about 1 ms and will contain around 3000 bunches separated by approximately 300 ns. This relatively large bunch separation permits to obtain a high performant feedback system to stabilise the beam. Naturally, the small losses lead to a high wall-plug to beam transfer efficiency. A key parameter for obtaining the necessary high energies is the energy gradient. The high quality factor is to a large extend achieved by a careful treatment of the surfaces of the accelerating cavities. As a result of this improvement, currently gradients of 31.5 MV/m seem to be achievable on industrial level.

- The operation frequency of superconducting cavities is limited by the surface resistance which increases with increasing frequency. Since the eigen frequency of a resonator is inversely proportional to its diameter, the cavities have to be comparatively large. However, the large size of the superconducting cavities has the advantage that wake field effects, that is a mutual influence of neighboured bunches due to their proper electromagnetic fields, are reduced. Wakefield effects occur when particles are displaced transversally from their nominal orbit. This reduced sensitivity of the accelerating structure with re-

spect to wake-field effects allow also for somewhat relaxed tolerances in the alignment of the cavities which in turn allows for an easier operation of the accelerator.

The Table 3.1 lists a few key parameters of the current proposal for the ILC for an operating energy of 500 GeV in comparison with previous accelerators introduced in Section 1.3. The Figure 3.2 shows a sketch of the current layout of the ILC accelerator complex. Here, the following elements are visible:

- A polarised electron source. Polarised electrons are obtained by shining polarised laser light on a gallium arsenide photo-cathode. This technique was already successfully employed at SLC where a polarisation of up to 80% was achieved [18].

- In the current layout, it is proposed that polarised positrons are created from the electron beam passing a helical undulator. The polarised photons created in the undulator field are converted into electron positron pairs which inherit the polarisation. The positrons are extracted and accelerated further. The proof-of-principle for producing polarised positrons with a helical undulator was demonstrated by the E166 Collaboration [64, 65]. For the studies to be presented in Chapter 4, a positron polarisation of 30% is assumed.

- Damping rings to cool the beam, i.e. to reduce its vertical divergence. A small vertical divergence is the first essential premise to achieve a small emittance. The cooling is happening at an energy of 5 GeV for the electrons and positrons.

- Two 11 km long beam-lines hosting the accelerating cavities. This part is called the main linac, short for Linear Accelerator.

- A 4.5 km long beam delivery system which brings the beams into collision at the interaction point under a 14 mrad crossing angle. The interaction point will be shared by two experiments. The final focusing magnet will be integrated into the experiments in order to provide the smallest possible beam size at the interaction point. A tiny beam size is the second essential premise for a small emittance.

The total footprint of the accelerator complex is 31 km in length. The table in Appendix A lists preliminary beam parameters for a few possible operation modes of the ILC. Some of these parameters will be referenced when discussing the accuracy of Higgs production measurements in Chapter 4. A comprehensive overview on the entire design of the ILC is given in [62]. Updates to this reference design can be followed under [63].

The Table 3.1 lists also parameters for the CLIC concept [67]. The latter is an R&D project for a multi-TeV collider and could become an option for a linear collider if discoveries at the LHC require a centre-of-mass energy considerably higher than 1 TeV. In short words, the main beam gets accelerated by extracting power from a parallel running second beam called the drive beam. This concept promises much

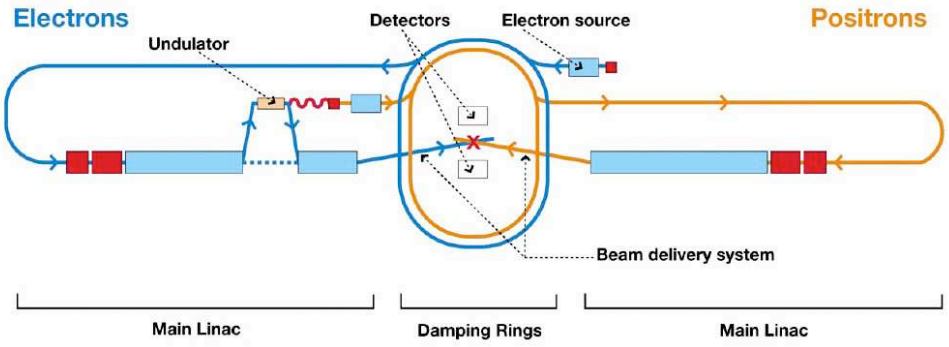

Figure 3.2: *Schematic layout of the ILC complex for 500 GeV centre-of-mass energy.*

larger gradients. On the other hand, since the cross sections at these high energies are even smaller than at around 1 TeV, this puts tight requirements to the beam size and to the collision frequency. In particular the short time separation between the particle bunches renders the feasibility of the experimentation at the CLIC collider currently questionable. For comparison with the ILC, the values in Table 3.1 gives the parameters for the operation mode at 500 GeV which is also envisaged for CLIC.

	LEPII	SLC	ILC @ 500 GeV	CLIC @ 500 GeV
Vertical size nm	40000	700	5.7	2.3
Total P MW	65	50	216	129
Wall plug transfer %	<1%	<1%	9.4	7.4
Luminosity $10^{31}\mathrm{cm}^2\mathrm{s}^{-}1$	5	0.2	>1500	1400
ΔT between bunches ns	∞	∞	300	0.5
Polarisation e^- %	No	80	>80%	>80%
Polarisation e^+ %	No	No	>30%	?
Gradient MV/m	8	17	31.5	100

Table 3.1: *A comparison of essential parameters of past and future electron positron colliders.*

3.2 Detector Requirements and the ILD Concept

The well known initial state of the electron positron collisions is an ideal premise for high precision measurements at the ILC. The extremely rich physics potential of the ILC puts high requirements on the detector performance. One driving force for the detector optimisation is an optimal separation of jet final states created W and Z bosons. As seen in Chapter 2 this would become particular important in the absence of the Higgs boson which would then require a new type of interaction in order to preserve unitarity. Other important measurements would be the couplings of the Higgs boson to fermions, in particular to quarks which turn into jets. On

average, after the decay of short-lived particles, about 62% of the jet energy is carried by charged particles, about 27% by photons, about 10% by neutral hadrons and 1.5% by neutrinos [68]. Traditionally high energetic jet final states are measured in calorimeters which provide an energy resolution of typically $50\%/\sqrt{E}$. On the other hand, Figure 3.3 illustrates that up to a given particle energy, the momentum measurement of charged particles by a tracking device is much more precise than the energy measurement by a calorimeter. Thus, the more the measurement of a final state can be based on the track momentum measurement of individual charged particles, the higher the precision which can be obtained. The concept to base the jet energy measurement on the measurement of individual particles is called *Particle Flow* and requires changes of paradigms in the detector design with respect to previous or existing detectors [69].

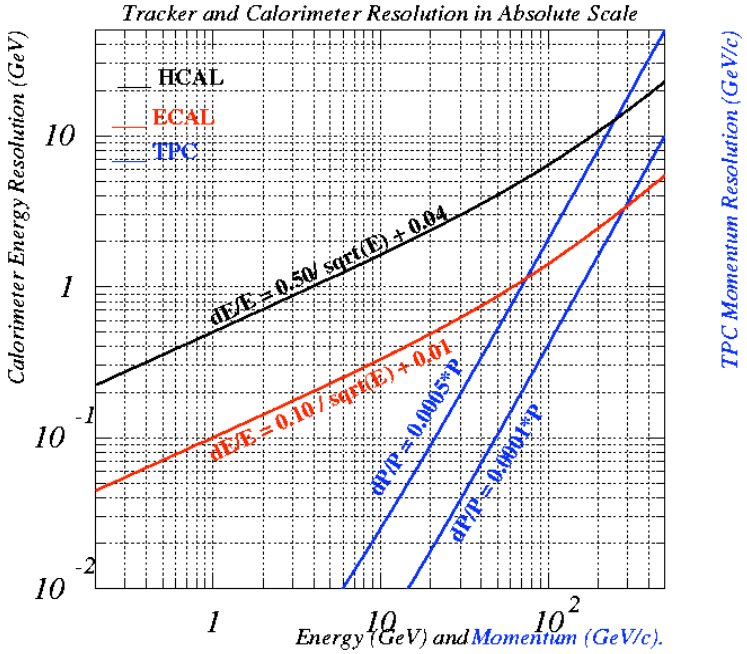

Figure 3.3: *Energy and momentum resolution as provided by tracking devices (TPC) and calorimetric devices (Ecal, Hcal). The study presented here was performed for the TESLA Detector proposal [61, 70] which was similar to the ILD Concept as described in this document.*

Individual particles can be separated by a large tracking volume in combination with a large magnetic field. By that, particles with opposite charge can be mutually separated from each other and from neutral particles of the final state. The latter can, however, only be measured in the calorimeter. The separation of charged and neutral particles can only be realised, if particles can also be traced in the calorimeters. This in turn requires a high granularity of the calorimeters. By means of highly granular calorimeters, showers created by charged particles can be associated with the corresponding tracks in the tracking device and can hence be discarded from

the calorimetric measurements. The jet energy resolution, a direct measurement for the detector performance, is then mostly given by residual overlap, called *confusion* hereafter, of near by particles in the final state. The concept of particle flow and the aim of resolving the jet energy E_{jet} to a value of $\sigma_{E_{jet}}/E_{jet} \approx 4\%$ impose the following design guidelines for a detector.

- A tracking system that ensures an optimal momentum measurement of charged particles complemented by a vertex system that provides an excellent reconstruction of secondary vertices from hadrons containing b and c quarks.
- Highly granular calorimeters to allow for the detailed tracing of particles inside the calorimetric volume. The calorimeters will have to be placed inside the coil providing the solenoidal field.
- All detector components interior to the calorimeters have to provide a small material budget. Otherwise the excellent performance of the individual components might get compromised by effects of multiple scattering or, in case of electrons or photons in the final state, by bremsstrahlung and pair production, respectively.
- The detector will have to be 4π hermetic in order to avoid uncertainties from final state particles scattered under very small angles.

The *I*nternational *L*inear Collider *D*etector concept, called *ILD* hereafter, has been proposed in a Letter of Intent [71] and got validated by an international panel of experts to be suitable to meet the requirements mentioned above [72]. The other validated concept is the SiD concept [73]. Both concepts are now invited to enter detailed technical studies for their realisation. A sketch of the ILD Detector is given in Figure 3.4. The z-axis of the right handed co-ordinate system is given by the direction of the incoming electron beam. Polar angles given in this document are defined with respect to this axis. From inner to outer, the ILD proposal features the following components.

- For the vertex detector two alternatives are proposed. One consists of three cylindrical double layers of silicon extending between 16 mm and 60 mm in radius and between 62.5 mm and 125 mm in z direction. For the second option the three double layers are replaced by five single layers which cover about the same volume. The vertex detector is designed for an impact parameter resolution of $\sigma_{r\phi} = \sigma_{rz} = 5 \oplus 10/(p \sin^{\frac{3}{2}}\theta)\,\mu$m.
- The measurement of charged tracks is supported by an inner Silicon Tracker (SIT) in the central region and by a set of silicon disks in forward direction (FTD), i.e. towards large absolute values of $\cos\theta$.
- The ILD detector contains a large Time Projection Chamber (TPC) with an inner sensitive radius of 395 mm and an outer sensitive radius of 1743 mm. The half length in z is 2250 mm. With this size, the track reconstruction can

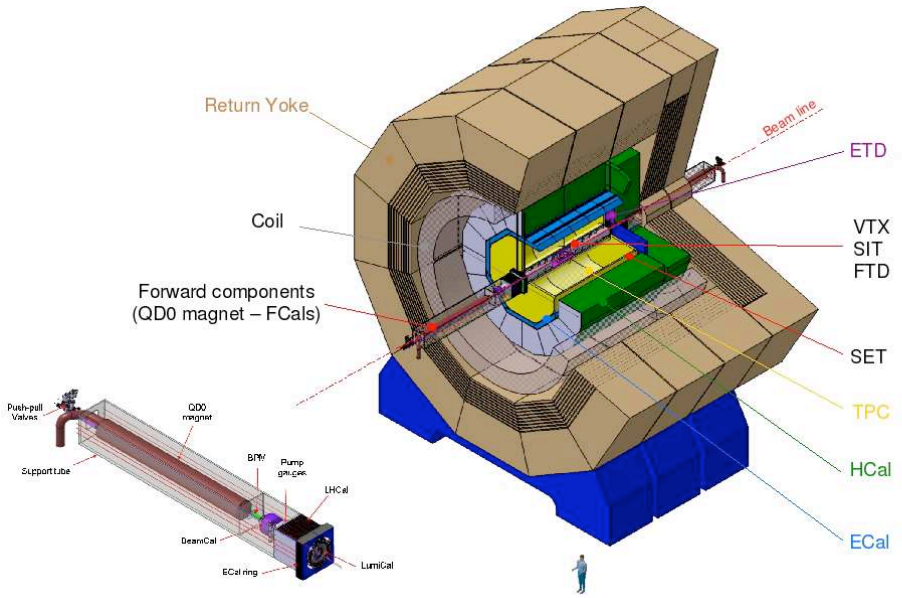

Figure 3.4: *Schematic view on the ILD Detector. The components are described in the text.*

be performed by means of about 200 individual tracker hits, recorded in pads at the extremities of the chamber. Recent simulation studies confirm that the momentum of charged particle tracks can be measured to a precision of $\delta(1/P_T) \sim 2 \times 10^{-5}\,\mathrm{GeV}^{-1}$. Here P_T denotes the transverse component of the three momentum P of the particles. It is envisaged to install another layer of silicon tracking devices which surrounds the TPC (SET, ETD). Tracks to which will be referred to in Chapter 4 are mainly based on TPC hits complemented with information from the SIT, FTD and the vertex detectors.

- The electromagnetic calorimeter is a SiW sampling calorimeter, called *SiW Ecal* hereafter. Its longitudinal depths of $24\,\mathrm{X}_0$ or equivalently 1 interaction length λ_I allows for the complete absorption of photons with energies of up to 50 GeV. The energy resolution of the electromagnetic calorimeter as evaluated from Monte Carlo simulations is $\frac{\Delta E}{E} = 15\%/\sqrt{E\,[\mathrm{GeV}]}$.

- The hadronic calorimeter surrounds the electromagnetic calorimeter and comprises 4.5 interaction lengths λ_I. Two proposals exist for the hadronic calorimeter: a digital variant consisting of steel absorbers and gas RPC chambers with a pixel size of $1 \times 1\,\mathrm{cm}^2$ as active material; a second variant featuring scintillating tiles with size of $3 \times 3\,\mathrm{cm}^2$ as active material. The latter has been retained for the current baseline of the ILD concept.

- In forward and backward direction the detector is completed by small angle calorimeters (FCALs) for measurements of luminosity and final state particles

scattered under very small angles. These calorimeters use diamond as sensitive material as these devices are the only ones for which radiation hardness is an issue. With these calorimeters a polar angle coverage of the ILD detector down to 5 mrad is assured.

- A large volume superconducting coil surrounds the calorimeters, creating an axial B-Field of nominally 3.5 T.

Prior to the Letter of Intent, the ILD concept went through a dedicated optimisation study. The study was performed by applying the Pandora Particle Flow Algorithm [68]. Among other items, this optimisation procedure addressed the choice of the magnetic field B, the inner radius of the SiW Ecal R as well as the cell size of that device. The criterion was the jet energy resolution $\sigma_{E_{jet}}/E_{jet}$. The result of the study are:

- The inner radius of the Ecal and the magnetic field were varied independently. As demonstrated by Figure 3.5, the dependency of the jet energy resolution, expressed as rms_{90}, on the inner radius of the SiW Ecal is much stronger that the dependency on the magnetic field. The jet energy resolution can be approximated by the empirical function

$$\frac{\sigma_{E_{jet}}}{E_{jet}} = \frac{21}{\sqrt{E/\mathrm{GeV}}} \oplus 0.7 \oplus 0.004E \oplus 2.1 \left(\frac{R}{1825\,\mathrm{mm}}\right)^{-1.0} \left(\frac{B}{3.5\,\mathrm{T}}\right)^{-0.3} \left(\frac{E}{100\,\mathrm{GeV}}\right)^{0.3} \%.$$

  The quadratic sum is composed of four terms: i) the estimated contribution to the jet energy resolution from the intrinsic calorimeter resolution; ii) the contribution from imperfect track reconstruction; iii) Leakage out of the hadronic calorimeter; iv) contribution of confusion. Apart from the stronger dependence on the inner Ecal radius R, the function demonstrates also that the particle separation gets more difficult with increasing jet energy. This is expected since jets get more collimated when their energy increase.

- As shown in Figure 3.6, the energy resolution improves significantly with smaller cell dimensions of the SiW Ecal. The higher granularity supports the correct assignment of calorimeter clusters to the tracks and becomes most important towards high jet energies. The Ecal allows for a correct separation of photons and charged hadrons [74] and a precise determination of the starting point of hadronic showers. Note, that about 60% of the hadrons start to shower in the SiW Ecal volume.

The last item listed in the optimisation study motivates the construction of a highly granular electromagnetic calorimeter. In the following section, the status and prospects of the R&D towards its realisation will be described.

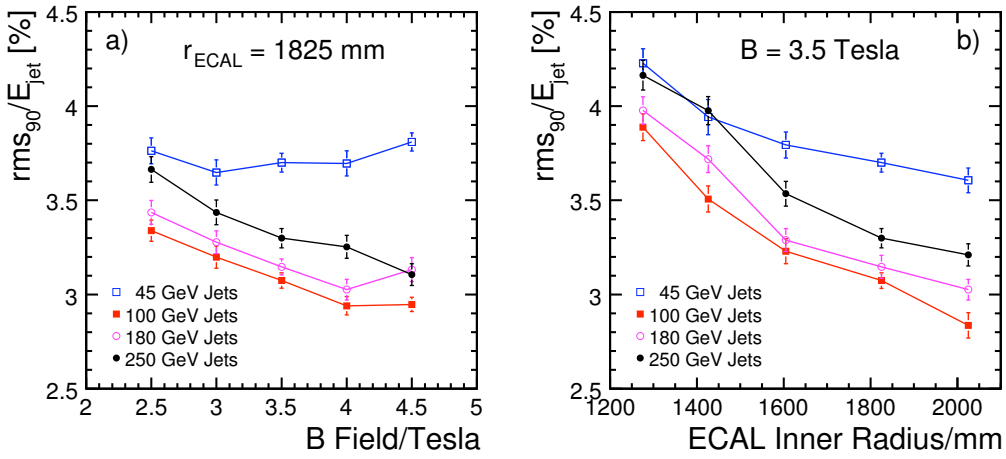

Figure 3.5: *a) the dependence of the jet energy resolution* (rms_{90}) *on the magnetic field for a fixed ECAL inner radius. b) the dependence of the jet energy resolution* (rms_{90}) *on the Ecal inner radius a fixed value of the magnetic field.*

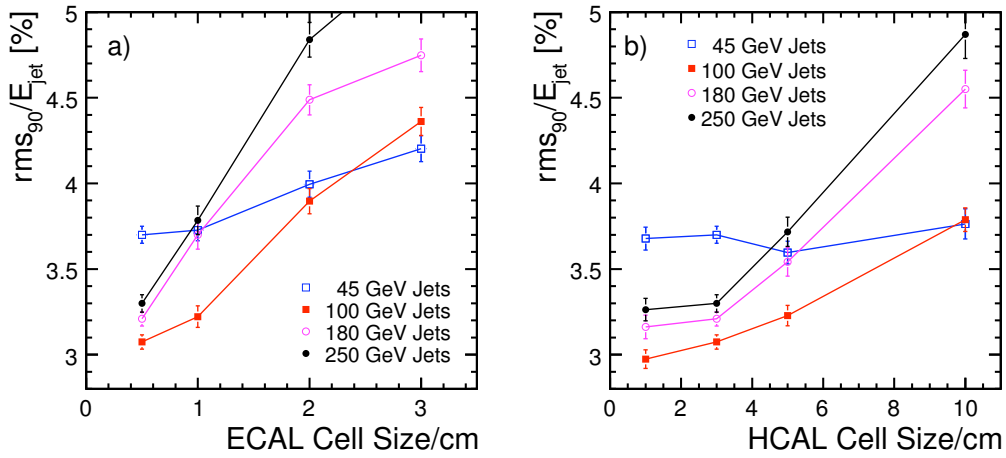

Figure 3.6: *a) the dependence of the jet energy resolution* (rms_{90}) *on the Ecal transverse segmentation (Silicon pixel size). b) the dependence of the jet energy resolution* (rms_{90}) *on the HCAL transverse segmentation (scintillator tile size).*

3.3 R&D for the Silicon Tungsten Electromagnetic Calorimeter

The reconstruction of the final state of the e^+e^- interactions will be based on particle flow algorithms (PFA). The goal is to reconstruct every single particle of the final state which in turn demands a perfect association of the signals in the tracking

systems with those in the calorimeters. As a consequence, this requires a perfect tracking of the particle trajectories even in the calorimeters. To meet these requirements the detectors have to cover the whole solid angle and have to feature an unprecedented high granularity. For an optimal particle flow, the calorimeters will have to be placed inside the magnetic coil of the detector which puts tight constraints on the space available for the installation of the detectors. The design of the calorimeters have thus to follow two main guidelines

- The number of readout channels has to be driven to an unprecedented amount.
- The calorimeters have to be extremely compact and hermetic. This concerns both, the choice of the absorber material and the integration of infrastructural components such as cooling, power supply, readout lines and front end electronics.

For the electromagnetic calorimeter which surrounds the tracking system the two guidelines above lead to the choice of Tungsten as absorber material having a Radiation length $X_0 = 3.5\,\mathrm{mm}$, Molière Radius $R_M = 9\,\mathrm{mm}$ and Interaction length $\lambda_I = 96\,\mathrm{mm}$ and Silicon as the active material. The Figure 3.7 shows the position of the SiW Ecal in the ILD detector, the trapezoidal form of the modules and how it is envisaged to be interfaced mechanically with the hadron calorimeter.

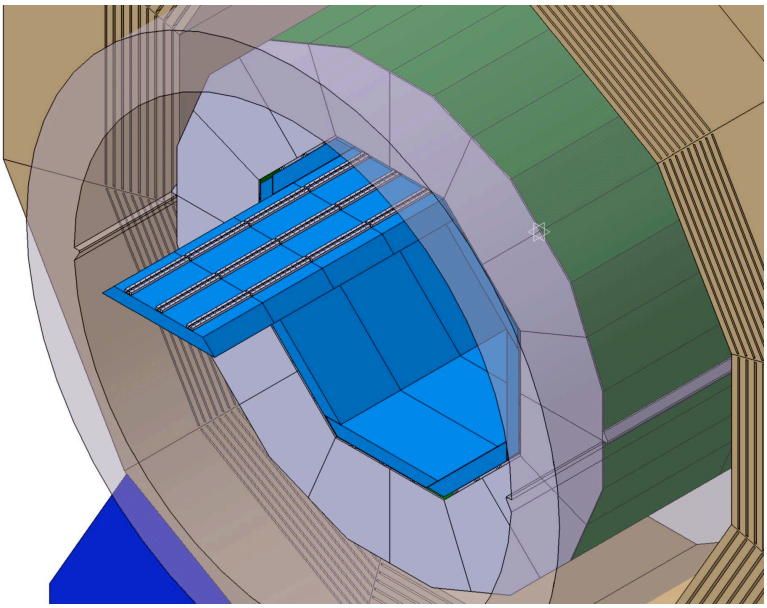

Figure 3.7: *The SiW Ecal (in blue) within the ILD Detector.*

The CALICE collaboration [75], short for *CA*lorimeter for a *LI*near *C*ollider *E*xperiment, conducts a large R&D program for the development of highly granular calorimeters as envisaged for the detectors of the ILC. It comprises 386 physicists and engineers from 17 countries and 4 continents. A physics prototype of the SiW Ecal dedicated mainly to demonstrate the physics potential of a calorimeter fulfilling

the requirements above but also to validate the main mechanical concepts has been constructed and is currently examined in beam test measurements at DESY, CERN and FNAL. The results of the beam test data taking with the physics prototype as well as the steps towards the realisation of its successor, a technological prototype, will be described in the following sections.

3.3.1 Results with the Physics Prototype

The physics prototype [76] is dedicated to demonstrate the principle of compact high granular calorimeters. Its major purpose is to verify physics observables like energy resolution and angular resolution to support the validity of the ongoing physics studies with a full detector. Another important objective of the program with the physics prototype is the verification of models of hadronic showers. These are typically less well modelled than electromagnetic showers and the uncertainty can be estimated from the fact that the simulation toolkit GEANT4 [77] offers more than 10 different models for these hadronic showers. The Figure 3.8 shows a lateral view of the physics prototype. It consists of 9720 1x1 cm^2 wide calorimeter cells in 30 layers. The active zone covers 18x18 cm^2 in width and approximately 20 cm in depth. The layers are composed alternately by W absorber plates and a matrix of PIN diode sensors on Silicon Wafer basis. At normal incidence, the prototype has a total depth of 24 X_0 achieved using 10 layers of 0.4 X_0 tungsten absorber plates, followed by 10 layers of 0.8 X_0, and another 10 layers of another 1.2 X_0 thick plates. The sensitive layers are mounted onto both sides of a H-shaped tungsten plate as shown in Figure 3.9. Such an entity is called a slab. The readout electronics sticks out to the left of the sensitive area. In the following, the main characteristics of the mechanical structure, the silicon sensors and the Front End Electronics will be outlined

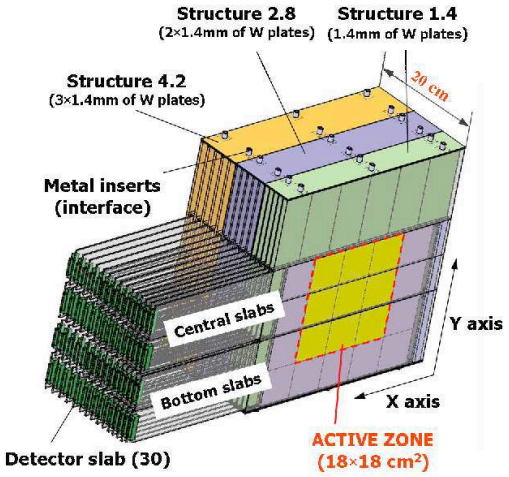

Figure 3.8: *Schematic 3D view of the Physics Prototype. Figure taken from [76].*

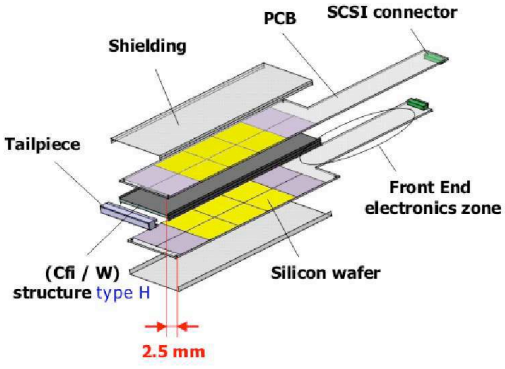

Figure 3.9: *Schematic diagram showing the components of a detector slab. Figure taken from [76].*

- The mechanical structure of the physics prototype features an innovative effort to reduce the zones with passive material, to ensure compactness and to provide a self-supporting structure of the detector which in turn will minimise additional mechanical support in a detector operated at the ILC. All the three requirements can be fulfilled by integrating half of the W absorber layers into the detector housing. More precisely, the sheets of tungsten plates are placed onto metal cores wrapped into pre-impregnated carbon fibre and epoxy glue. By a curing process at about 135^{o}C in an autoclave, the carbon fibre, the epoxy components and the tungsten plates are glued into a stiff structure. After the curing, the metal cores are drawn out, leaving free spaces within the structure, the alveoli, in which the slabs mentioned above are inserted. In order to avoid channelling effects during data taking, the layers within a slab are shifted by 2.5 mm with respect to each other. In addition to that, two slabs are shifted by 1.3 mm with respect to each other. The details of layer offsets and residual passive areas are given in Figure 3.10. For studies at non-zero impact angles of the beam, the detector is placed on a rotational support. In order to provide a maximal sensitive volume in rotated position, the individual structures can be shifted with respect to each other into 5 different positions, corresponding to impact angles pf 0^o, 10^o, 20^o, 30^o and 45^o. An example for a rotated configuration for an angle of 45^o is sketched in Figure 3.10.

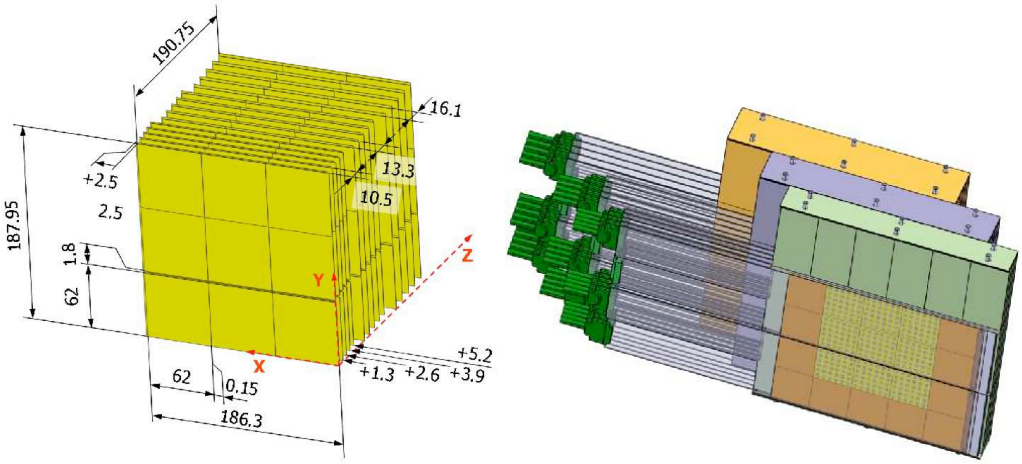

Figure 3.10: *Left: Details of layer offsets and passive areas. Right: Schematic 3D view of the SiW Ecal in rotated position for an angle of* 45^o.

- The PIN diodes are made from 4x4 inch^2 wide and 525 μm thick silicon wafers with a resistivity of 5M$\Omega \cdot$ m. The sensor matrix and its dimensions are shown in Figure 3.11. A minimal ionising particle (MIP) creates 42000 electron-hole pairs when passing the Silicon Wafer transversely. The aim of this choice is to provide a signal over noise ratio of 10 at the end of the entire readout chain of the detector. Although PIN diodes are rather simple and widely used

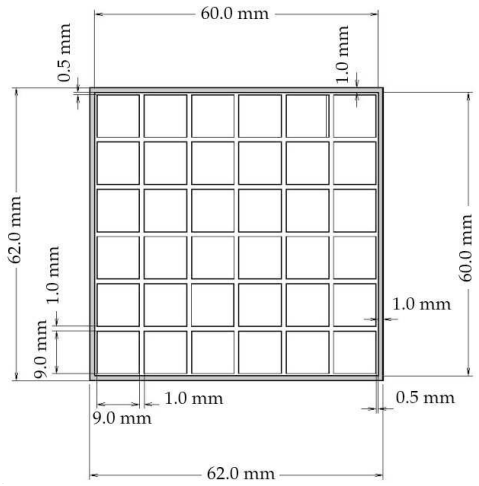

Figure 3.11: *Details of the matrix dimensions in a module (cathode side). The area shaded in grey corresponds to the guard ring.*

in detectors, the challenge here is to well control the cost of the fabrication process. It has to be kept in mind that in the final electromagnetic calorimeter, e.g. for ILD, about 3000 m^2 will have to be covered with silicon sensors. The matrix is enclosed by an approximately 1 mm wide *continuous* guard ring. In semi-conductor applications, guard rings serve to stabilise the depletion region over the *pn* junction in a diode which may be reduced by charges accumulated on the passivation layer. At the same time, guard rings serve to drain leakage currents due to crystal defects away from the sensitive area.

- The main device of the Very Front End, *VFE*, electronics is a 18 channel charge sensitive front end Application Specific Integrated Circuit (ASIC), called FLC_PHY3. One 6×6 sensor matrix is thus readout by two ASICs which provides also a redundancy by decorrelating ASIC and sensor response. As shown in Figure 3.12, the signal paths starts with a variable gain charge preamplifier followed by two shaping filters for gains 1 and 10 with a shaping time of 180 ns for both gains. The shaped signal is then propagated to a sample and hold device realised by a 2 pF capacitance after which the measured voltage which is proportional to the charge at the input of the pre-amplifier is written into a buffer designed to store the 18 signals as processed by the signal chain.The eighteen signals are read one-by-one by the off-detector electronics. One channel provides a dynamic range of about 500 MIP which has been considered to be sufficient for a beam test data taking with primary electrons of an energy of up to 50 GeV.

- The interface between the sensor matrices and the VFE ASICs is provided by multilayer VFE boards of which two types do exist. One type for the *central slabs* is equipped with 6, i.e. 3×2, sensor matrices, see Figure 3.13, while the other for the *bottom slabs* is equipped with 3, i.e. 3×1, sensor matrices.

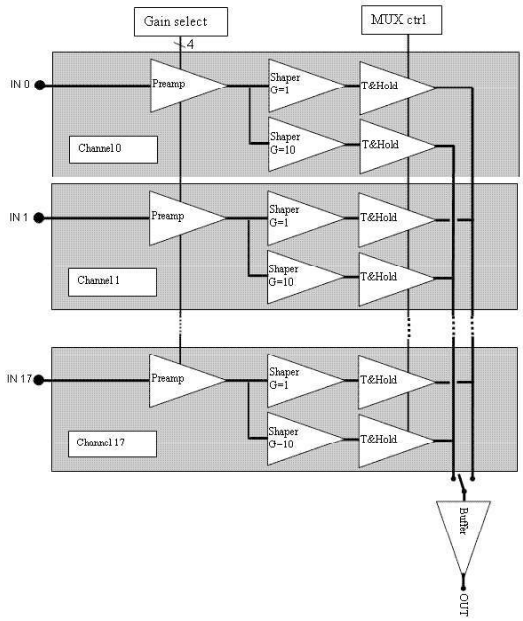

Figure 3.12: *General block schematic of FLC_PHY3.*

The 216 cells of the central boards are read out by 12 VFE ASICs while the 108 cells of the bottom boards are readout by 6 VFE ASICs. The data are acquired by the off-detector electronics in a 12x18 multiplexing series.

Beam test data taking

The physics prototype was subject to large scale beam test data taking in the years 2006-2008. Data have been taken at DESY, CERN and FNAL. In these beam test campaigns about 10^8 events have been recorded with electron, pion and muon beams. This considerable amount of data required already a structured data processing approach which is described in Appendix B. A picture of the beam test setup at FNAL is shown in Figure 3.14.

The beam test data taking was conducted in conjunction with a high granular analogue hadron calorimeter, called *AHcal* hereafter, with iron as absorber and scintillating tiles readout by silicon photo-multipliers. Finally the calorimetric devices have been completed by a *Tail Catcher and Muon Tracker*, also called *TCMT*, using a technology similar to the AHcal. The beam line is completed by a set of drift chambers, for position resolution measurements and a set of scintillator triggers. At CERN and FNAL a Cerenkov Counter for particle identification was also part of the beam line instrumentation. The Figures 3.15 and 3.16 show the response of the prototype to electrons in terms of linearity and energy resolution [78].

The results are based on an analysis of data taken in the year 2006 at CERN. For the analysis, events have been selected which have their impact well away from the wafer boundaries. Both observables are well described by a GEANT4 Monte

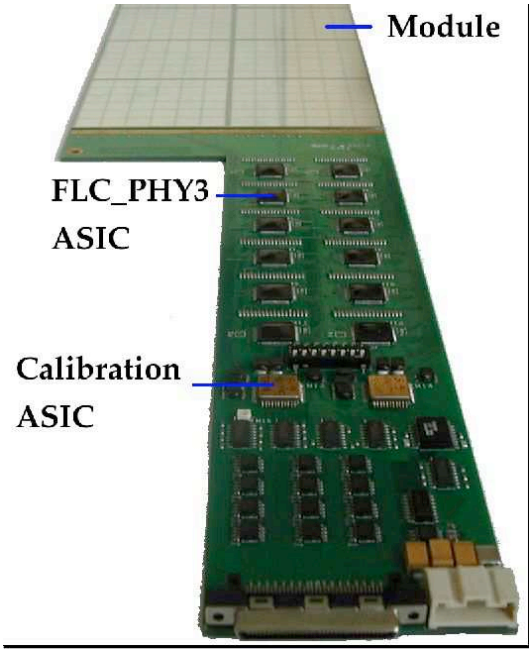

Figure 3.13: *Picture of the very front end PCB, and description of its elements. PCB thickness: 2.1 mm, length: 600 mm, largest width: 12.4 mm.*

Figure 3.14: *CALICE beam test setup in the MTBF area at Fermilab. The SiW Ecal physics prototype is visible in the front, followed by an analogue Hcal and a Tail Catcher and Muon Tracker.*

Carlo Simulation of the beam test setup. It is found that between 6 and 45 GeV the detector response is linear within 1%. The energy resolution is determined to be

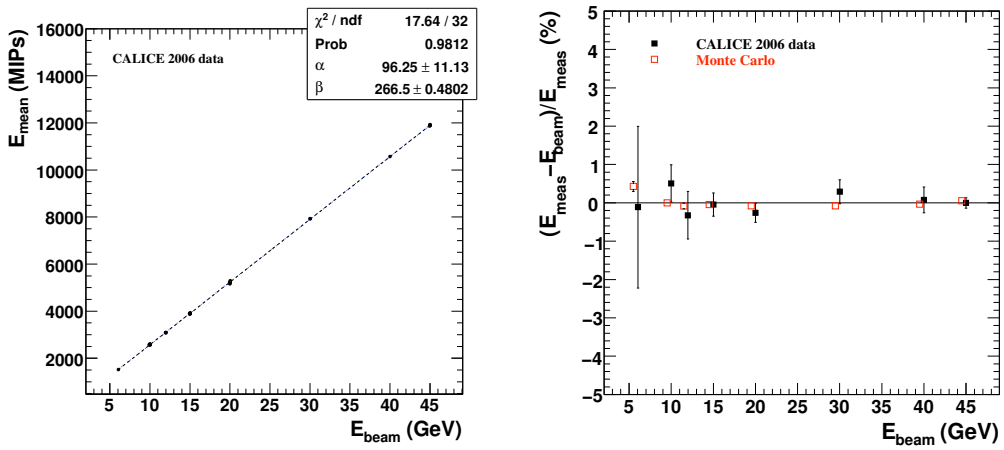

Figure 3.15: *Left: Linearity of the energy response of the SiW Ecal as a function of the nominal energy. Right: The residuals between the measured and the nominal energy.*

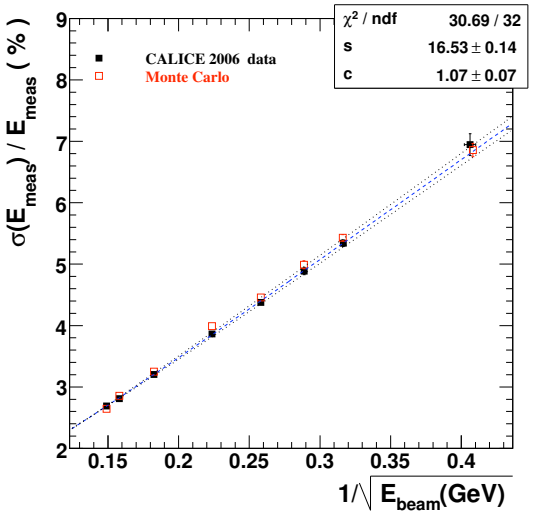

Figure 3.16: *Relative energy resolution ($\sigma(E_{\text{meas}})/E_{\text{meas}}$) as a function of $1/\sqrt{E_{\text{beam}}}$ (solid squares), and its usual parametrisation as $s/\sqrt{E} \oplus c$. For clarity, the 35 runs available were combined into 8 different beam energy points for the plot. For the parametrisation of the energy resolution each run was however treated individually. The values expected from simulation are shown (open squares). The dashed line gives the fitted resolution for data (Equation 3.3), and the dotted lines correspond to its variation when the beam energy scale is shifted by ± 300 MeV.*

$$\frac{\sigma(E_{\text{meas}})}{E_{\text{meas}}} = \left(\frac{16.53 \pm 0.14(\text{stat}) \pm 0.4(\text{syst})}{\sqrt{E(\text{GeV})}} \oplus (1.07 \pm 0.07(\text{stat}) \pm 0.1(\text{syst})) \right) \%, \tag{3.3}$$

This is compatible with the value assumed for the full detector simulation of the ILD detector as indicated above. For the data taken in 2006 at CERN also the angular resolution has been determined. Here a set of drift chambers located upstream of the SiW Ecal are used to provide reference values. The angles are defined from the eigenvectors $\hat{x}$, $\hat{y}$, $\hat{z}$ of the cluster of a primary particle which is in first approximation an ellipse. By these eigenvectors, the angles ϕ and θ are defined as:

$$\phi = \text{atan}(\hat{y}/\hat{z}), \quad \theta = \text{atan}(\hat{x}/\hat{z}). \tag{3.4}$$

The results are displayed in Figure 3.17. The angular distribution is found to be [80]:

$$(106 \pm 2)/\sqrt{E} \oplus (4 \pm 1)\,\text{mrad along the x-direction and}$$
$$(100 \pm 2)/\sqrt{E} \oplus (14 \pm 1)\,\text{mrad along the y-direction.}$$

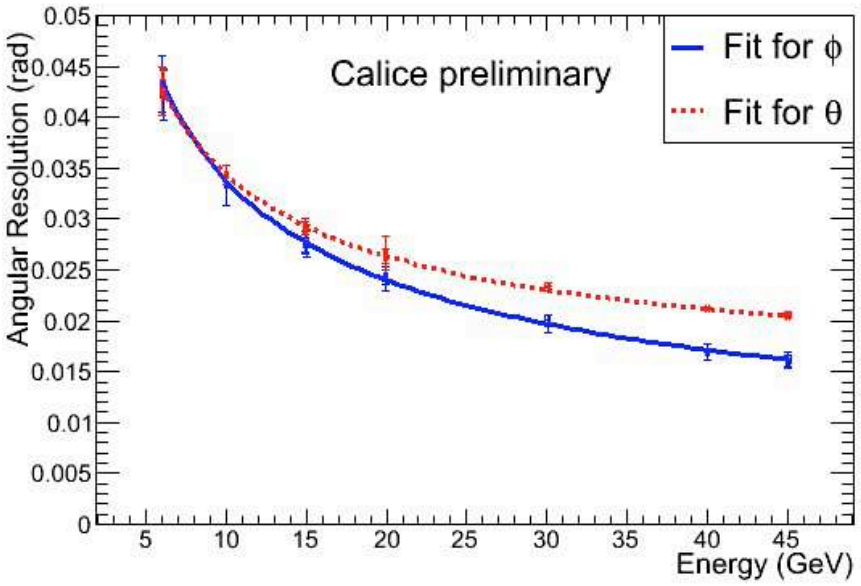

Figure 3.17: *Angular resolution of the SiW Ecal as a function of the energy of the incident beam. The results are given separately for the angles ϕ measured with respect to the x-direction and, θ, measured with respect to the y-direction.*

The differences between the two directions can be explained by the different arrangement of the detector layers in x and y direction.

3.3.1.1 Calibration of the SiW Ecal for the 2008 FNAL Data

This section summarises the main results of the calibration of the data taken in 2008 at the Meson Test Facility at FNAL [79]. The details of the calibration procedure

are presented in [76]. The relative calibration was performed using dedicated muon beams with an energy of 32 GeV. At this energy, muons are expected to loose their energy only by ionisation and act, to a good approximation, as minimal ionising particles (MIP).

In a first step the pedestal and pedestal dispersion of the 9720 Ecal cells were extracted. The results are shown in Figure 3.18 and 3.19.

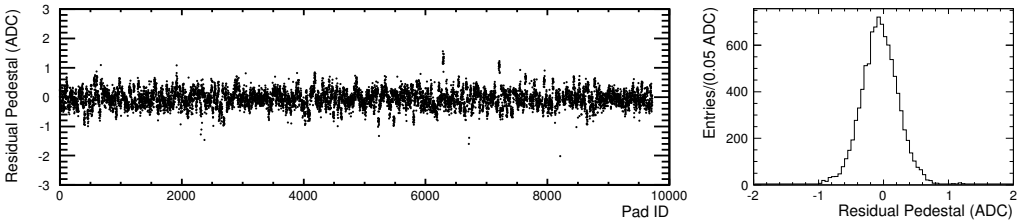

Figure 3.18: *Left: Residual pedestal as a function of the pad index for the muon calibration data. Right: After projection onto the y axis the resulting mean is* -0.058 ± 0.003 *ADC counts with a RMS of* 0.281 ± 0.002 *ADC counts.*

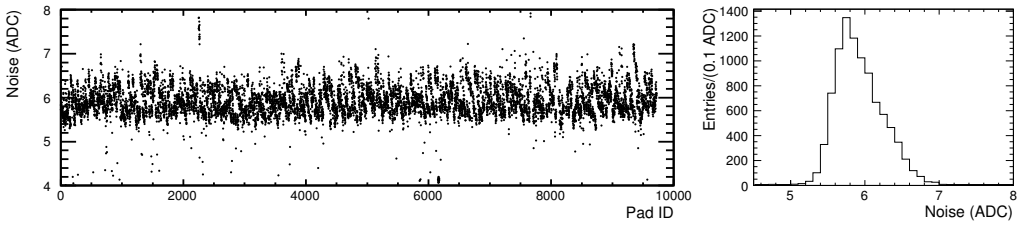

Figure 3.19: *Left: Pedestal dispersion as a function of the pad index for the muon calibration data. Right: After projection onto the y axis the resulting mean is* 5.930 ± 0.003 *ADC counts with a RMS of* 0.330 ± 0.002 *ADC counts.*

The average pedestal has a mean of -0.058 ± 0.003 ADC Counts with a rms of 0.281 ± 0.002 ADC Counts. Hence, the resulting pedestals are well compatible with zero as expected. The average width of the pedestal distributions and hence the average noise of the calorimeter cells are found to be 5.930 ± 0.003 ADCCounts with an rms of 0.330 ± 0.002 ADC Counts. For the calibration, muons incident on the Ecal surface were selected. It was required, that the series of cells hit by the muon can be well fitted by a straight line. A typical MIP spectrum in a cell is shown in Figure 3.20.

As expected, the signal shape follows a Landau distribution which is superimposed by a Gaussian noise component. The calibration constant is given by the most probable value of the Landau distribution for a fit in the range between 25 and 78.5 ADC Counts. The resulting calibration constants for all cells are shown in Figure 3.21. The mean of the calibration constants is found to be 47.61 ± 0.02 ADC Counts. The systematic error of 0.77% of this value is estimated by extending the fitting range to all measured ADC counts for a given cell. The

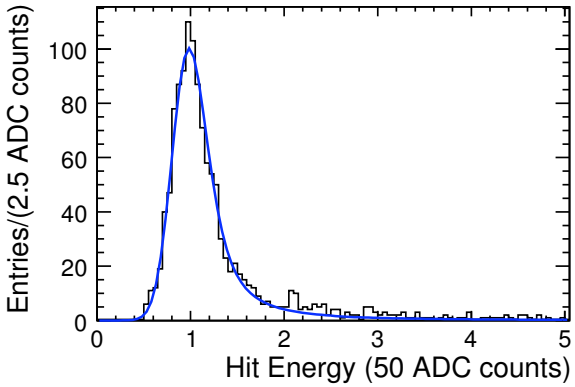

Figure 3.20: *A typical MIP spectrum found for a calorimeter cell for muons used for calibration. The spectrum can be well fitted by a convolution of a Landau with a Gaussian distribution. The resulting calibration constant for this particular cell is* 46.57 ± 0.04 *ADC Counts as given by the Landau MPV, while the noise is* 7.26 ± 0.73 *ADC Counts given by the Gaussian sigma.*

mean of the calibration constants has to be compared to the rms of the noise of measured above of 5.930 ± 0.003 ADC Counts. By these values the signal over noise ratio is given to be 7.95 for the detector under beam test conditions.

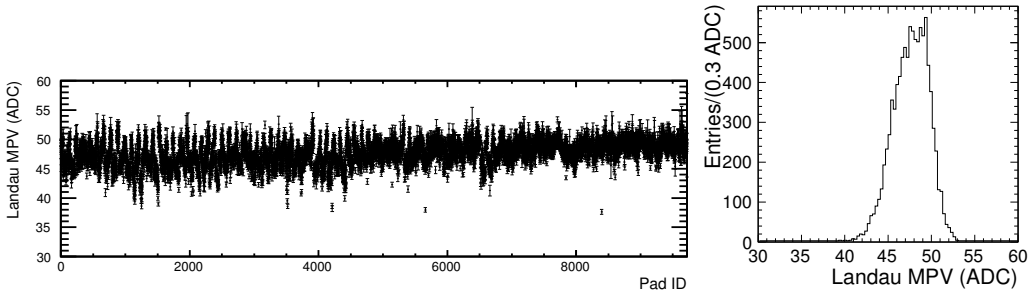

Figure 3.21: *Left: Calibration Constants as a function of the cell index. The systematic error assigned to each constant is estimated by a variation of the fit range. Right: After projection onto the y axis the resulting mean is* 47.61 ± 0.02 *ADC Counts with a RMS of* 2.06 ± 0.01 *ADC Counts.*

With respect to the operation in a detector at the ILC, the stability of the calibration is an important issue. The total electromagnetic calorimeter will comprise of the order of 10^8 cells. It is clear that calibrating this large number of cells in situ, using cosmic muons, beam halo muons or even stubs in hadronic showers, will be extremely challenging. The detector modules will have to be calibrated in a beam test prior to installation. The question is how well a calibration found in a beam test is applicable to the operation in the detector. A good indicator to answer this question is the comparison of calibration constants obtained in different beam test

periods. Figure 3.22 shows the correlation between the calibration constants as obtained for the 2008 FNAL and two sets of calibration constants obtained during the 2006 data taking at CERN, labelled "Aug.06" and "Oct.06", respectively.

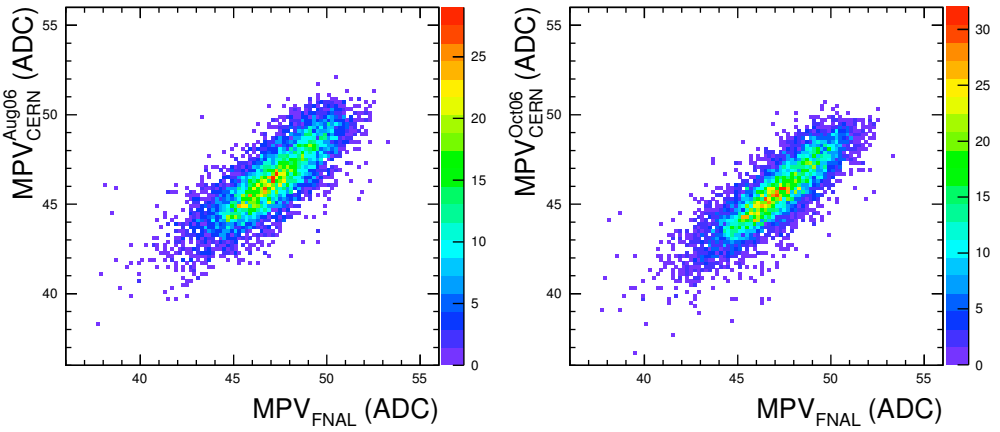

Figure 3.22: *Correlation of calibration constants obtained for muon calibration in August (left) and October (right) 2006 at CERN with those obtained for muon calibration runs in 2008 at FNAL. A correlation coefficient of* $(80.30 \pm 0.44)\%$ *is found when comparing with the ones obtained for August 2006 at CERN, while* $(83.76 \pm 0.37)\%$ *is found when comparing with ones obtained for October 2006 at CERN.*

The correlation between these calibration constants is $(80.30 \pm 0.44)\%$ and $(83.76 \pm 0.37)\%$. The difference is displayed in Figure 3.23 for the comparison with the August 06 data and in Figure 3.24 for the comparison with the October 06 data. The average difference is 1.21 ± 0.01 ADC Counts and 0.67 ± 0.01 ADC Counts, respectively.

This residual difference can be traced back to different timing offsets between trigger arrival and signal arrival in the various data taking periods.

In conclusion, the comparison of the different sets of calibration constants provides evidence that the calibration can also be well controlled for a full SiW Ecal in a detector at the ILC and constitutes thus an important result in view of the feasibility of its realisation.

3.3.1.2 Hadronic Showers in the Ecal

Given the depth of about one interaction length, it can be assumed that about 60% of the hadrons contained in a jet will interact in the volume of the SiW Ecal. It is therefore important to understand the interactions of hadrons in the SiW Ecal. A study of the hadronic interactions in the Ecal serves two purposes:

- The high granularity allows for a detailed investigation of the substructure of hadronic showers. Once understood, the data will constitute one of the most

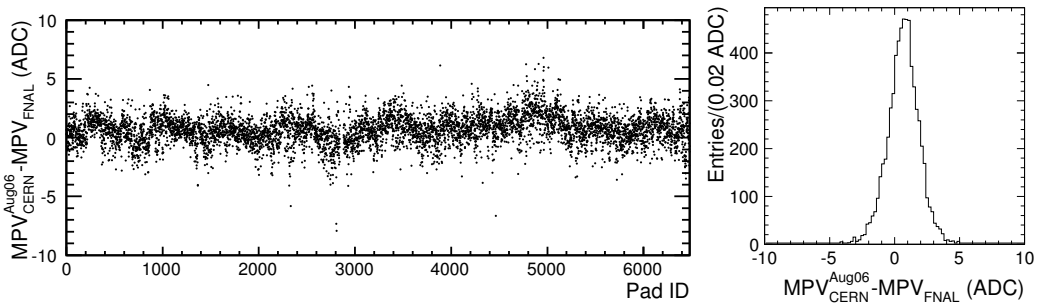

Figure 3.23: *Left: Difference of the calibration constants between August 2006 CERN runs and 2008 FNAL runs as a function of pad index. Right: Distribution of the difference of each pad, with a mean of* 0.67 ± 0.02 *ADC Counts and a RMS of* 1.21 ± 0.01 *ADC Counts.*

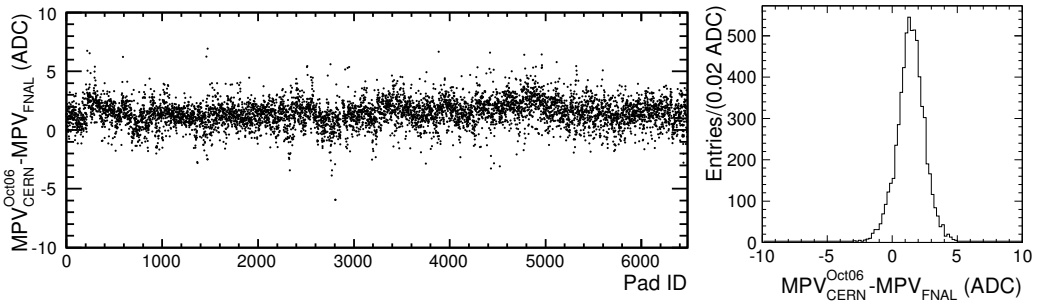

Figure 3.24: *Left: Difference of the calibration constants between October 2006 CERN runs and 2008 FNAL runs as a function of pad index. Right: Distribution of the difference of each pad, with a mean of* 1.42 ± 0.01 *ADC Counts and a RMS of* 1.08 ± 0.01 *ADC Counts.*

detailed measurements of hadronic showers ever. This is at least true for the initial phase of a shower and for low energetic hadrons.

- Understanding the development of hadronic showers is a first step to improve existing or to develop new particle flow algorithms. A deep understanding of the shower development may allow for the correct assignment of energy depositions to a shower and thus to reduce the confusion term.

In a first step the interaction region of a pion entering the SiW Ecal has been identified. This is achieved by analysing the energy deposition in consecutive layers of the SiW Ecal. As a first result, four types of interactions can be distinguished, see Figure 3.25.

- A MIP like interaction. Here the particle traverses the detector without any notable interaction.

- A fireball like interaction. Here a particle deposits the energy equivalent to at least 5 MIP in three consecutive layers.

- A point like interaction. This interaction is characterised by one isolated layer with a large energy deposition. After this interaction the particle either continuous to act as a MIP or splits up into two tracks of mips, giving rise to a fork like interaction.

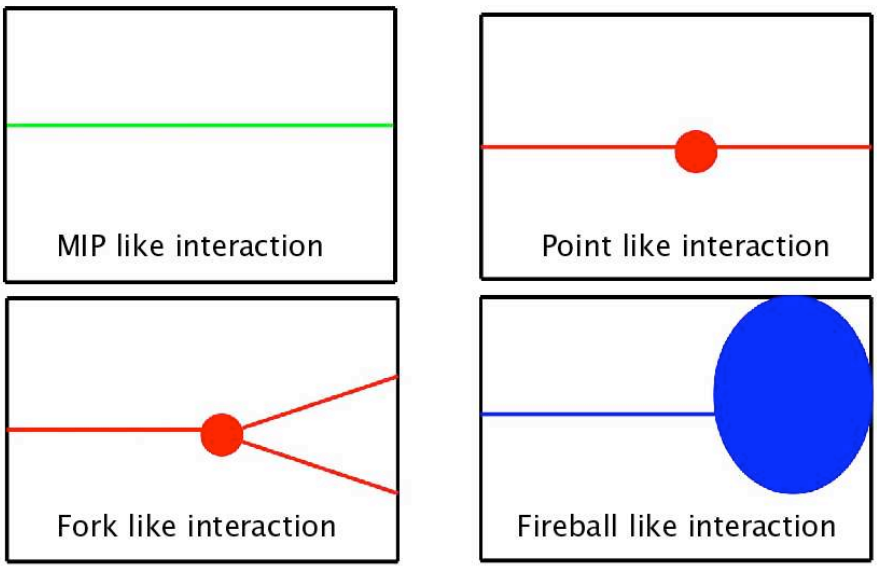

Figure 3.25: *Different types of hadronic interactions which can be distinguished with the SiW Ecal.*

Figure 3.26 shows the longitudinal and lateral shower width as simulated in the SiW Ecal. The longitudinal width is defined as:

$$\sigma^2_{long} = \frac{\sum_{hits} E_i \cdot z_i^2}{E_{tot}} - \left(\frac{\sum_{hits} E_i \cdot z_i}{E_{tot}} \right)^2 \tag{3.5}$$

while the lateral shower width is defined as:

$$\sigma^2_{trans} = \frac{\sum_{hits} E_i \cdot (x_i^2 + y_i^2)}{E_{tot}} - \left(\frac{\sum_{hits} E_i \cdot \sqrt{x_i^2 + y_i^2}}{E_{tot}} \right)^2 \tag{3.6}$$

Here x_i, y_i and z_i is the centre of the cells which carry an energy deposition E_i. The total energy deposition in the detector is given by E_{tot}.

In this figure, three types of interactions defined above can be distinguished; the MIP like, the fireball like and the point like interaction. The tail of point like interactions is generated by the fork like interactions. In a next step the latter two types of interactions need to be resolved further.

In the future the simulation studies will be confronted with data in order to identify the hadronic shower model which is best suited to describe these details of a hadronic shower.

3.3.2 Construction of a Technological Prototype

The design of the next generation prototype for a Silicon Tungsten (SiW) electromagnetic calorimeter as described in this document, also called EUDET Module, picks up the two guidelines mentioned in Section 3.3. In comparison with the physics prototype, it emphasises more the understanding and overcoming of the *engineering challenges* imposed by the requirements of the overall design of an ILC detector. Details of the design can be looked up in its Technical Design Report [81]. The main parameters of this module are:

- A pixel size of $5.5 \times 5.5\,\mathrm{mm}^2$
- A total depth of $23\,\mathrm{X}_0$ subdivided into 30 layers.
- The thickness of an individual layer of 3.4 mm and 4.4 mm due to a larger W tungsten thickness in the last 10 layers.

The construction of the final module was preceded by the construction of a so-called *demonstrator* with slightly different dimensions and simplified electronics. The demonstrator allowed for the study of all mechanical aspects of the final module and constitutes an important step towards its realisation. The technological prototype will be exposed to beams starting in 2011. Here, for the first time prototypes with a layout realistic for an ILC detector will be qualified. The results will be compared to those obtained with the physics prototype. The beam test results with the technological prototype will allow for an even more realistic estimation of the precision, which can be expected from an electromagnetic calorimeter at the ILC as well as insight into the operability of such a device during data taking at the ILC.

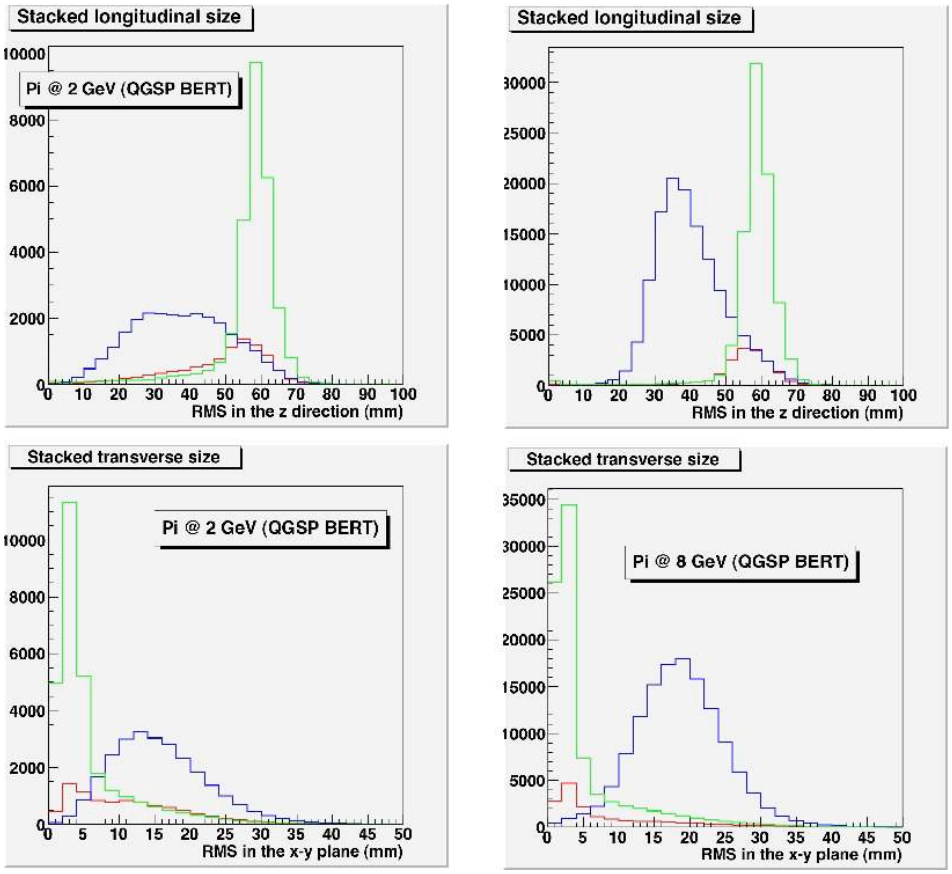

Figure 3.26: *Decomposition of the longitudinal (top) and transversal shower profiles (bottom) into different interaction types for energies of 2 GeV and 8 GeV of incident pions. The coloured histograms indicate the MIP-like interaction (green), the fireball-like interaction (blue) and the punctual interaction (red).*

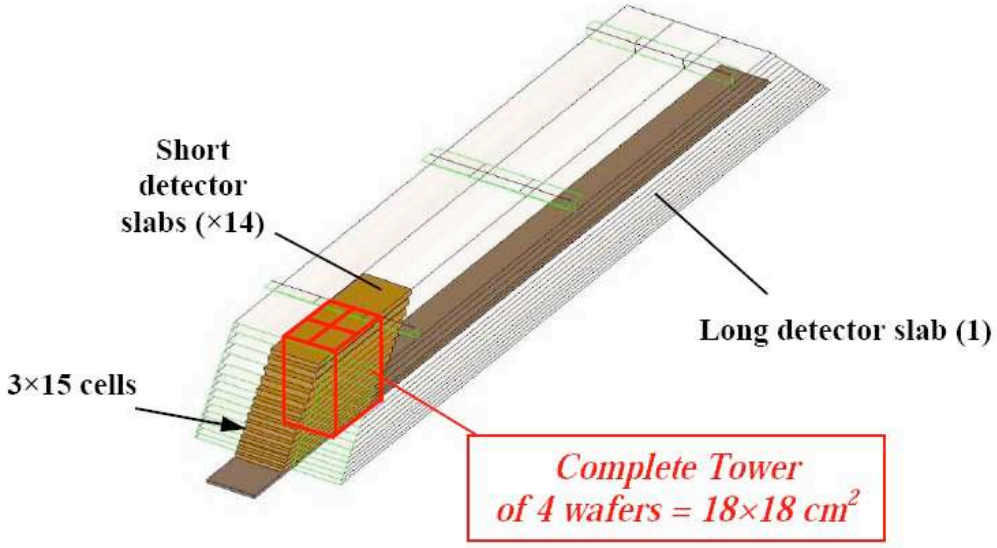

Figure 3.27: *A schematic 3D view of the technological prototype.*

Overall Design

With a size of $1560 \times 545 \times 186\,\mathrm{mm}^3$, the technological prototype has similar dimensions as the modules envisaged for the ILD detector. Figure 3.27, shows the design of the alveolar structure with 3 columns of alveoli of which the middle one will be equipped with sensitive devices mounted on dedicated slabs. The technological prototype has the following sampling at normal incidence: $22.8\,\mathrm{X}_0$ are filled with 20 layers of $0.6\,\mathrm{X}_0$ (2.1 mm) thick tungsten absorber plates, followed by 9 layers of $1.2\,\mathrm{X}_0$ (4.2 mm) thick plates. All but two detector layers have an active area of $18 \times 18\,\mathrm{cm}^2$ segmented into read out cells, or pixels, of $5.5 \times 5.5\,\mathrm{mm}^2$ lateral size which in turn are grouped into 2×2 matrices consisting of 16×16 pixels each. Two layers will be equipped with *long slabs* featuring 8 of these $18 \times 18\,\mathrm{cm}^2$ units. All thirty layers together will comprise 45000 readout channels in total. Table 3.2 lists the main parameters in comparison with those of the physics prototype described in the previous section.

	Physics Prototype	Technological Prototype
Subdivision	3 Structures	1 Structure
W Thickness $n \times d_W$ [mm]	$10 \times 1.4 + 10 \times 2.8 + 10 \times 4.2$	$20 \times 2.1 + 9 \times 4.2$
Depth [X_0]	24	23
Dimensions [mm^3]	$380 \times 380 \times 200$	$1560 \times 545 \times 186$
Smallest Slab Thickness [mm]	8.3	6.8
VFE	outside	inside
# Channels	9720	45360
Weight [kg]	200	700

Table 3.2: *A comparison of parameters of the physics prototype and the technological prototype of the SiW Ecal.*

The Figure 3.28 shows a sketch of the entire alveolar structure and a cross section through one slab. A most prominent change with respect to the physics prototype is that for this technological prototype the very front end electronics will be integrated into the layer structure.

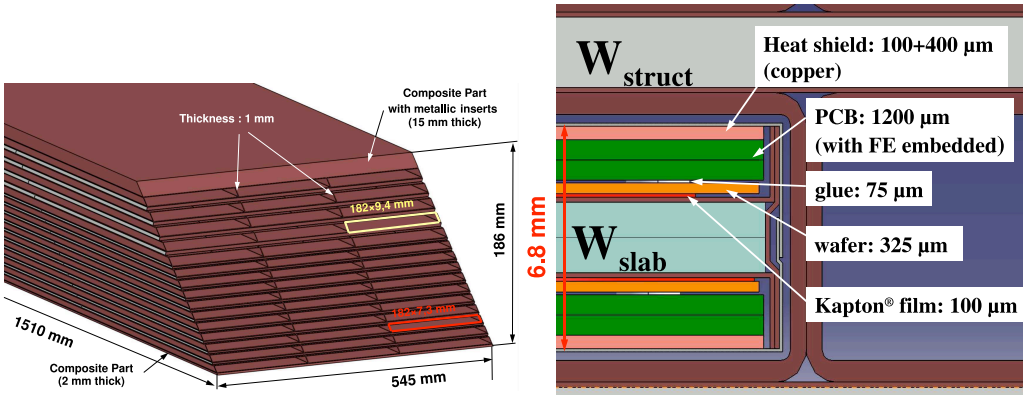

Figure 3.28: *Left: Alveolar structure and its dimensions which houses the sensitive parts of the technological prototype. Right: Cross Section through a slab for the technological prototype. The sensitive components and very front end electronics are mounted on two sides of a tungsten carbon composite plate. The whole slab is embedded in alveolar layers.*

This high level of compactness puts tight tolerances on the size of individual pieces of the very front end electronics. The ensemble PCB and ASIC must not be higher than $1200\,\mu m$. In addition, there is no active cooling to act on the heat produced by the ASICs. Therefore, the ASICs are required to be as little power consuming as possible. This issue will be addressed in more detail later in this section. As indicated above and illustrated in Figure 3.29, a long layer will be equipped with 8 units consisting of 1024 readout cells each. These cells will be glued onto a PCB and equipped with the VFE Chips. The unit of Silicon Wafer, PCB and VFE ASICs is called *Active Signal Unit* or *ASU*. Each layer will be terminated by a so called *Detector Interface* or *DIF* card and an adapter card. The DIF card constitutes the interface to the calorimeter data acquisition while the adapter card will host miscellaneous services like e,g, the power supply for the ASICs.

Mechanical Demonstrator

The mechanical demonstrator has slightly smaller dimensions, $1300 \times 380 \times 70\,\mathrm{mm}^3$, than the technological prototype. It allowed, however, for validating the mechanical feasibility to built large modules by reusing existing material (i.e. the tungsten plates) from the physics prototype. The mechanical structure is built using a similar technique as described for the physics prototype. However, instead of doing the curing in one step, first the alveolar layers were built and then in a second step three alveolar layers were "baked" together with tungsten plates to render the final

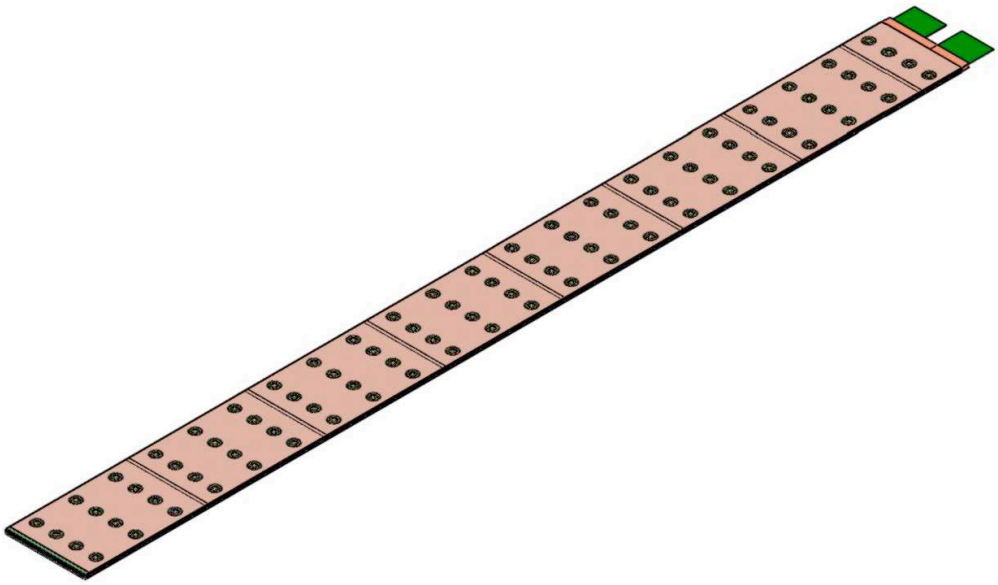

Figure 3.29: *Subdivision of a layer into Analog Signal Units (ASUs). The picture shows an older design with only 7 ASUs. In the current design a layer will comprise 8 ASUs*

structure. The alveolar structure of the demonstrator is shown in Figure 3.30. From precise metrology, the planarity of the structure is given to be between 0.59 mm and 0.65 mm. In addition to the alveolar structure, a H shaped tungsten board dedicated to act as an absorber and to carry the ASUs has been built. For the demonstrator, this board was equipped with 9 cards allowing to study the thermal behaviour of a detector module. One of these cards is equipped with a steerable thermal resistor which simulates the heating ASICs. The resistor can be configured such that it dissipates 1 W at a local position which is to be compared to a total of 0.205 W expected to be generated by the ASICs along the slab. The other cards are equipped with thermometers which allow for the measurement of the temperature gradient along the layer. The extremities of the thermal slab are furnished with mock-ups of the DIF and the adapter card which are also sources of heat. In accordance with the specifications of the TDR, resistors with a heat dissipation of 0.48 W for the adapter card and more than 1.3 W for the DIF card were implemented on these cards. The interconnection between the various thermal cards was realised by heating up a tin-bismuth paste to 200^o C using a halogen lamp. The Figure 3.31 shows the clean interconnection between two individual cards and the complete chain of 9 interconnected boards. This chain of boards got finally wrapped into copper sheets supposed to evacuate the heat. Copper was used for its high heat conduction coefficient of $\lambda = 401\mathrm{W}/(\mathrm{m}\cdot\mathrm{K})$ [82]. The wrapped layer was inserted into the middle of the alveolar structure and subject to a dedicated thermal test. For this test, the other slots of the alveolar structure were also equipped with dummy

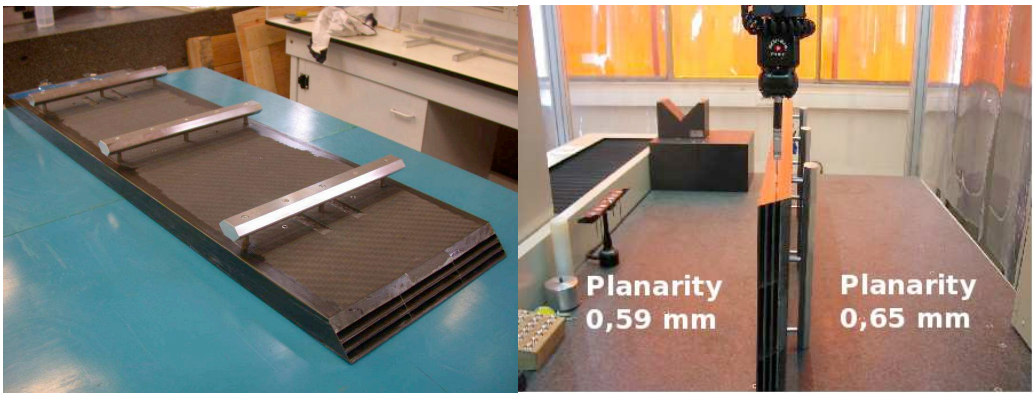

Figure 3.30: *Left: Alveolar structure as built for the demonstrator of the technological prototype. Right: The alveolar structure in the metrology at LAL. The numbers on both sides of the alveolar structure indicate the deviation from planarity of the structure.*

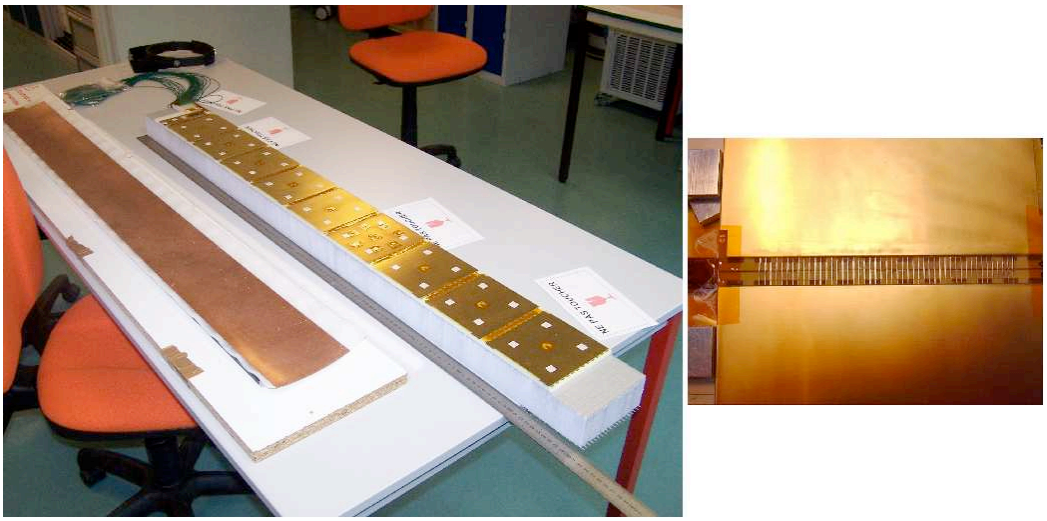

Figure 3.31: *Left: Thermal layer of 9 cards. The layer is wrapped into the copper foil visible to the left of the layer. Left: Interconnection between two thermal boards using the halogen lamp technique.*

slabs generating 1 W each. The Figure 3.32 shows the experimental setup of the thermal test. As can be seen from the figure, the thermal slab is connected to a cooling system. This cooling system consisted of copper blocks which were in

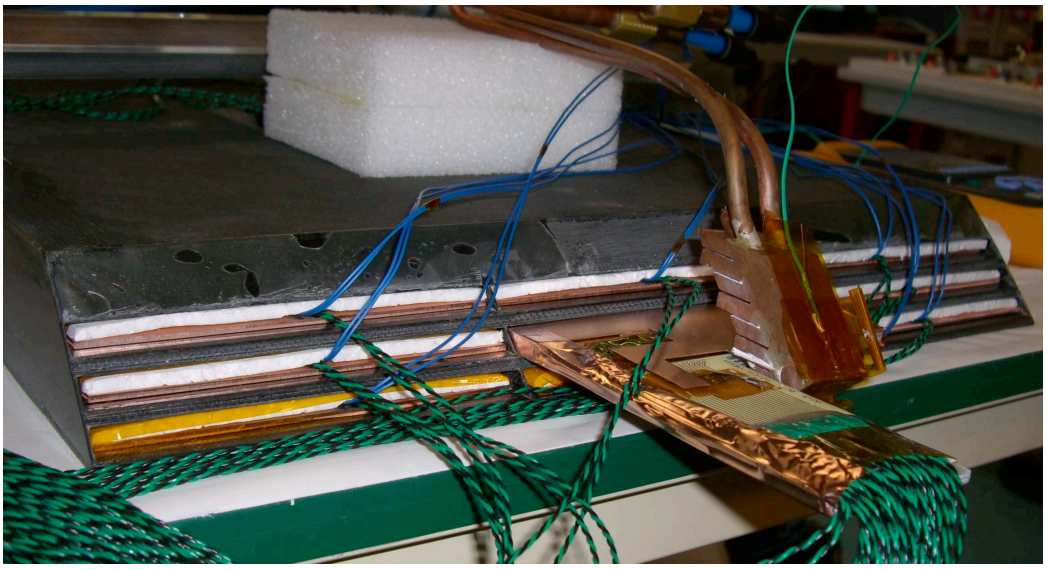

Figure 3.32: *Experimental setup of the thermal test with the demonstrator. The thermal layer has been inserted into the middle of the alveolar structure and is connected to a cooling system.*

turn connected to a water pipe. As it was realised, the cooling system is already very much oriented to the needs for an operation in the ILD detector. In a first step only the heating elements interior to the alveolar structure was powered. The temperature development along the thermal layer is shown in Figure 3.33. These and all subsequent temperatures are read off after the values have been observed to be stable for more than 30 minutes.

The temperature difference between the heated board and the outer extremity was measured to be of the order of 8^o C, the heat is partially transported by the copper layer as can be seen from temperature gradient as measured by the probes along the layer. The Table 3.3 shows the temperature measured in the surrounding layers as well as on top of the alveolar structure. The temperature on top of the structure was found to be 1.5^o C higher than the ambient temperature which indicates that the alveolar structure contributes significantly to the heat transfer.

The temperature gradient when powering the DIF and adapter card is shown in Figure 3.34. As can be seen, the cooling system allows for maintaining these devices as temperatures of at maximum 55^o C. Still this considerable heat dissipation has to be taken into account in the final design of e.g. the ILD detector. A detailed finite element simulation based on the measured data is currently ongoing. The result will deliver important information on the thermal behaviour of the SiW Ecal modules in the final detector and its influence on other detectors. It will be included in the *Detail Base Line Design* of the ILD detector foreseen for 2012. In conclusion, it can

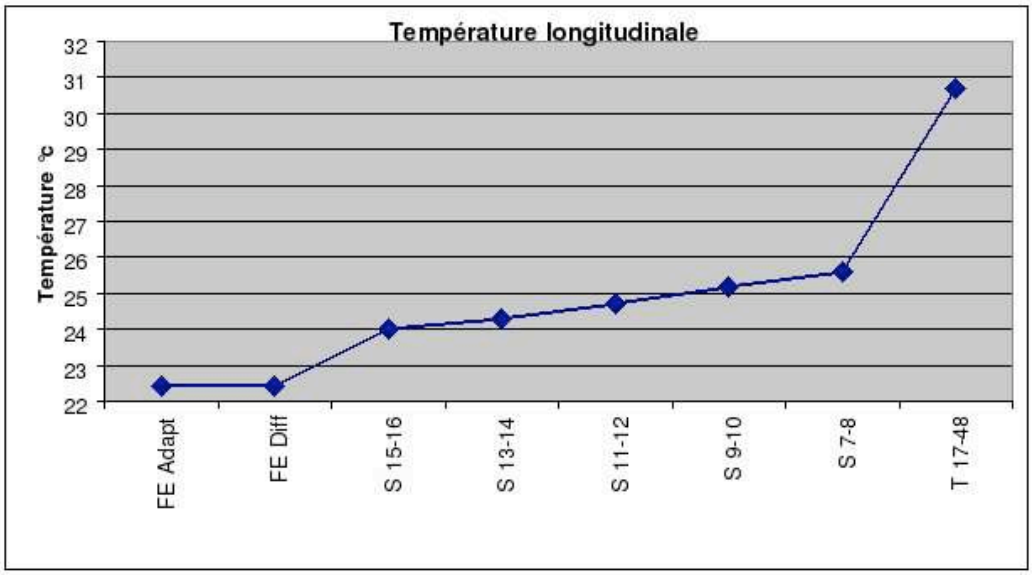

Figure 3.33: *Temperature development along the thermal layer upon powering the resistance located at point 17-48 with 1 W. The more left the points are, the closer they are to the cooling system.*

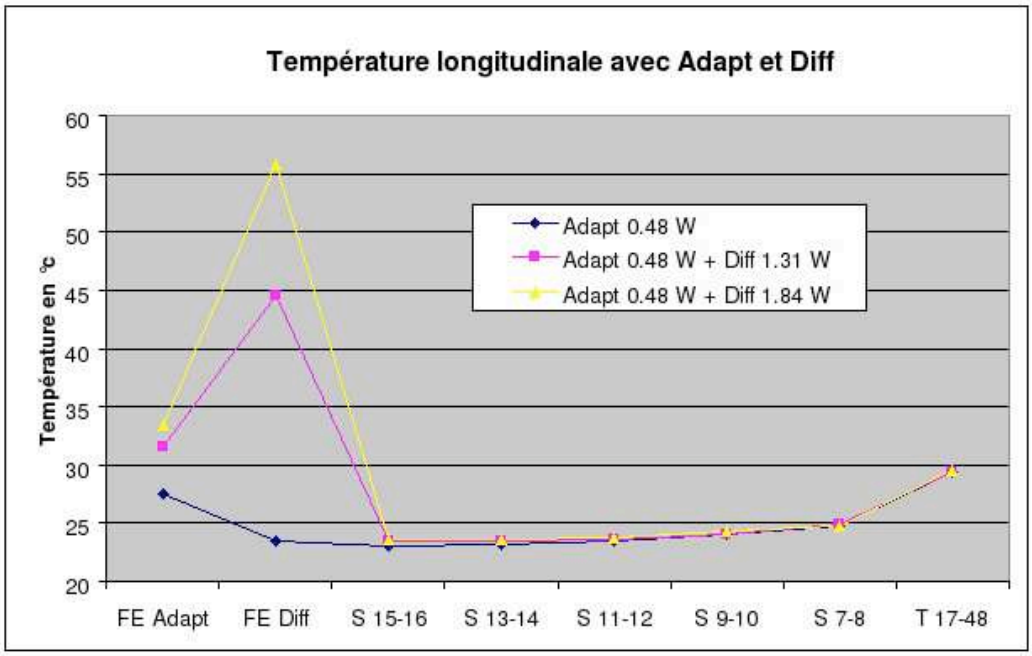

Figure 3.34: *Temperature development along the thermal layer upon powering the cards mimicking the DIF and adapter cards. The more left the points are, the closer they are to the cooling system.*

Ambient Temperature	22		
Alveolar Slot	Left	Middle	Right
External		23.5	
Upper	24.8	24.8	24.6
Lower	25	30.7	25.2
Bottom	25.1	25.2	25.1

Table 3.3: *Temperatures in °C measured in the different alveolar slots when heating each layer with 1 W.*

be stated that the construction and the studies with the demonstrator have proved the mechanical feasibility to construct structures with dimensions as foreseen for an ILC detector. The mechanical concept for the SiW Ecal can therefore considered to be fully validated.

R&D on Silicon Wafers

The sensitive part of an ASU of the technological prototype will consist of a matrix of 32×32 pixels distributed over 4 silicon wafers with a 16×16 segmentation. As can be seen in Figure 3.28 these wafers are supposed to have a thickness of only $325\,\mu$m. As the technological prototype should also constitute a first step towards industrialisation, a first batch of 40 wafers was purchased from Hamamatsu Photonics. These wafers were characterised in terms of the "usual" I-V and C-V curves to study their behaviour in terms of breakdown voltage and depletion region. All wafers show a breakdown at above 500 V. The Figure 3.35 shows a characterisation of a few wafers in terms of C-V. The start of the plateau shows that the wafers get saturated i.e. depleted at a voltage of around 80 V which is well away from the breakdown voltage of the wafers. The dark currents are found to be of the order 0.5μA. The yield of 100%, as obtained from the Hamamatsu Wafers, indicates that the technology to equip the SiW Ecal in an ILC detector is available.

During the operation of the physics prototype, events were observed which exhibit an unnatural square pattern of cells which carry a signal, see Figure 3.36 The R&D for the technological prototype addressed this issue, too. The reason for this square pattern could be traced back to a capacitive coupling between the guard ring and the pixels which induced charge into these pixels which is finally read out by VFE [83]. A remedy to suppress these square events is to segment the guard ring. It is hence decomposed into a series of capacitances which increases the effective impedance of the guard ring and thus suppresses the circulation of currents along the guard ring itself. The Figure 3.37 shows a picture of a segmented guard ring and the level of cross talk for different segmentations of the guard ring. After segmentation the cross talk is attenuated by up to 80%. It can be concluded that the origin of the square pattern is understood and can be taken into account in the future design of silicon wafers.

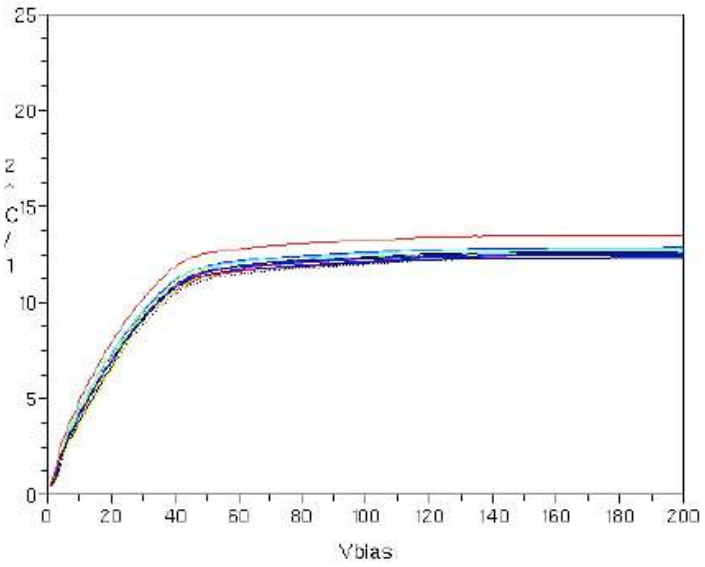

Figure 3.35: *Saturation curves of wafers which will be employed in the technological prototype.*

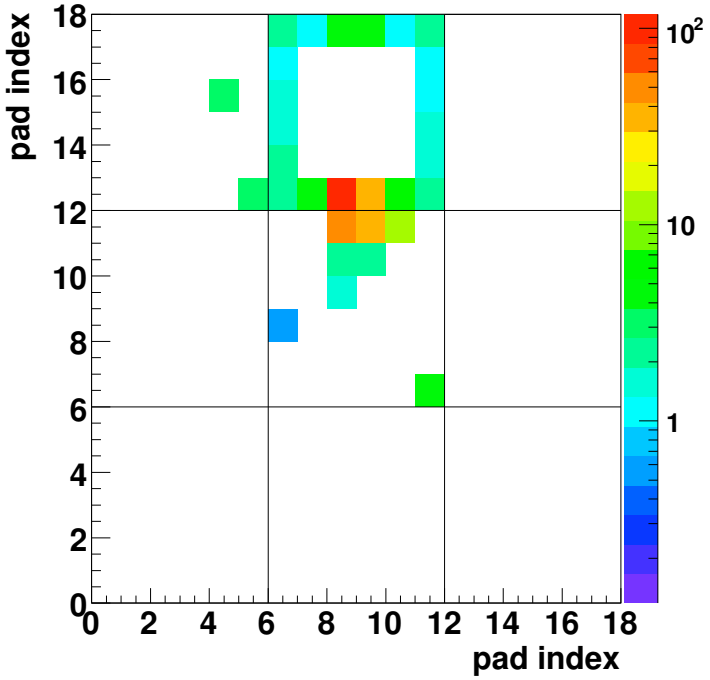

Figure 3.36: *Event with square pattern as observed in the physics prototype.*

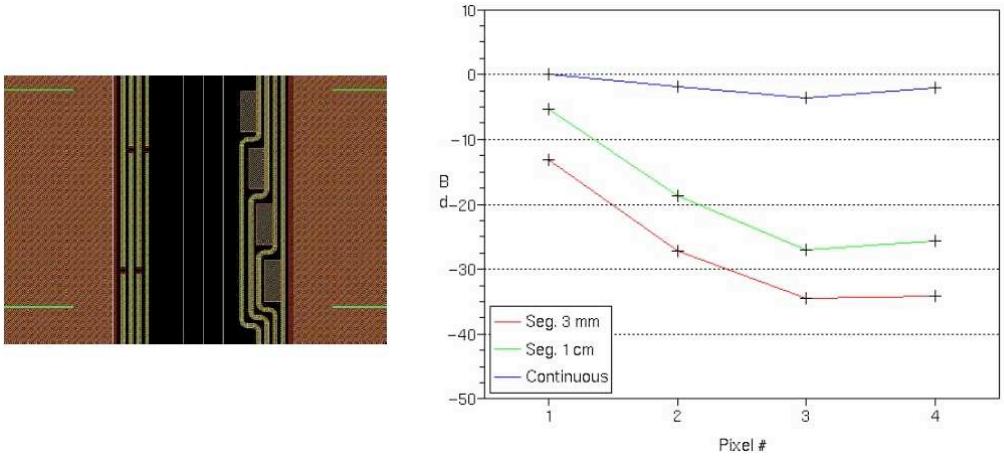

Figure 3.37: *Left: In its left part the photo shows a segmented guard ring. Right: The attenuation for different guard ring segmentation as observed in a test setup.*

Very Front End Electronics - The SKIROC Chip

The ASICs to be conceived for the EUDET Module and hence for the ILC detectors are very challenging. They integrate all of the following steps

- Pre-amplification of the charge deposited in the PIN Diode.
- Shaping of the signal.
- Digitisation and zero suppression on Chip.
- Output of a the digitised signal together with a time stamp equivalent to a bunch crossing ID.

The ASIC designed for the SiW Ecal is called *SKIROC*, which is short for *Silicon Kalorimeter Read Out Chip*. A block diagram of the ASIC is shown in Figure 3.38.

One ASIC is supposed to serve 64 cells with a dynamic range of 3000 MIPS for each of these cells. One of the key design issues for the ASIC is the quest for low power consumption. As outlined above, the requirement of compactness of the ILC detectors does not leave much space for service devices such as cooling. In fact as can be deferred from the basic design, parts interior to the alveolar structure practically do not benefit from any active cooling at all. Therefore, the ASICs have to be designed for ultra low power dissipation. The design value is 25 μW per channel. In order to achieve this small value, a novel technology called *Power Pulsing* will be applied. This technology exploits a distinct feature of the ILC beam structure. As explained above, the beam will arrive in bunch trains with a length of roughly 1 ms. Two bunch trains are mutually separated by about 199 ms. It is foreseen that the electronics will only be switched on during the one millisecond of a bunch train. For the other 200 ms the electronics will be switched off, apart from a short time after

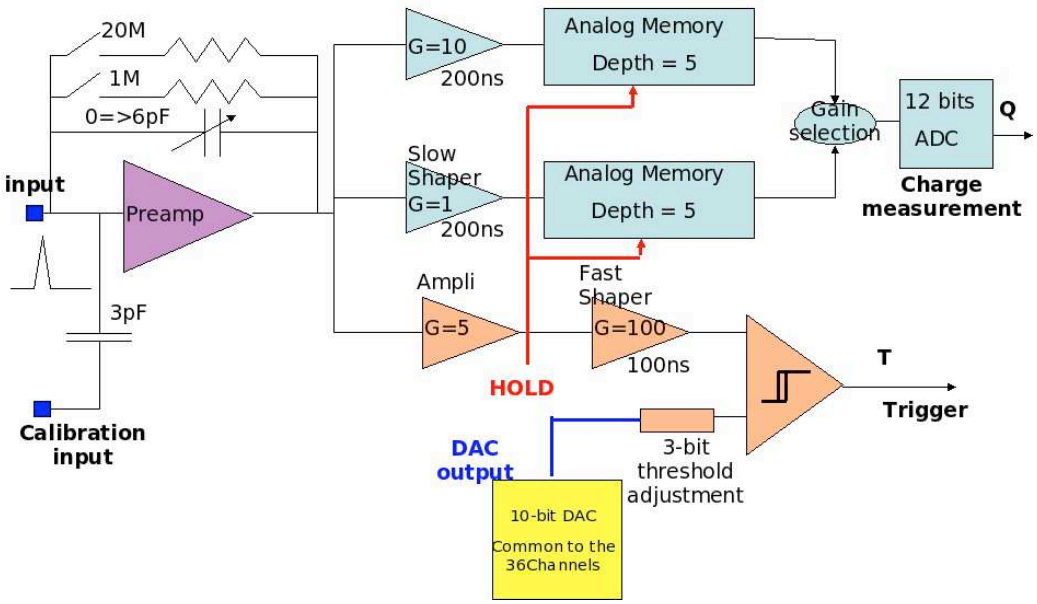

Figure 3.38: *Block channel diagram of one channel of the SKIROC chip. The input signal from a PIN Diode is processed from left to right.*

the bunch train dedicated for data acquisition. The described sequence is illustrated in Figure 3.39

It should be noted that at the time this document is written the Omega team at LAL together with the physics group have operated a SPIROC ASIC for the first time in power pulsing mode. This ASIC is conceived for the technological prototype of the analogue Hcal but shares a large number of functionality with SKIROC. The major difference is the dynamic range where SPIROC covers "only" 500 MIPS. In addition SPIROC can serve only 36 Channels. Due to the still large commonality, and in the current absence of a functional SKIROC, SPIROC was used for characterisation in terms of linearity and noise behaviour [84, 85]. The following results refer to measurements in non-power pulsed mode. As shown in Figure 3.40, the ADC of SPIROC is linear to ± 1 LSB over an input voltage range of about 1.2 V. At the same time, the noise level varies between 0.5 and 1 LSB. The Figure 3.41 shows in its left part, the residuals to the linearity fits of the individual channels and in its right part the difference between the mean of the individual channel and the mean of all channels. For the right part the means were measured at three different input voltages of 1.2,V, 2 V and 2.4 V, respectively. It is important to note that the difference remains constant independent of the input value. This shows that one can correct for this non-uniformity.

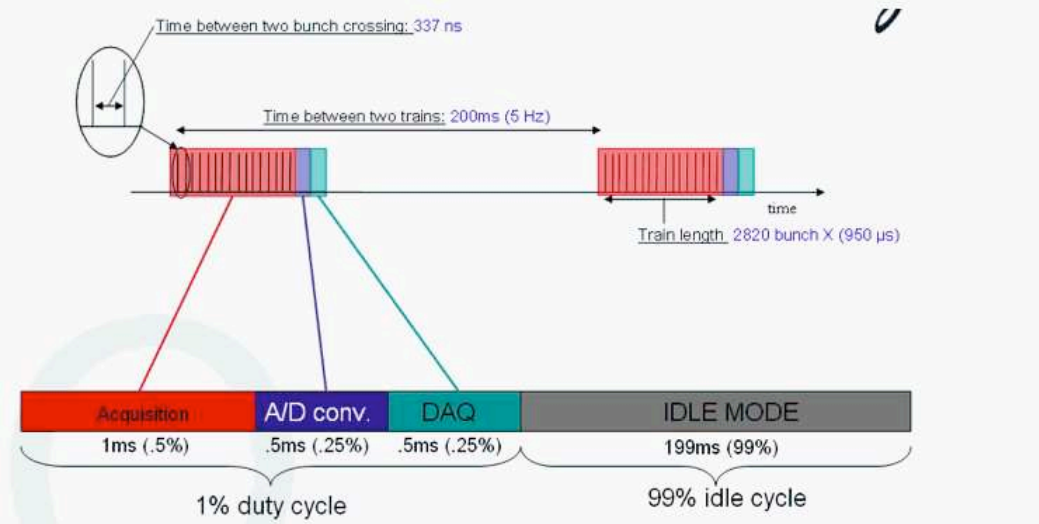

Figure 3.39: *Schematic illustration of the power pulsing in relation to the beam structure of the ILC beam. Apart from a short time at the beginning, the electronics will be switched off in between bunch trains.*

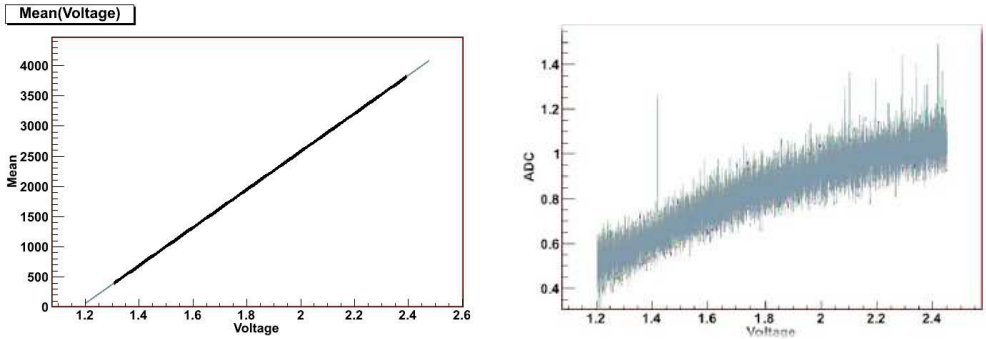

Figure 3.40: *Left: Linearity of the 36 Channels of the SPIROC ADC as a function of the input voltage. Right: Noise of the SPIROC ADC in ADC counts as a function of the input voltage.*

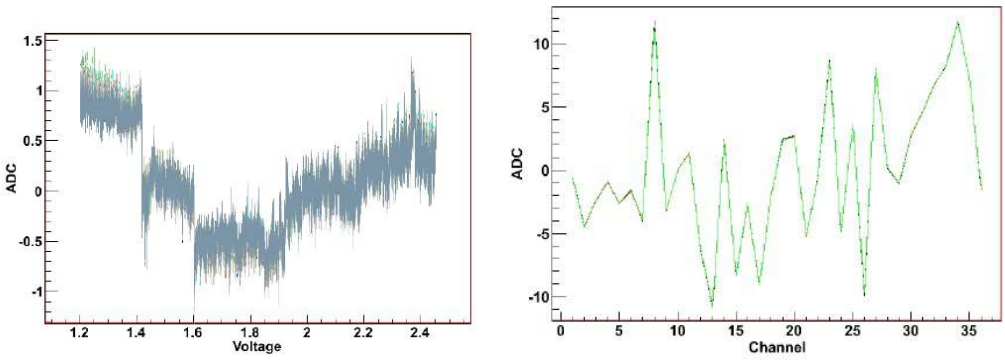

Figure 3.41: *Left: Residuals of the individual channels to the linear fit shown in Figure 3.40. Right: Deviation of the mean of an individual channel from the combined mean of all 36 channels measured for three different input voltages to the ADC. The input voltages are1.2,V, 2 V and 2.4 V.*

3.3.3 Effects of High Energetic Particle Showers on Embedded Front End Electronics

The central calorimeters of the detectors to be operated at the ILC will have the very front end electronics interleaved with the calorimeter layers. The energy of electromagnetic showers produced in the final state of typical e^+e^--collisions ranges between a few MeV up to several hundreds of GeV. A natural question arising from this design is whether the cascade particles of the high energetic showers which penetrate through the electronics do create parasitic signals in these circuits. Those signals would compromise the precision measurements envisaged at the ILC. This section describes the measurements conducted in a special set of runs in which an ordinary calorimeter layer of the physics prototype has been replaced by a prepared test board allowing for the exposure of the very front end electronics to particle showers.

Experimental setup and data taking

For the test, FLC_PHY3 ASICs, see Section 3.3.1, were exposed to electromagnetic showers. One ASIC has a surface of about $1.6 \times 2.3\,\mathrm{mm}^2$. It is TQFP64 packaged such that the whole ensemble, which will be called Chip herafter, has outer dimensions of about $1 \times 1\,\mathrm{cm}^2$ [85]. The shower particles may create charges and thus a parasitic signals in the PMOS at the entrance of the Pre-Amplifiers of the 18 channels. The sensitive area of one channel is about $3000\,\mu m^2$ while the total surface of a channel of about $110000\,\mu\mathrm{m}^2$.

A PCB equipped with four FLC_PHY3 chips in the nominal sensitive plane was mounted directly on a spare H-Board as shown in Figure 3.42. This board was placed at the expected position of the shower maximum. In this configuration, data with electrons with an energy of 70 GeV and 90 GeV were recorded. The beam was positioned at five different points along the x-direction at the centre in y as indicated

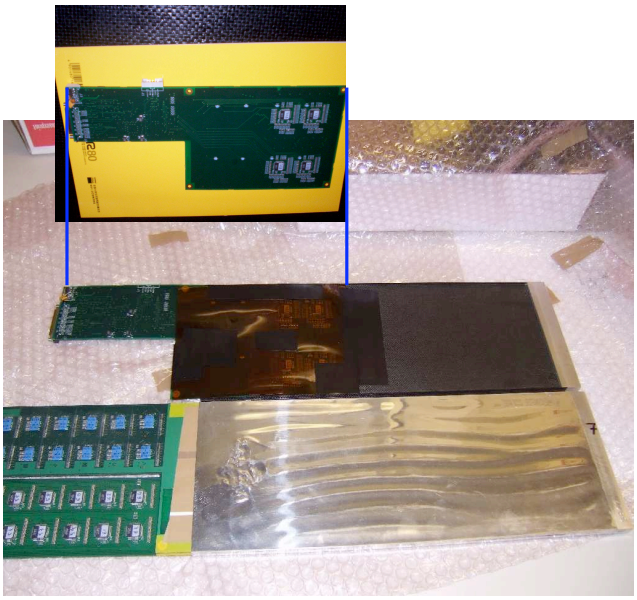

Figure 3.42: *Testboard mounted on tungsten absorber and comparison with fully equipped slab.*

for the 'Chip 1' in Figure 3.43 for each of the four chips for a total of 20 positions.

The regular events triggered with scintillation counters, thus beam events, are interleaved during the data taking with pedestal events triggered by an oscillator integrated into the CALICE data acquisition system. The data were recorded during the 2007 beam test campaign at CERN in the H6 beam test area. Table 3.4 gives the number of recorded Signal and Pedestal Events at each measurement point. The table also introduces the nomenclature used hereafter to identify the various measurement points.

Data Analysis and Results

The data are verified for the shower development and for a proper alignment of the chips w.r.t. to the beam orientation. Figure 3.44 shows the spectra of a run with electrons of 90 GeV. Here, the recorded data have been subject to the same reconstruction chain as applied to the regular data taking which in particular introduces a zero suppression at a value of 0.4 MIP.

The total energy spectrum exhibits a clear maximum well separated from residual noise and MIP events. The gap visible in the longitudinal shower profile indicates that the special layer was well placed at the maximum of the electromagnetic shower. The orientation of the layers is such that the lateral position of the special PCB, installed at the position of Layer 12, is identical to that of the Layer 2 of the prototype. Figure 3.45 shows the hit maps for about 5000 electron events in the

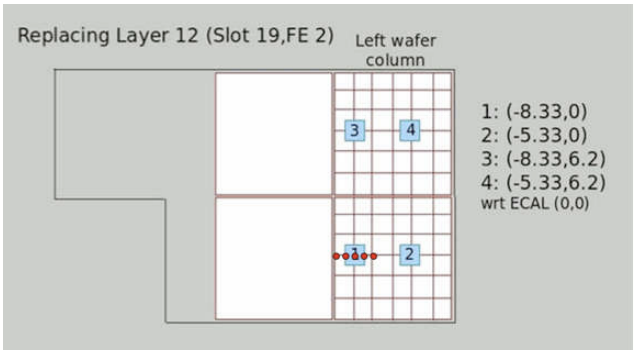

Figure 3.43: *Schematic view of the special board. The points indicate the nominal five impact points for a scan over Chip 1. Identical scans have been performed for the other three Chips.*

Layers 2 and 14. Layer 14 is the first regular layer behind the Layer 12 and shifted by only 1.3 mm with respect to Layer 12. The projection of the position of Chip 4 into these layers is indicated by a full square.

It is clearly visible that the beam hits the detector close to the chip position and that the lateral shower development leads to a good coverage and thus good exposure to shower particles of the chip.

In a next step, the regular zero suppression was switched off in the CALICE reconstruction program in order to get sensitive to the behaviour of the chips in the small signal range. In [76] it is reported that a Minimal Ionising Particle (MIP) creates a signal of approximately 45 ADC counts. This value serves as a reference for the studies in the present document. During the analysis it was observed that the first signal of each chip has a relatively high correlation of greater than 0.5 with the first signal of the other chips. The reason for this might be a imperfect isolation of the connector to the CALICE DAQ system. These signals are hence discarded from the analysis, leaving 17 signals per chip per event. The search for parasitic signals is performed by sub-dividing the data samples into *Signal Events* and *Pedestal Events*. Signal Events are further selected by requiring an energy deposition of more than 2000 MIPS in order to be unbiased by low energy events when tracing parasitic signals. This cut is also motivated by the energy spectrum shown in Fig. 3.44. It reduces the available statistics quoted in Table 3.4 by approximately 15%. Still no difference between the noise spectra of these two event types is expected. The Figure 3.46 shows the noise spectra for Signal and Pedestal Events as an example for a scan over Chip 4. Indeed, no difference between the two data types can be observed. After this more qualitative result, the mean and the root mean square (rms) for each chip at each scan point is extracted for Signal and Pedestal Events. The results are displayed in Figures 3.47 to Fig. 3.50. From these figures the following conclusions can be drawn:

- The mean and the rms remain the same throughout all the runs. In particular,

Scan	Scanpoint	Position - x,y [cm]	Signal Events	Pedestal Events
Chip 1	1	-9.33, 0	78293	14624
	2	-8.83, 0	189966	37173
	3	-8.33, 0	209312	38361
	4	-7.83, 0	65249	3602
	5	-7.33, 0	85543	4306
Chip 2	1	-6.33, 0	85188	4678
	2	-5.83, 0	129778	6146
	3	-5.33, 0	213369	13719
	4	-4.83, 0	217111	11053
	5	-4.33, 0	89435	4254
Chip 3	1	-9.33, 6.2	90395	4347
	2	-8.83, 6.2	228138	10296
	3	-8.33, 6.2	216877	9831
	4	-7.83, 6.2	218519	9462
	5	-7.33, 6.2	86989	3909
Chip 4	1	-6.33, 6.2	66655	4223
	2	-5.83, 6.2	214418	13666
	3	-5.33, 6.2	314275	15264
	4	-4.83, 6.2	217415	11698
	5	-4.33, 6.2	85884	4949

Table 3.4: *Protocol of the exposure test containing the identifiers of the scanning points, their position and the number of Signal and Pedestal Events recorded at each position.*

no dependence on the scan position can be observed

- The mean and rms for signal and pedestal events are always nearly identical. Residual differences are smaller than 1% of a MIP.

The results obtained so far indicate that the embedding of the very front end electronics does not compromise the performance of the detector. An analysis on the extraction of upper limits on parasitic hits is currently ongoing.

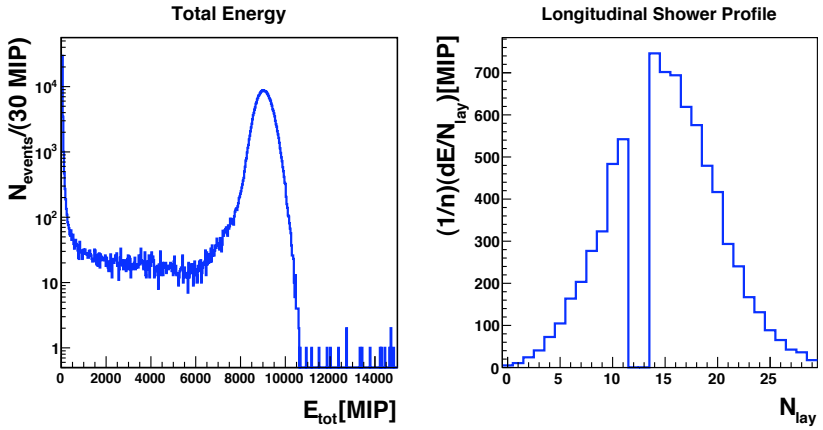

Figure 3.44: *Total energy deposition and longitudinal shower profile for a run with electrons of 90 GeV during the test of the special PCB.*

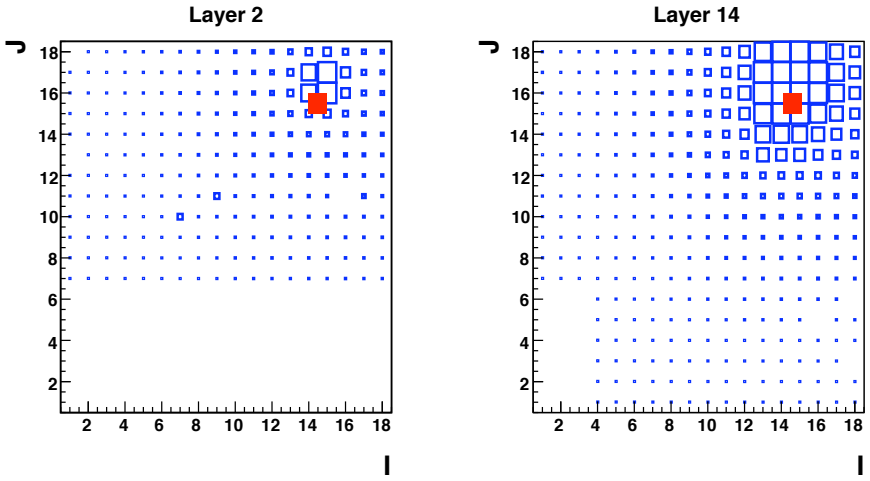

Figure 3.45: *Hit maps shown as a function of the cell indices I, J in x and y-direction in layer 2 and 14. The box sizes represent the number of recorded hits in the individual cells. The position of Chip 4, indicated by the full square, the projected into the planes of these layers.*

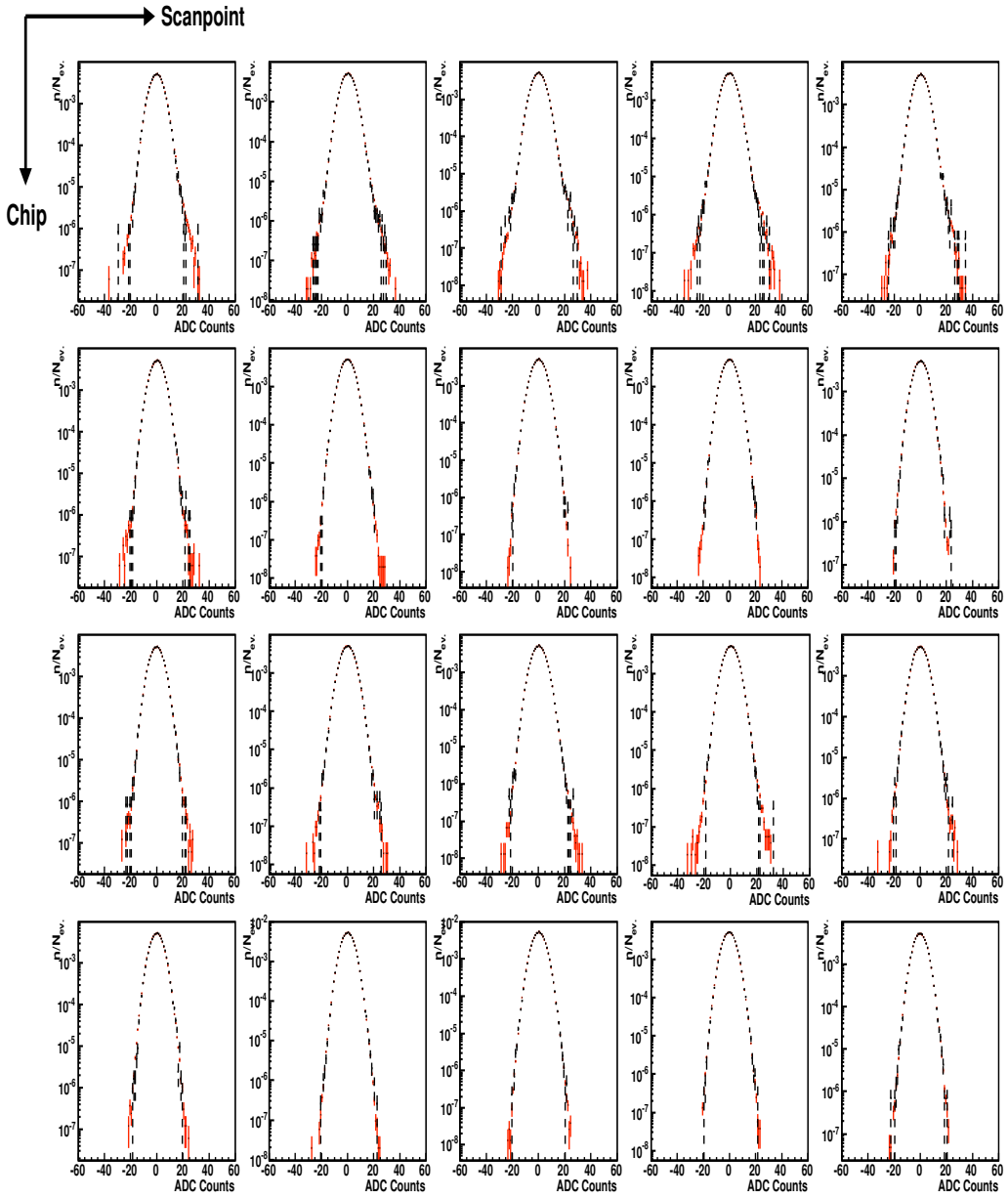

Figure 3.46: *Noise spectra for Signal Events (red) and Pedestal Events (black). The figure displays the result for Scan 4.*

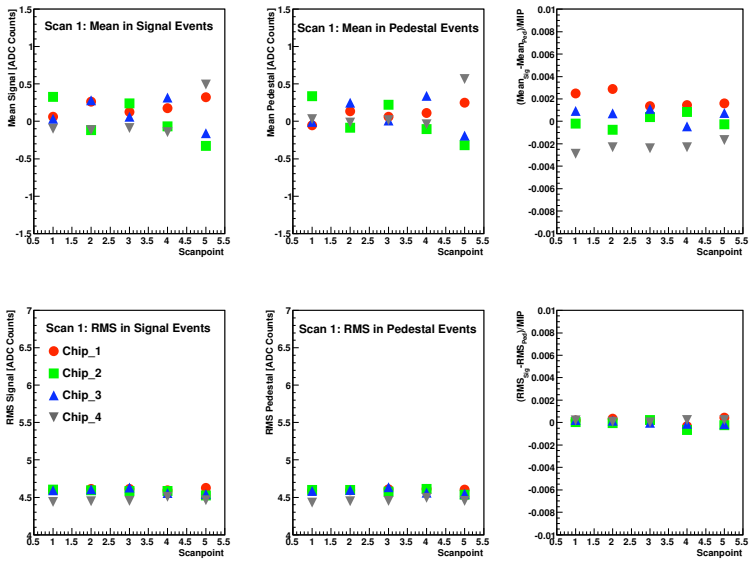

Figure 3.47: *Mean and RMS for Signal Events and Pedestal Events. The very right part shows the corresponding differences normalised to the value of a MIP assumed to be 45 ADC counts. Statistical Errors are negligible. The figure displays the result for Scan 1.*

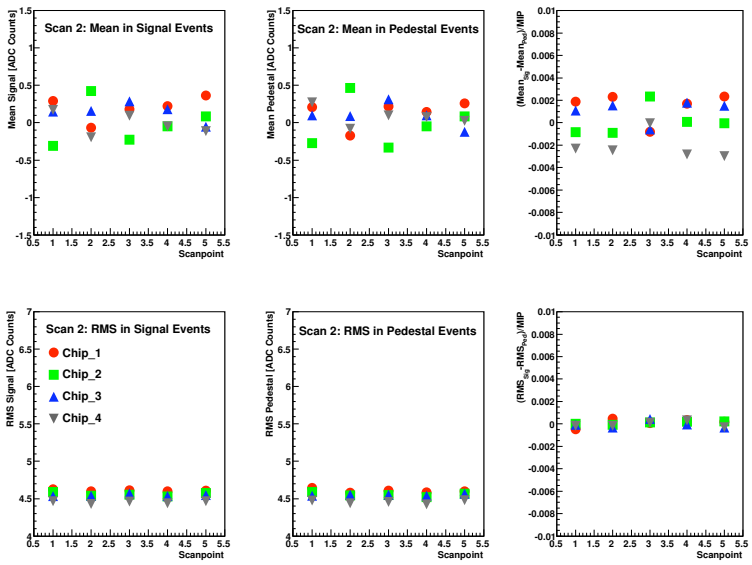

Figure 3.48: *Mean and RMS for Signal Events and Pedestal Events. The very right part shows the corresponding differences normalised to the value of a MIP assumed to be 45 ADC counts. Statistical Errors are negligible. The figure displays the result for Scan 2.*

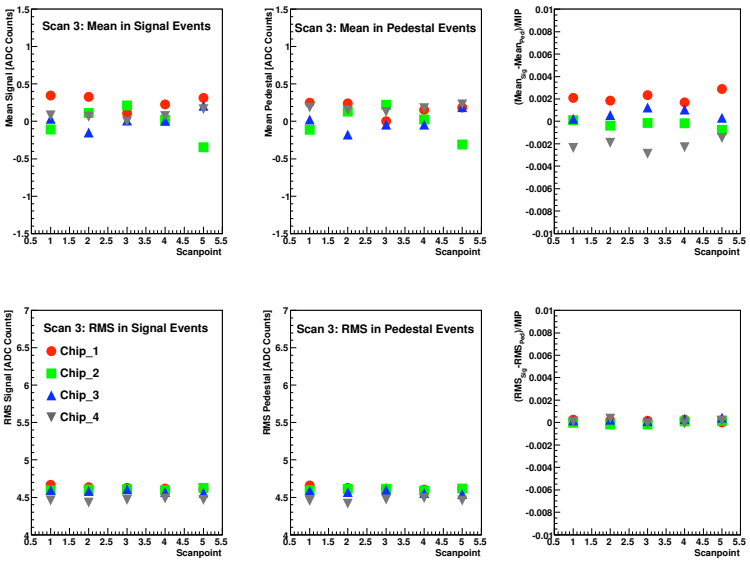

Figure 3.49: *Mean and RMS for Signal Events and Pedestal Events. The very right part shows the corresponding differences normalised to the value of a MIP assumed to be 45 ADC counts. Statistical Errors are negligible. The figure displays the result for Scan 3.*

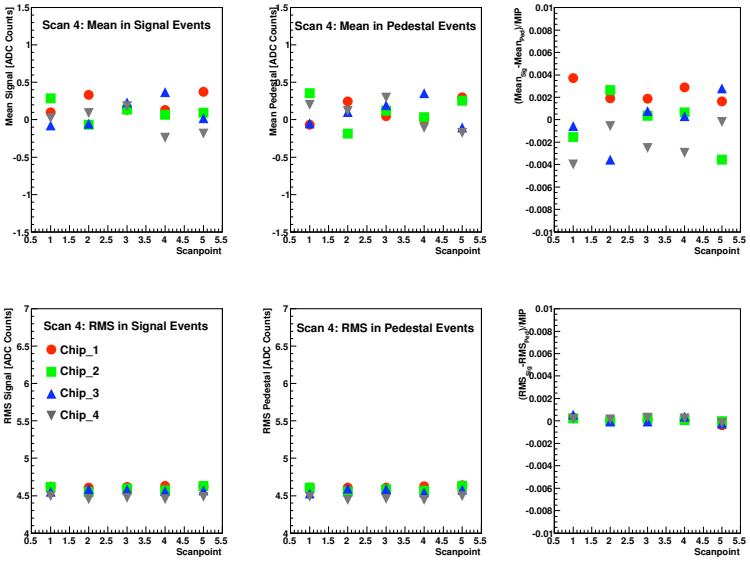

Figure 3.50: *Mean and RMS for Signal Events and Pedestal Events. The very right part shows the corresponding differences normalised to the value of a MIP assumed to be 45 ADC counts. Statistical Errors are negligible. The figure displays the result for Scan 4.*

Chapter 4

Higgs Mass and Higgs-strahlung Cross section at the ILC

Contents

As motivated in the previous chapters, electro-weak symmetry breaking is intimately coupled to the study of the Higgs boson. It appears as a consequence of the observation of massive gauge bosons which can be generated by the spontaneous breaking of the $SU(2)_L \times U(1)_Y$ symmetry of the electroweak Lagrangian.

The ILC will allow for the detailed investigation of the nature of the Higgs boson as has been shown in [86, 87, 88] and references therein. For the Letter of Intent Studies of the detector concepts, see Section 3.2, it was proposed to study as a benchmark the production of a Standard Model Higgs boson with $m_H = 120\,\text{GeV}$ at a centre-of-mass energy $\sqrt{s} = 250\,\text{GeV}$ [89]. For these parameters, the most relevant production mechanism is the Higgs-strahlung process, see Section 2.5.

By detecting the decay products of the Z boson the Higgs-strahlung allows for the search of Higgs signals without any further assumption on its decay modes since also the initial state is perfectly known. Thus, the ILC permits an unbiased or *Model Independent* search for the Higgs boson which is a major advantage in comparison with hadron colliders such as the LHC. The presumably cleanest way to study Higgs boson production is given by the reaction chain $e^+e^- \to HZ$ and the subsequent decays $Z \to \mu^+\mu^-$ or $Z \to e^+e^-$, i.e. regarding decays of the Z boson into well measurable electron and muon pairs. These channels, also named $\mu\mu X$-channel and eeX-channel hereafter, have been examined in detail in [79, 90]. The results given in the references are summarised in this article.

4.1 Event Samples

The study is based on events generated with the event generator Whizard [91] which are subject to a detailed simulation of the ILD detector. For simulation the MOKKA [92] software package was used which provides the geometry interface to the GEANT4 simulation toolkit. The event reconstruction was performed using the MarlinReco framework. For this study, the versions as contained in the Software Package *ILCSoft v01-06* [92] were employed.

The incoming beams were simulated with the GUINEA-PIG package [93]. The energy of the incoming beams was smeared with an energy spread of 0.28% for the electron beam and with 0.18% for the positron beam. In addition, the energy was modulated by beam-strahlung. The generated signal and background samples are given in the Table 4.1 for the beam polarisation mode

$$e^-_L e^+_R\text{: } P_{e^-} = -80\% \text{ and } P_{e^+} = +30\%$$

and in Table 4.2 for the beam polarisation mode

$$e^-_R e^+_L\text{: } P_{e^-} = +80\% \text{ and } P_{e^+} = -30\%.$$

The initially generated samples of the signal are combined such that they yield $\mathcal{L} = 10\,\text{ab}^{-1}$ in each of the polarisation modes. For background samples the integrated luminosity is mostly larger than $250\,\text{fb}^{-1}$. Where it is smaller, it is still provided that the samples contain considerable statistics. Note, that in Tables 4.1 and 4.2 the background samples are grouped by the resulting final state.

Process	Cross-Section
$\boldsymbol{\mu\mu X}$	**11.67 fb**
$\mu\mu$	10.44 pb
$\tau\tau$	6213.22 fb
$\mu\mu\nu\nu$	481.68 fb
$\mu\mu ff$	1196.79 fb

Process	Cross-Section
$\boldsymbol{eeX}$	**12.55 fb**
ee	17.30 nb
$\tau\tau$	6213.22 fb
$ee\nu\nu$	648.51 fb
$eeff$	4250.58 fb

Table 4.1: *Processes and cross sections for polarisation mode* $e^-_L e^+_R$. *The signal is indicated by bold face letters.*

As can be seen from Tables 4.1 and 4.2, the expected background exceeds the signal by up to six orders of magnitude. As the study is performed model independent, the largest background is expected from lepton pair production. On the other hand, the boson pair production and in particular the Z pair production leads to a final state which is very much similar to that of the signal. A major challenge of the analysis is thus to suppress the considerable background. In the following, selected steps of signal selection and background suppression will be presented. Emphasis is put on those steps which highlight the potential for precision measurements with the ILD detector.

Process	Cross-Section
$\boldsymbol{\mu\mu X}$	**7.87 fb**
$\mu\mu$	8.12 pb
$\tau\tau$	4850.05 fb
$\mu\mu\nu\nu$	52.37 fb
$\mu\mu ff$	1130.01 fb

Process	Cross-Section
$\boldsymbol{eeX}$	**8.43 fb**
ee	17.30 nb
$\tau\tau$	4814.46 fb
$ee\nu\nu$	107.88 fb
$eeff$	4135.97 fb

Table 4.2: *Processes and cross sections for polarisation mode* $e^-_R e^+_L$. *The signal is indicated by bold face letters.*

4.2 Signal Selection and Background Rejection

The signal is selected by identifying two well measured leptons in the final state which yield the mass of the Z boson. The mass M_{recoil} of the system recoiling to the di-lepton system is computed using the expression:

$$M^2_{recoil} = s + M^2_Z - 2E_Z\sqrt{s}$$

Here M_Z denote the mass of the Z boson as reconstructed from the di-lepton system and E_Z its corresponding energy. Techniques of background suppression similar to those applied in the present study were already introduced in [94]. This section firstly defines the criteria of lepton identification and then addresses the means to suppress the background.

4.2.1 Lepton Identification and Track Selection

The task is to identify the muons and electrons produced in the decay of the Z boson. The momentum of the decay leptons is in the range $15 < P < 90\,\text{GeV}$. In a first step, the energy deposition in the electromagnetic calorimeter (E_{ECAL}), the total calorimetric energy E_{total} and the measured track momentum P_{track} are compared accordingly for each final state particle. The lepton identification is mainly based on the assumption that an electron deposits all its energy in the electromagnetic calorimeter while a muon in the considered energy range passes both the electromagnetic and the hadronic calorimeter as a minimal ionising particle. The observables and cut values are summarised in Table 4.3.

	μ-Identification	e-Identification
E_{ECAL}/E_{total}	< 0.5	> 0.6
E_{total}/P_{track}	< 0.3	> 0.9

Table 4.3: *Electron and muon identification criteria based on tracking and calorimetric information.*

The criteria to estimate the quality of the lepton identification and hence the

signal selection are the *Efficiency* and *Purity*. These are defined as follows:

$$\text{Efficiency} = \frac{\text{N}_{\text{true}\cap\text{iden}}}{\text{N}_{\text{true}}}$$

$$\text{Purity} = \frac{\text{N}_{\text{true}\cap\text{iden}}}{\text{N}_{\text{iden}}}$$

Here N_{true} defines the generated number of the corresponding lepton type and N_{iden} defines the reconstructed number of the corresponding lepton type according to the selection criteria. The expression $\text{N}_{\text{true}\cap\text{iden}}$ denotes the number of events in the intersection of generated and reconstructed lepton types. For electrons and muons with $P > 15\,\text{GeV}$ in the signal samples, the efficiencies and purities are well above 95% except for the purity of the muon identification which is only 91%. This is caused by final state charged pions which pass the detector as minimal ionising particles and which are indistinguishable from muons with the applied selection criteria. This deficiency is partially balanced by the fact that two leptons of the same type with opposite charge are required for the reconstruction of the Z boson and that they should yield the mass of the Z boson. Indeed, using the above selection cuts, the efficiency to identify both leptons from the Z boson decay is 95.4% for the case $\text{Z} \to \mu\mu$ and 98.8% for the case $\text{Z} \to ee$. Note, that the cut on $P > 15\,\text{GeV}$ has been omitted in this case.

As the invariant mass of the Z boson and thus of the recoil mass will be calculated from the four-momenta of the tracks, badly measured tracks need to be discarded from the analysis. The track quality can be estimated by the ratio $\Delta P/P^2$ where the uncertainty ΔP is derived from the error matrix of the given track by error propagation.

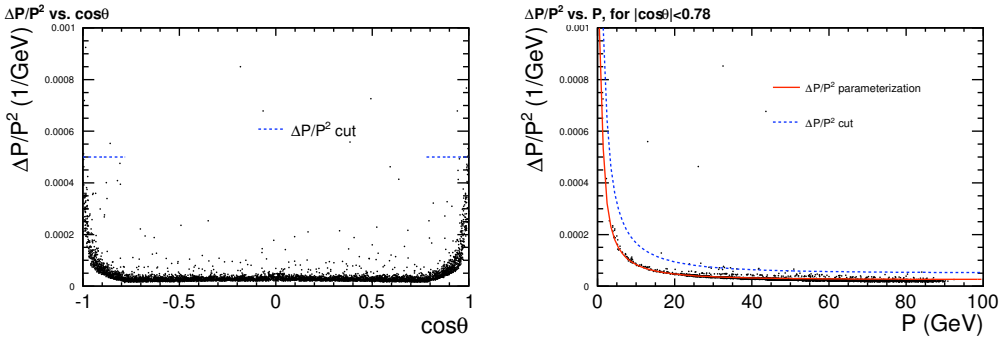

Figure 4.1: *2D $\Delta P/P^2$ distribution vs. $\cos\theta$ (left) and $\Delta P/P^2$ distribution vs. track momentum (right) of muon candidates*

The Figures 4.1 and 4.2 show, separately for muons and electrons, the dependency of $\Delta P/P^2$ on the polar angle $\cos\theta$ and on the track momentum P. For reasons discussed in the following, the latter has been restricted to $|\cos\theta| < 0.78$, i.e. the central region. For both variables, the distributions exhibit for muon tracks a narrow band with well measured momenta equivalent to small $\Delta P/P^2$. The track

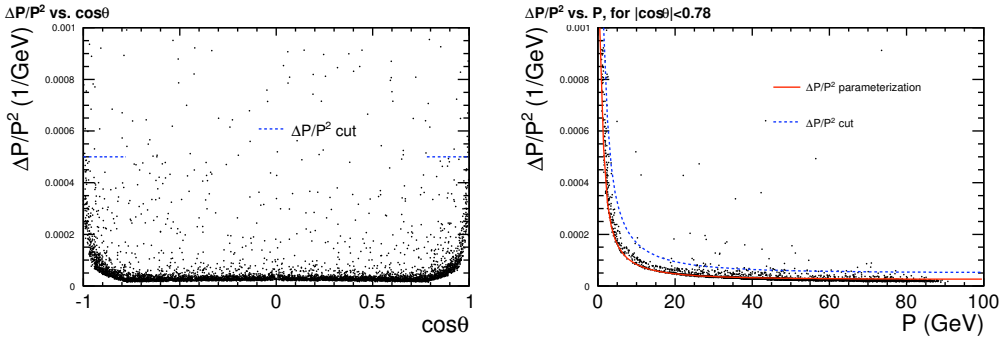

Figure 4.2: *2D $\Delta P/P^2$ distribution vs. $\cos\theta$ (left) and $\Delta P/P^2$ distribution vs. track momentum (right) of electron candidates*

quality decreases as expected towards large $|\cos\theta|$, i.e. towards the acceptance limits of the TPC which motivates the restriction to the central region when displaying $\Delta P/P^2$ versus P. These distributions show a decrease in track quality towards small particle momenta as expected from multiple scattering effects. Beyond that, it is clearly visible that for electrons the situation is much more diluted and the number of badly measured tracks is significantly higher than that for muons. This can be explained by bremsstrahlung of the electrons in the detector material.

The procedure for track rejection is developed for the better measured muon induced tracks:

- For $|\cos\theta| < 0.78$ the shape of $\Delta P/P^2$ versus P is approximated by:

  $$\delta(1/P) = \Delta P/P^2 = a \oplus b/P = c(P); \text{ with } a = 2.5\times10^{-5}\,\text{GeV}^{-1} \text{ and } b = 8\times10^{-4}. \tag{4.1}$$

  which corresponds to the nominal track momentum resolution of the TPC. Tracks are rejected if $\delta(1/P) > 2c(P)$.

- For $|\cos\theta| > 0.78$ tracks are rejected if $\Delta P/P^2 > 5 \times 10^{-4}\,\text{GeV}^{-1}$.

The cuts are indicated in Figure 4.1 and 4.2 and underline that tracks created by electrons are rejected considerably more often which will reduce the number of reconstructed Z bosons in the corresponding channel.

4.2.2 Background Rejection

The recoil analysis is based on the identification of the di-lepton system as produced by the decay of the Z boson. It is thus necessary to distinguish the processes which lead to two leptons in the final state as given in Table 4.1 and Table 4.2 from the ones produced in the Higgs-strahlung process. The cuts against background are introduced in the following:

- For the Higgs-strahlung process, the invariant mass of the di-lepton system M_{dl} should be equal to the Z boson mass while the invariant mass of the recoiling

system, M_{recoil} is expected to yield the introduced mass of the Higgs boson of 120 GeV. It is unlikely that combinations of background processes fulfil both conditions at once. The analysis is therefore restricted to the following mass ranges:

  - $80 < M_{dl} < 100\,\text{GeV}$
  - $115 < M_{recoil} < 150\,\text{GeV}$

- Acoplanarity *acop*: As for e^+e^- collisions with beams of equal energy the centre-of-mass system is at rest, it is expected that in processes in which the leptons are produced at the Z^* vertex these two leptons are back-to-back in azimuth angle. The distance in azimuth angle is expressed by the acoplanarity *acop*, defined as $acop = |\phi_{\ell^+} - \phi_{\ell^-}|$, where $\phi_{\ell^\pm}$ is the azimuth angle of the an individual lepton of the di-lepton system. If the particles are produced from a intermediate particle with a given transverse momentum, the exact back-to-back configuration is modulated. Therefore a cut on $0.2 < acop < 3$ is applied.

- Transverse Momentum P_{Tdl} of the di-lepton system: As the Higgs-strahlung process can be interpreted as a two body decay, both bosons gain equal transverse momentum which is conserved by their decay products. The total final state for muon pair production or Bhabha Scattering has in first approximation no transverse momentum. In order to suppress this background, a cut $P_{Tdl} > 20\,\text{GeV}$ of the di-lepton system is applied. This cut cannot suppress events in which initial state radiation of the incoming beams leads to a transverse momentum of the colliding system. This case will be discussed separately.

- $|cos\theta_{missing}| = |\sum P_{z,miss}|/|\sum P_{miss}|$: This cut discriminates events which are unbalanced in longitudinal momentum, essentially, those of the type $e^+e^- \to \ell^+\ell^-\gamma$, see Figure 1.2. A cut on $|cos\theta_{missing}| < 0.99$ is applied.

The last introduced cut also suppresses events with initial state radiation happening approximately collinear with the incoming beams. The final state in $e^+e^- \to \mu^+\mu^-(e^+e^-)$ can, however, gain sizable transverse momentum by initial state radiation of a high energetic photon. Figure 4.3 shows the correlation between the transverse momentum $P_{T\gamma}$ of a detected high energetic photon, assumed to be created by initial state radiation, and the transverse momentum P_{Tdl} of the di-lepton system for both, events in which only a muon pair is created at the Z^*- Boson vertex and signal events. The first type shows a clear correlation in transverse momentum. In order to suppress this background the variable $\Delta P_{Tbal.} = P_{Tdl} - P_{T\gamma}$ is introduced which is shown in Figure 4.4 for signal events and background events superimposed with each other. By selecting events with $\Delta P_{Tbal.} > 10\,\text{GeV}$, 90% of the remaining background by lepton pair production can be suppressed. Background events of type

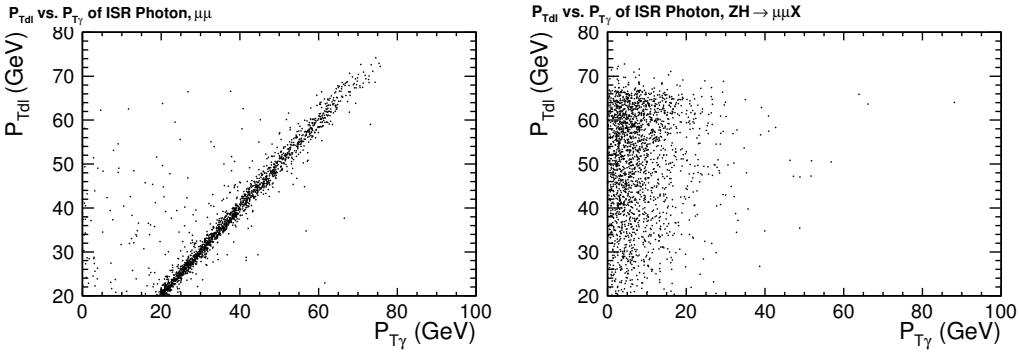

Figure 4.3: P_{Tdl} *vs.* $P_{T\gamma}$ *for background by* $e^+e^- \to \mu^+\mu^-$ *(left) and for signal (right) in the* $\mu\mu X$*-channel.*

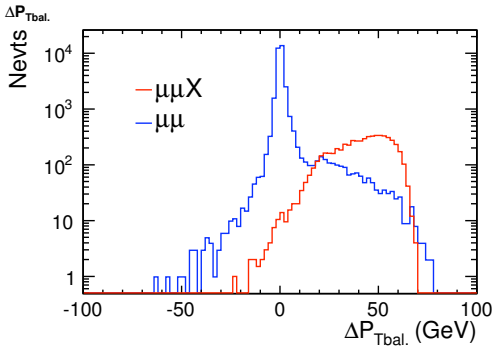

Figure 4.4: $\Delta P_{Tbal.}$ *distributions for background by* $e^+e^- \to \mu^+\mu^-$ *and signal in the* $\mu\mu X$*-channel.*

$e^+e^- \to \mu^+\mu^-\gamma(e^+e^-\gamma)$ which are undergoing final state radiation are suppressed by the requirement that the lepton pair should yield the Z boson mass.

A photon created by initial or final state radiation may convert in the passive material of the detector. Further rejection against lepton pair production can thus be achieved by determining the separation in polar angle of tracks other than the ones associated to the Z boson. Figure 4.5 shows this distance for signal events and background events in the $\mu\mu X$ channel. While the signal events are equally distributed in polar angle, the background events accumulate at $|\Delta\theta_{2\mathrm{tk}}| = 0$ as expected for electron-positron pairs from photon conversion. Therefore a further cut on $|\Delta\theta_{2\mathrm{tk}}| > 0.01$ is introduced. Albeit the analysis of additional tracks might introduce a certain model dependency, it can be considered as highly unlikely that a decay of the Higgs boson creates a topology leading to fermions being separated at a very small angle. Therefore, it can be concluded that the model independence is not compromised by this cut.

After the cuts discussed above, the background from fermion pair production is nearly entirely suppressed while about 95% of the signal is retained. The background

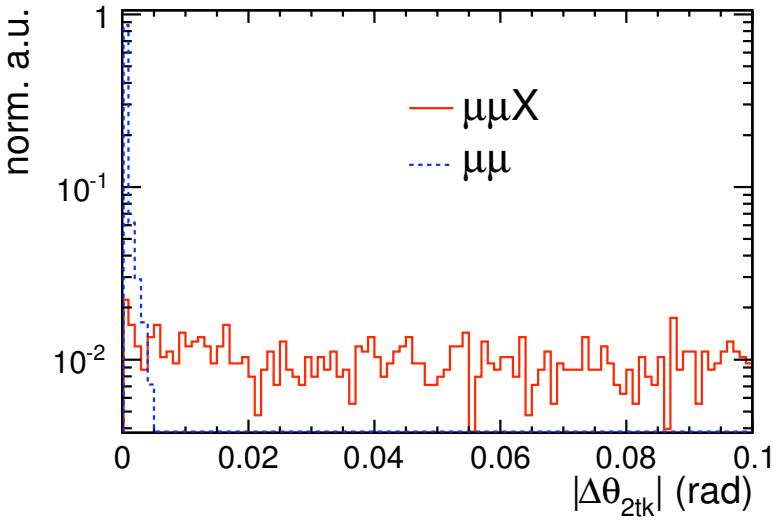

Figure 4.5: *Distribution of $\Delta\theta_{2tk}$, which is the $\Delta\theta$ between two additional tracks for $N_{add.TK} = 2$, for signal events ($\mu\mu X$) and background by muon pair production ($\mu\mu$).*

by events in which two bosons are produced, i.e. $e^+e^- \to ZZ/\gamma\gamma$ or $e^+e^- \to W^+W^-$, is less well distinguishable from the signal events. Further rejection can be achieved by a multi-variate analysis employing a set of suited discriminative variables. One example for these discriminative variables is the polar angle of the di-lepton pair. The production of Z boson and W boson pairs happens predominantly via exchange reactions which lead to a strong increase of the differential cross section towards large absolute values of the cosine of the polar angle. On the contrary, according to Equation 2.42 the Higgs-strahlung process is expected to decrease towards the forward and backward direction. Therefore the polar angle spectrum as shown in Figure 4.6 of the di-lepton system can be used to discriminate between signal events and background from Z and W pair production. Further variables employed in the multivariate analysis are the invariant mass M_{dl} of the di-lepton system its transverse momentum P_{Tdl} and its acollinearity, defined as $acol = \text{acos}(\mathbf{P}_{\ell^+}\mathbf{P}_{\ell^-}/|\mathbf{P}_{\ell^+}||\mathbf{P}_{\ell^-}|)$ After the multivariate analysis the overall signal selection efficiency is always larger than 35% and the signal over background ratio in the Higgs mass window $115 < M_{recoil} < 150\,\text{GeV}$ is always larger than 30%.

4.3 Extraction of Higgs Mass and the Higgs-strahlung Cross Section

In the previous section the criteria to select the signal events and to suppress the background from various sources have been introduced and applied. The remaining spectra are a superposition of signal and background events convoluted with beam

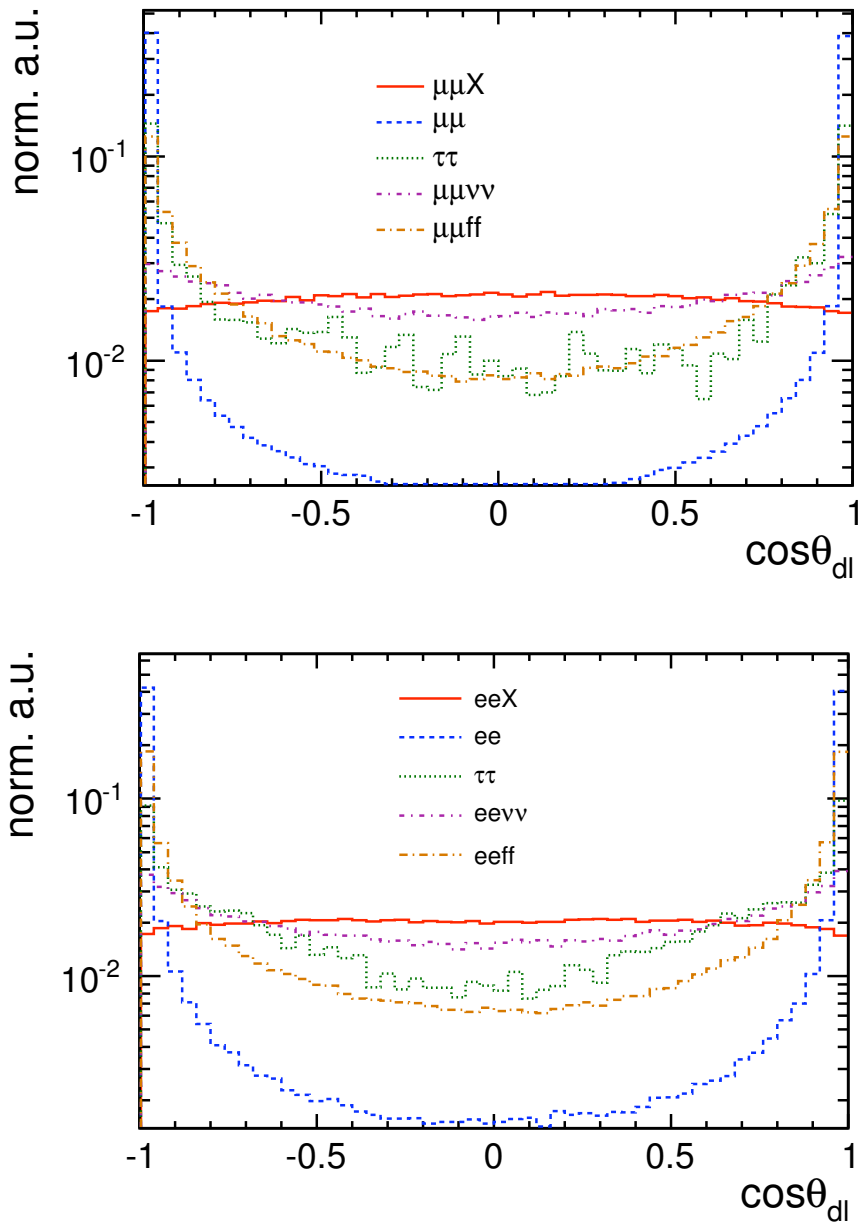

Figure 4.6: *Normalised signal and background distribution of the cosine of the polar angle* $\cos\theta_{\mathrm{dl}}$ *of the di-lepton system for the* $\mu^+\mu^- X$ *Channel (top) and the* $\mathrm{e}^+\mathrm{e}^- X$*-Channel (bottom). Here* $\tau\tau$ *refers to the* $\mu\mu$ *or* ee *created in the decay of* $\tau\tau$*.*

effects. In the following, the relevant observables as the Higgs boson mass m_{H} and the total Higgs-strahlung cross section σ_{HZ} are extracted. Note in passing, that the results for the eeX-channel will always contain a small admixture of the ZZ fusion process. The combination of signal and background is finally fitted by the sum of signal and background functions. The signal is approximated by a function based on *Kernel Estimation* [95, 96, 97] where the Kernel is given by a multi-gaussian distribution. The background on the other hand is approximated by a second order Chebyshev polynomial.

The result is displayed in Figure 4.7 for the $\mathrm{e}^-_{\mathrm{L}}\mathrm{e}^+_{\mathrm{R}}$ polarisation mode and in Figure 4.8 for the $\mathrm{e}^-_{\mathrm{R}}\mathrm{e}^+_{\mathrm{L}}$ polarisation mode. A clear maximum around the input value of $m_{\mathrm{H}} = 120\,\mathrm{GeV}$ is visible.

As expected, the signal is much more pronounced for muons that it is the case for electrons. The precision obtained for electrons suffers from bremsstrahlung which leads to migrations from the region around the maximum into the tail of large reconstructed masses. In addition, residual background from Bhabha Events as well as stronger background due to W pair production reduces the signal over background ratio in the eeX channel. The results are quantified in Table 4.4 and 4.5. While Table 4.4 shows the result of the model independent analysis, the Table 4.5 gives the result of a *Model dependent* analysis. Here, background from Bhabha events and W pair production can be entirely suppressed by requiring additional track activities as suggested when the Higgs boson decays into particles included in the Standard Model.

Pol.	Ch.	m_{H} (GeV)	σ_{HZ} (fb)
$\mathrm{e}^-_{\mathrm{R}}\mathrm{e}^+_{\mathrm{L}}$ $\mathcal{L} = 250\ \mathrm{fb}^{-1}$	$\mu^+\mu^- X$	120.006 ±(0.039)	7.89 ± 0.28 (3.55 %)
	$\mathrm{e}^+\mathrm{e}^- X$	120.005 ±(0.092)	8.46 ± 0.43 (5.08 %)
	merged	120.006 ±(0.036)	8.06 ± 0.23 (2.91 %)
$\mathrm{e}^-_{\mathrm{L}}\mathrm{e}^+_{\mathrm{R}}$ $\mathcal{L} = 250\ \mathrm{fb}^{-1}$	$\mu^+\mu^- X$	120.008 ±(0.037)	11.70 ± 0.39 (3.33 %)
	$\mathrm{e}^+\mathrm{e}^- X$	119.998 ±(0.085)	12.61 ± 0.62 (4.92 %)
	merged	120.006 ±(0.034)	11.96 ± 0.33 (2.76 %)

Table 4.4: *Resulting Higgs mass* m_{H} *and cross section* σ_{HZ} *of the* Model Independent *Analysis using* Kernel Estimation.

Pol.	Ch.	m_{H} (GeV)	σ_{HZ} (fb)
$\mathrm{e}^-_{\mathrm{R}}\mathrm{e}^+_{\mathrm{L}}$ $\mathcal{L} = 250\ \mathrm{fb}^{-1}$	$\mu^+\mu^- X$	120.008 ± 0.037	7.88 ± 0.26 (3.30 %)
	$\mathrm{e}^+\mathrm{e}^- X$	120.001 ± 0.081	8.46 ± 0.38 (4.49 %)
	merged	120.007 ± 0.034	8.06 ± 0.21 (2.66 %)
$\mathrm{e}^-_{\mathrm{L}}\mathrm{e}^+_{\mathrm{R}}$ $\mathcal{L} = 250\ \mathrm{fb}^{-1}$	$\mu^+\mu^- X$	120.009 ± 0.031	11.68 ± 0.32 (2.74 %)
	$\mathrm{e}^+\mathrm{e}^- X$	120.007 ± 0.065	12.58 ± 0.46 (3.66 %)
	merged	120.009 ± 0.028	11.97 ± 0.26 (2.19 %)

Table 4.5: *Resulting Higgs mass* m_{H} *and cross section* σ_{HZ} *of the* Model Dependent *analysis using* Kernel Estimation.

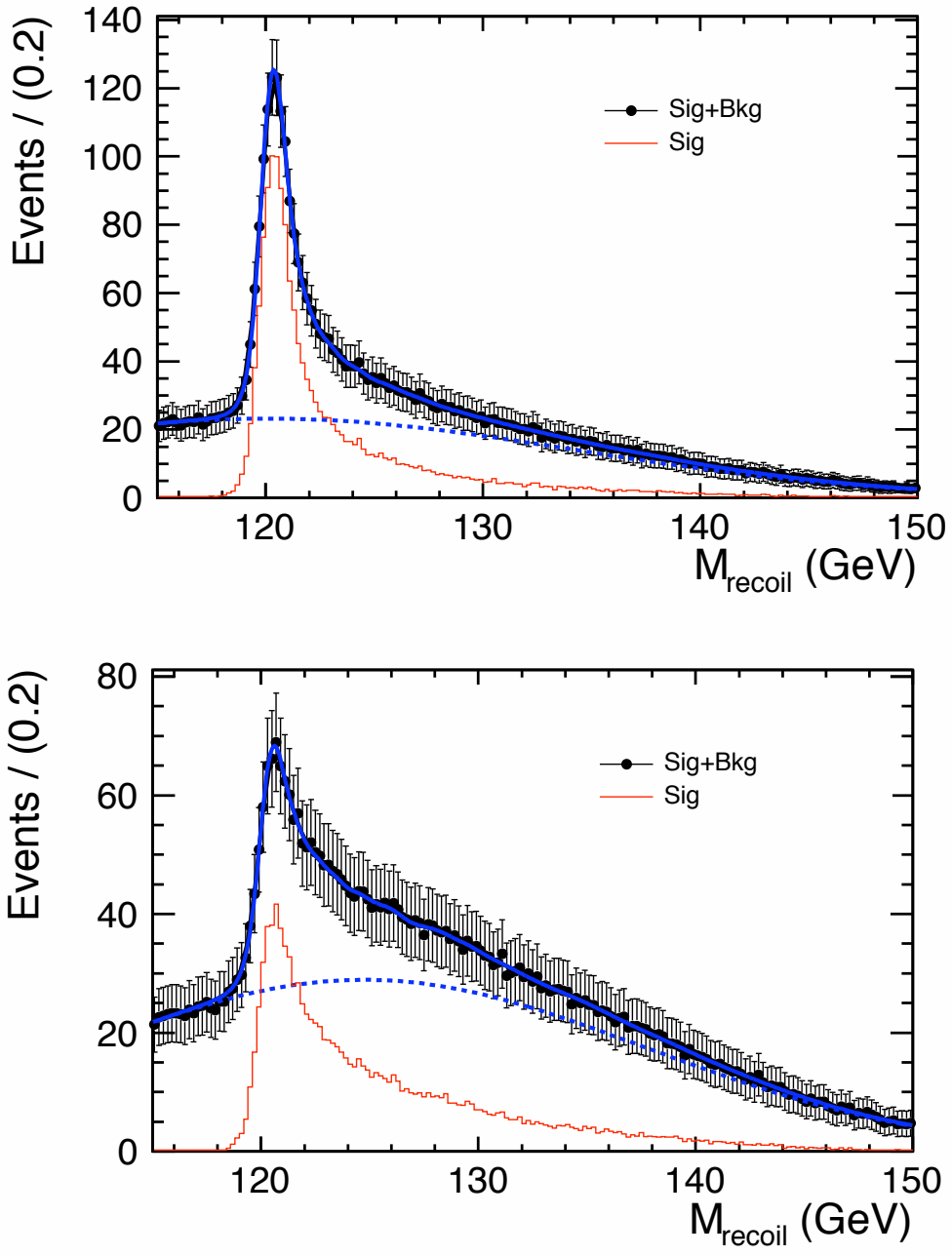

Figure 4.7: *Reconstructed Higgs mass spectrum together with the sum of underlying background for the* Model Independent Analysis *for the $\mu\mu X$-channel (top) and eeX-channel (bottom). The polarisation mode is $e^-_L e^+_R$. The lines show the fit based on* Kernel Estimation *to the signal and a polynomial of second order to the background as explained in the text.*

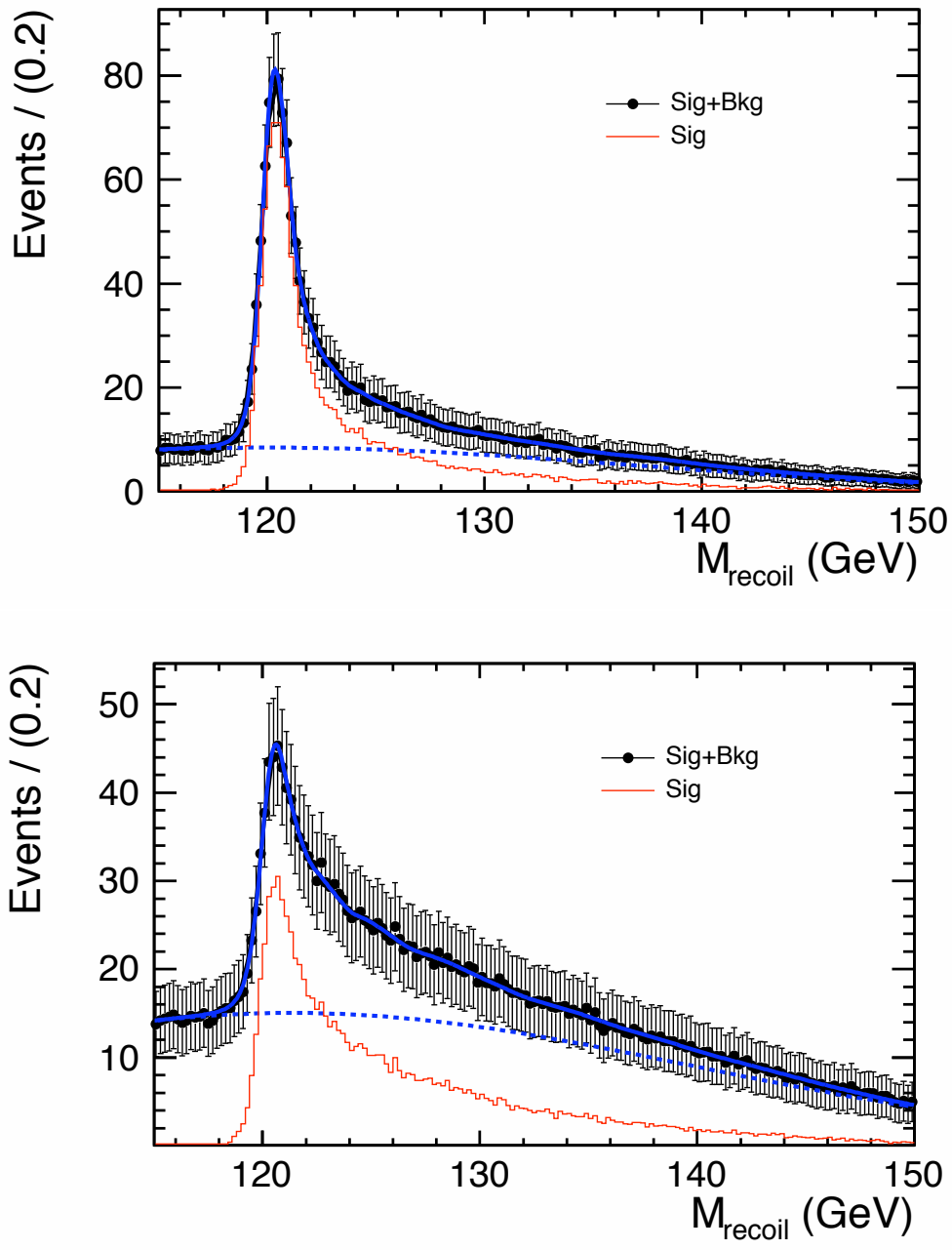

Figure 4.8: *Reconstructed Higgs mass spectrum together with the sum of underlying background for the* Model Independent Analysis *for the $\mu\mu X$-channel (top) and eeX-channel (bottom). The polarisation mode is $e^-_R e^+_L$. The lines show the fit based on a* Kernel Estimation *to the signal and a polynomial of second order to the background as explained in the text.*

The Higgs mass can be determined to a precision of the order of 0.03% when the eeX channel and the $\mu\mu X$ are combined. Regarding the individual results, it can be deferred that the precision in the $\mu\mu X$ channel is more than two times better than that of the eeX Channel. This increase of the error can mainly be attributed to bremsstrahlung of the electrons in the detector material. This can be concluded by comparing the corresponding results between Tables 4.4 and 4.5 as for the latter the background of Bhabha scattering and W pair production is suppressed. Still, the difference in the errors obtained for the eeX channel and the $\mu\mu X$ channel remains about the same.

The cross section of the Higgs-strahlung can be measured with a precision which is better than 3%. The difference between the $\mu\mu X$ channel and the eeX channel is smaller in this case since it is determined in a basically arbitrary mass window. The derived values for the Model Dependent Analysis are only slightly more precise. This relatively small difference of the results confirms that the methods employed for background suppression in the model independent analysis are already very efficient. For both, the mass determination and the cross section determination, no sizable influence of the beam polarisation mode on the resulting precision can be noticed.

In a final step, an attempt is made to improve the precision in the eeX channel by recovering the bremsstrahlung photons. The four-momenta of the selected electrons are combined with those of photons which have a small angular distance to the electrons. If these combined objects together with the corresponding other electron candidate yield the Z mass, they are included in the Z reconstruction. The inclusion of low energetic photons leads to a penalty in the momentum reconstruction due to the poor energy resolution of the electromagnetic calorimeter for low energetic particles. This drawback might get counterbalanced by the gain in statistics. The result after the recovery of bremsstrahlung's photons is given in Tables 4.6 and the fitted spectra in Figure 4.9. The numbers show that the mass resolution is improved by 10% while the precision in the cross section is improved by 20%. The cross section benefits directly from the gain in statistics while the determination of the recoil mass is compromised by the reduced momentum resolution.

Ana.	Pol.	m_{H} (GeV)	σ_{HZ} (fb)
MI	$e_R^- e_L^+$	120.003 ± 0.081	8.41 ± 0.36 (4.28 %)
	$e_L^- e_R^+$	119.997 ± 0.073	12.52 ± 0.49 (3.91 %)
MD	$e_R^- e_L^+$	119.999 ± 0.074	8.41 ± 0.31 (3.69 %)
	$e_L^- e_R^+$	120.001 ± 0.060	12.51 ± 0.38 (3.04 %)

Table 4.6: *Resulting Higgs mass m_{H} and cross section σ_{HZ} for the Model Independent analysis (MI) and Model Dependent (MD) analysis of the Higgs-strahlung process of e^+e^-X channel* after *bremsstrahlung photons recovery.*

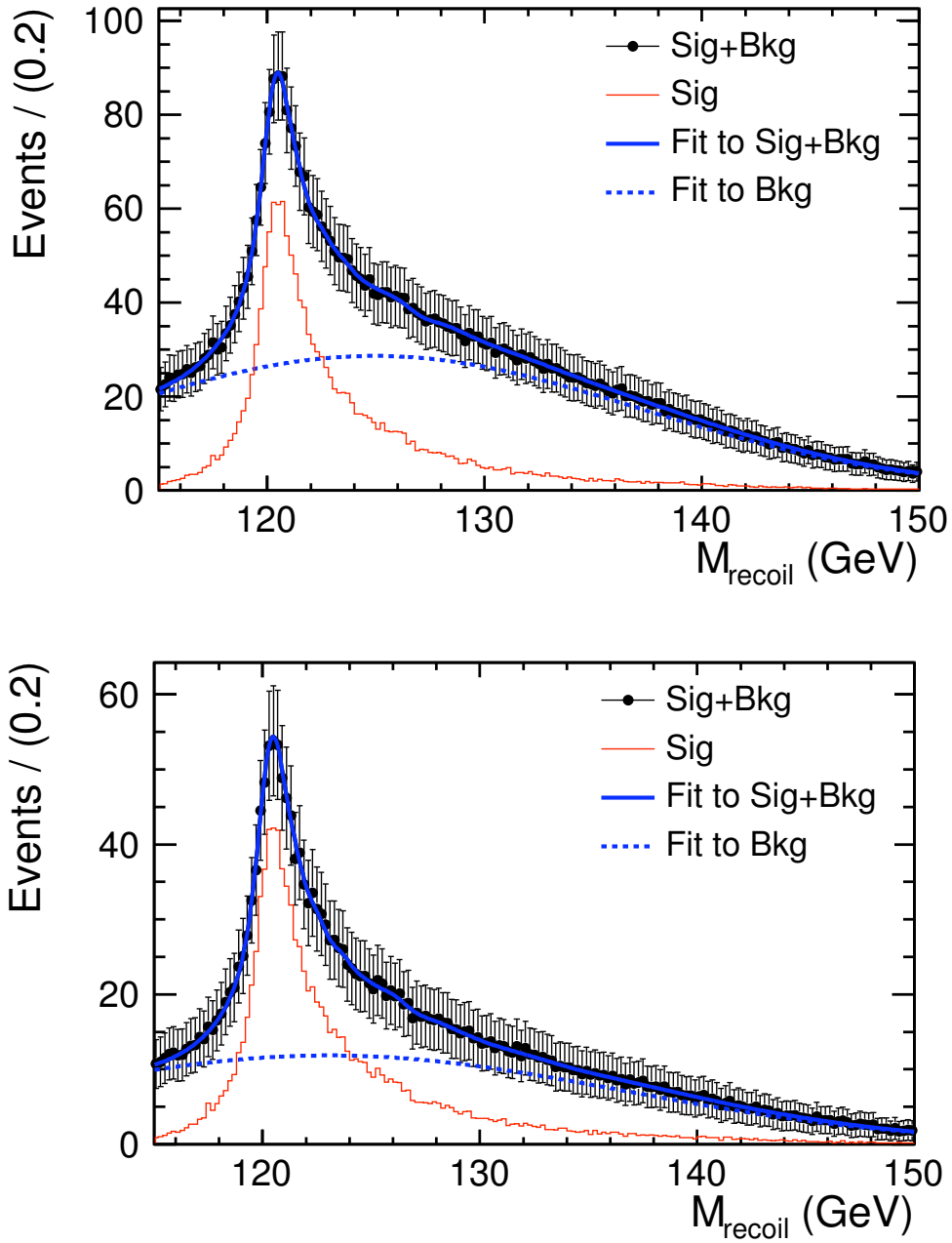

Figure 4.9: *Reconstructed Higgs mass spectrum* after the recovery of bremsstrahlung photons *together with the sum of underlying background for the* Model Independent *Analysis for the eeX-channel. The polarisation mode is* $e^-_L e^+_R$ *(top) and* $e^-_R e^+_L$ *(bottom). The lines show the fits based on a Kernel Estimation to the signal and a polynomial of second order to the background as explained in the text.*

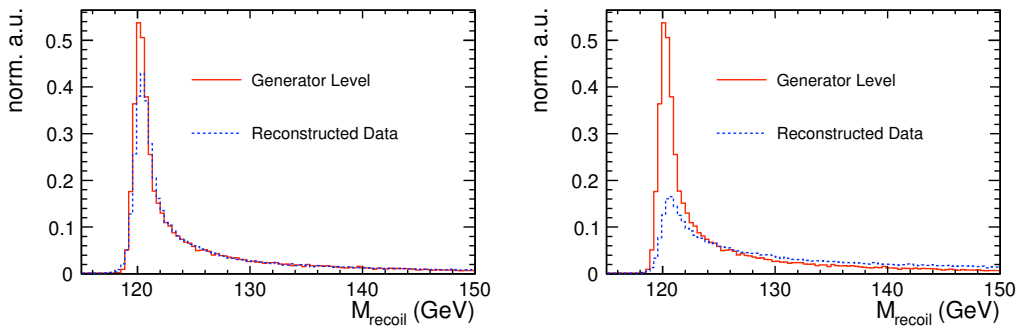

Figure 4.10: *Comparisons of recoil mass spectra in generator level and after full simulation, for the $\mu\mu X$-channel (left) and the eeX-channel (right).*

	$\Delta M_{tot.}$ (MeV)	$\Delta M_{mac.}$ (MeV)	$\Delta M_{dec.}$ (MeV)
$\mu\mu X$	650	560	330
eeX	750	560	500

Table 4.7: *Mass Resolution with contributions by machine ($\Delta M_{mac.}$) and detector ($\Delta M_{det.}$) separated.*

Influence of Beam Parameters

The width of the Higgs boson mass measurement is mainly given by a convolution of detector uncertainties and uncertainties on the energy of the incoming beams. Uncertainties on the energy of the incoming beams are imposed by accelerator components such as the initial linac, the damping rings or, in the case of electrons, by the undulator in the electron beam line. Another source of uncertainty is the beamstrahlung when particles of a beam bunch interact in the electromagnetic field of the opposite one. The Figure 4.10 shows the Higgs mass spectrum before and after full detector simulation. In particular for the $\mu\mu X$ channel, the detector response leads only to a small additional widening of the maximum of the recoil mass distribution. Using a Gaussian fit to the left side of the recoil mass distribution, its width before detector simulation can be quantified to be 560 MeV while it increases to 650 MeV for the $\mu\mu X$ channel after detector simulation, see Table 4.7. For the given configuration, the uncertainty on the incoming beams remains the dominant contribution to the observed width even for the eeX channel.

4.4 Discussion of Results

At the centre-of-mass energy of $\sqrt{s} = 250$ GeV and a luminosity of 250 fb^{-1}, the cross section σ_{HZ} of the Higgs-strahlung process with the Z boson decaying leptonically and a Higgs boson mass of 120 GeV as input, is determined to a precision of the order of 2-3% in the mass window $115 < m_{\mathrm{H}} < 150$ GeV. Due to the correspondence

$\sigma \sim g^2_{HZZ}$, this allows for the extraction of the coupling strength g_{HZZ} at the HZZ vertex to a precision between 1-2%. Due to the careful background reduction and the excellent mass resolution of up to 330 MeV, the signal to background ratio at the maximum of the Higgs mass peak is up to a factor 8 in the $\mu\mu X$ channel and up to a factor 5.5 in the eeX channel. With this excellent signal to background ratio, deviations as small as 15% from the Standard Model expectation could be established at the $5\,\sigma$ level. On the other hand, it provides to still see a signal even in case the cross section is reduced by a factor of about 10 due to new physics. It has been demonstrated semi-analytically [99] and confirmed with full simulation studies [98] that the precision can be further increased by working at a centre-of-mass energy closer to the HZ production threshold, i.e. at $\sqrt{s} = 230\,\text{GeV}$. This is also expected from the considerations in Section 2.5.

The mass of the Higgs boson can be determined to a precision of about 30 MeV. For the branch in which the Z boson decays into electrons, the precision is considerably compromised by bremsstrahlung in the passive material of the detector. This demands that the amount of passive material has to be carefully controlled during the detector design and construction phase. A future study clearly will have to quantify the systematic uncertainties and to identify those which have the largest influence on the systematic errors. This would give important directions on the final detector layout and the precision needed for e.g. alignment systems. For such a study realistic inputs on e.g. the uncertainty of drift times in the TPC or residual misalignments after detector movements are needed. It is finally important that the precision on the knowledge of the beam energy is kept at the envisaged 0.1% level.

The analysis has proved that the results are sensitive to details of the accelerator configuration. Using the set of parameters as has been chosen for the Letter of Intent studies which in turn correspond to the current best knowledge of the beam parameters, approximately half of the statistical error is generated by uncertainties caused by beam-strahlung and the energy spread of the incoming beams. The Higgs-strahlung process constitutes an important benchmark for the optimisation of the accelerator performance.

Chapter 5

Summary

This document reported on the preparational studies for a future linear electron positron collider. The most advanced proposal for such a machine is the International Linear Collider (ILC) which is designed for centre-of-mass energies between 90 GeV and 1 TeV. The document started with a review on precision experiments which lead to the formulation and the impressive confirmation of the Standard Model of particle physics. However, there is also a number of open question which the Standard Model is not able to answer. On the other hand, the discussed experiments gave important directions for the design of future experiments. Without too much simplification, it can be stated that the Higgs boson plays the most important role on the way to discover physics beyond the Standard Model. It is still undiscovered, but from the available data it can be inferred that its mass is of the order of 100 GeV when interpreting the data in the frame of the Standard Model or its minimal super-symmetric extension. One of the main goals of the proton-proton collider LHC which started operation in 2008 at CERN/Geneva is to discover the Higgs boson. At the ILC, as demonstrated in this document, the nature of the Higgs boson can be studied in a *model independent* way with an accuracy that is about 10 times higher than it will be possible at the LHC. The cross section for the production of a Higgs boson with a mass of 120 GeV via Higgs-strahlung can be measured at the ILC to a precision of 2-3%. The mass can be determined to a precision of 30 MeV. These results have been obtained with simulation studies of the ILD detector which is a validated proposal for a detector to be operated at the ILC. High precision measurements with the ILD detector will be based on Particle Flow. Its application needs highly granular calorimeters. The current baseline of the ILD detector design features a highly granular silicon tungsten (SiW) electromagnetic calorimeter with a lateral segmentation of $5 \times 5\,\mathrm{mm}^2$ and a longitudinal depth of $24\,\mathrm{X}_0$ subdivided into 30 layers. This design proposal is, however, still subject to an optimisation process. The whole SiW Ecal will comprise approximately 10^8 cells. Between the years 2005-2009 a physics prototype with 10000 cells built to demonstrate the principle of highly granular calorimeters was operated successfully in several large scale test beam campaigns. The physics prototype will be succeeded by a larger technological prototype which addresses technological challenges as for example the power pulsing of the front end electronics. From the operation of the physics prototype and the first steps towards the technological prototype, it can already be concluded that it will be feasible to operate a highly granular SiW Ecal in a detector for a linear collider. This conclusion is based on the following facts:

- The signal to noise ratio is of the order of 8 which is given the early stage of the R&D already very close to the envisaged goal of 10.

- The energy resolution is approximately $17\%/\sqrt{E}$ and the angular resolution is about $(100\,\mathrm{mrad})/\sqrt{E}$. These results confirm the values used in the Letter of Intent studies for the ILD detector. Future studies should put more emphasis on exploiting the highly granular structure of the device. The study of details of hadronic showers, presented briefly in this document, is one important step in that direction.

- By comparing data taken in different years at different locations, it could be demonstrated that the calibration is very stable over several years of operation. This is one of the key points required for the validation of the detector concepts.

- It will be possible to realise the challenging mechanics based on self-supporting alveolar structures which incorporate half of the tungsten absorbers. This was proved by the construction of a mechanical demonstrator.

- The readout electronics will be integrated into the layer structure of the calorimeter and has to integrate a multitude of tasks from first stage amplification until on-chip zero suppression and digitisation. The current status of the R&D shows that these challenging ASICs can be built. Preliminary studies indicate that the embedding of the ASICs into the layer structure will not compromise the precision measurements. One key design element for the ASICs is low power consumption. The goal is to achieve $25\,\mu$W/channel using power pulsing. Residual heat will be evacuated by a dedicated cooling system of which a first prototype was operated successfully in the context of the studies with the mechanical demonstrator.

- The technology for the silicon wafers is at hand. Shortcomings observed during the operation of the physics prototype like square events could be remedied by dedicated modifications of the guard rings which surround the silicon wafers.

The years until 2012 will see the step towards a *D*etailed *B*aseline *D*ocument (DBD) of the ILD detector. For this, the technological prototype will be subject of a large scale beam test program. The results of this beam test program will found the basis of the SiW Ecal design to be presented in this DBD. In particular, the results obtained during this and the past test beam data taking have to be incorporated into the simulation of physics channels for the DBD. The DBD will provide a solid basis for the detectors to complement the Technical Design Report of the accelerator. Both documents will constitute a costed and feasibility proved proposal for the ILC to be presented to the governments and will permit to plan the further steps towards the realisation of the ILC project. The DBD and the steps towards the realisation of the ILC project, particularly those for the detectors, will be accompanied by an intensive R&D program in which the SiW Ecal plays a

prominent role. The time schedule of the ILC and its detectors depends, however, very much on the first results from LHC as well as on political issues.

Appendix A

Beamparameters for ILC Operation Modes

Parameter	Symbol/Units	Calib.90	Nom.200	Nom.250	Nom.350	Nominal	Upgr.1TeV
Center of mass energy	$\sqrt{s}$ (GeV)	90	200	250	350	500	1000
Number of particles per bunch	N (10^{10})	2	2	2	2	2	2
Number of bunches per pulse	n_b	2625	2625	2625	2625	2625	2625
Bunch interval in the Main Linac	t_b	369.2	369.2	369.2	369.2	369.2	369.2
Average beam current in pulse	I_{ave} (mA)	8.7	8.7	8.7	8.7	8.7	8.7
Repetition rate	f_{rep} (Hz)	2.5	5	5	5	5	5
Electron polarization	(%)	N/A	80	80	80	80	80
Positron polarization[1]	(%)	N/A	30	30	30	30	30
Electron energy spread	(%)	0.70	0.35	0.28	0.20	0.14	0.14
Positron energy spread	(%)	0.50	0.25	0.18	0.10	0.07	0.07
Beta function at IP	β_x^* (mm)	75	26	22	20	20	30
Beta function at IP	β_y^* (mm)	2.0	0.6	0.5	0.4	0.4	0.3
R.M.S. beam size at IP	σ_x^* (nm)	3300	1200	950	760	640	550
R.M.S. beam size at IP	σ_y^* (nm)	35	13	10	7.4	5.7	3.3
R.M.S. bunch length	σ_z (μm)	300	300	300	300	300	300
Normalized emittance at IP	$\gamma\varepsilon_x^*$ (mm·mrad)	13	10	10	10	10	10
Normalized emittance at IP	$\gamma\varepsilon_y^*$ (mm·mrad)	0.054	0.056	0.053	0.047	0.040	0.036
Disruption parameter	D_x	0.03	0.13	0.15	0.17	0.17	0.11
Disruption parameter	D_y	3.3	11.4	14.0	17.5	19.1	18.9
Beamstrahlung parameter	Υ_{ave}	0.002	0.010	0.016	0.027	0.047	0.109
Beamstrahlung parameter	$\kappa = 2/(3\Upsilon_{ave})$	333.3	66.67	41.67	24.69	14.18	6.12
Energy loss by Beamstrahlung	δ_{BS}	0.0002	0.003	0.006	0.012	0.023	0.050
Number of Beamstrahlung photons	n_γ	0.26	0.74	0.89	1.09	1.29	1.43
Luminosity enhancement factor	H_D	1.9	1.8	1.7	1.7	1.7	1.5
Geometric luminosity	$\mathcal{L}_{geo}$ ($10^{34}\mathrm{cm}^{-2}\mathrm{s}^{-1}$)	0.018	0.28	0.42	0.74	1.1	1.8
Luminosity	$\mathcal{L}$ ($10^{34}\mathrm{cm}^{-2}\mathrm{s}^{-1}$)	0.033	0.47	0.71	1.2	1.9	2.8

[1]Although the baseline design only requires un-polarized positrons, the positron beam produced by the baseline source has a polarizatio n of ∼30%, and beamline space has been reserved for an eventual upgrade to ∼60% polarization.

Table A.1: *Beam parameters at interaction point (IP) [66].*

Appendix B

Calice Data Processing

The CALICE beam test effort is largely applying standard software available for ILC Detector studies. The whole data analysis is made in a data format compatible with the general ILC Software. Moreover, existing frameworks such as Marlin are employed for the CALICE software needs. The data management is entirely based on grid tools.

B.1 Introduction

Generally, the software concept for the processing of the CALICE data is driven by three main guidelines:

- Application of common ILC Software tools where possible and therefore benefiting from general developments of the ILC software. At the same time the application of these tools allow for the identification of the needs of the ILC Software for real data already at an early stage of the R&D phase.
- Since test beam data are taken at various locations they have to be available independent of the experimental site. Here, the grid was identified as the ideal tool to meet this goal. At the same time the grid offers significant computing resources needed for simulation and various re-processings of the data. In order to realise the data management and processing within the grid environment the virtual organisation (vo) calice has been established. As of today this vo counts 60 members.
- As many users as possible are to get involved in the analysis effort. Therefore, entry points for an easy start-up for unexperienced users have to be provided.

B.2 Data Management

Data as acquired by the CALICE data acquisition system are stored on a local buffer at the experimental site. Locally, these so called native files are used for debugging purposes and online monitoring of the data quality. A server of type Dell Poweredge 1950 is used for the online monitoring. At the same time, the server is configured as a grid user interface and transfers the data to a mass storage, see Fig. B.1, after the end of a run. The files are registered with their logical file names to the grid. By this, the data are available to the whole CALICE collaboration approximately 30 minutes after run end.

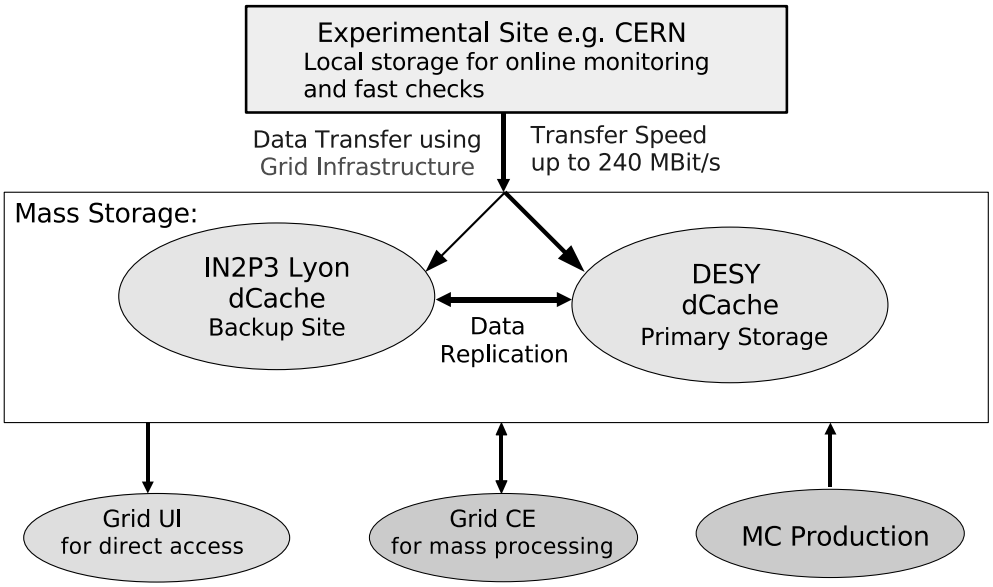

Figure B.1: *Data Management scheme as realised for CALICE Data. The DESY dCache is used as primary storage. Other main sites such as the Computing Center of the IN2P3 in Lyon/France hold replicas of the data or receive the primary copy in case of problems with the DESY mass storage during the data taking.*

The primary mass storage is the DESY dCache system [100]. Here, roughly 60 TBytes are available for CALICE. This is the amount of data collected by the end of 2009 which includes the native data files, simulated files as well as files produced during the data processing steps described in the next section. In addition to the mass storage at DESY similar storage space has been allocated at other sites. Among these sites, there are major computer centres which will hold complete replicas of the data. In total, 13 sites support CALICE with storage and computing resources.

B.3 Data Processing Scheme

Note, that the CALICE DAQ system is optimised for a maximal acquisition speed. For technical reasons, information belonging to an event appears at different places in the data stream.

To accommodate for that, the *native* data files are subject to a first processing step which acts as an event builder and provides first checks on the integrity of the data (see Figure B.2). This step is also called the *conversion* step since here the native data are converted into a format compatible with the general ILC Software. As the data are read out without zero suppression the size per event is mainly driven by the number of cells in the setup. For each cell the ADC value is stored as a 16 bit value. During the data taking in

2007 the complete setup including the analogue hadronic calorimeter, a Silicon-Tungsten electromagnetic calorimeter and a Tail Catcher and Muon Tracker comprised approximately 17000 cells leading to an event size of about 34 KBytes. By data compression, this size can be reduced by one third. During the conversion, a *database* is filled with detector configuration data and important conditions data such as e.g. temperatures and voltage settings. This database holds also other conditions data such as calibration constants and details of the experimental setup. This conversion step is entirely made on the grid which allows for a parallel conversion of several runs and therefore for a fast availability of the data. The converted *raw* data are available two hours after the end of a given run. These files can be processed using regular ILC Software tools. The raw data are then subject to a *reconstruction* step of which the main output is calibrated calorimeter hits and tracks as measured by tracking devices which are part of the test beam setup. The latter files can be used to examine algorithms developed for a full ILC detector simulation on the measured test beam data. Vice versa, digitisation algorithms developed for the test beam data and thus under realistic conditions, can be ported easily back into a full detector simulation.

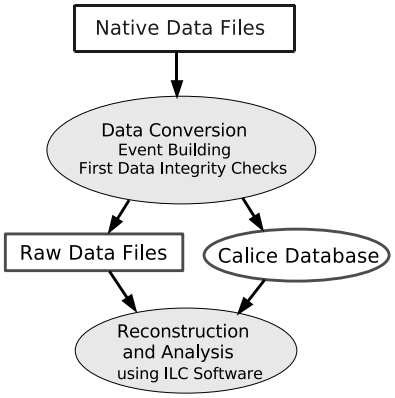

Figure B.2: *Overview on the processing chain for CALICE data.*

B.4 Conclusion

CALICE has established a full chain of data processing based in ILC Software and grid tools. This way of organising the software has lead to a wide spread analysis effort not restricted to the main detector experts. The strategy of using ILC Software tools will allow for a easy exchange between test beam results and results or algorithms obtained in general detector studies. This is in particular true for clustering algorithms which will be for the first time tested on data obtained with prototypes of ILC detectors. The CALICE collaboration will pursue this strategy throughout its running in 2007 and 2008.

The experience obtained during the CALICE data taking has clearly revealed the need for a dedicated treatment of data types more related to hardware issues. For the next generation test beams the interface between the DAQ systems and the offline processing has to be better defined. First efforts into this direction are already undergoing.

In total the processing and analysis of the CALICE test beam data delivers

important input to the development of the ILC software and computing environment with respect to technical aspects as well as for the development of Particle Flow Algorithms.

Bibliography

[1] F. Halzen, A.D. Martin.
Quarks and Leptons. J. Wiley & Sons Inc., ISBN 0-471-81187-4. 6, 29

[2] The Particle Data Group, *C. Amsler et al.*.
Review of Particle Physics. Phys.Lett.B667:1, 2008. 7, 22, 24, 27

[3] Gargamelle Neutrino Collaboration *F.J. Hasert et al.*.
Search for elastic muon neutrino electron scattering. Phys.Lett.B46:121, 1973. 7

[4] S.L. Glashow.
Partial Symmetries of Weak Interactions. Nucl.Phys.22:579, 1961. 8

[5] A. Salam.
Weak and Electromagentic Interactions. Proceedings of the Nobel Symposium, 1968. 8

[6] S. Weinberg.
A Model of Leptons. Phys.Rev.Lett. 19:1264, 1968. 8

[7] C. Jarlskog.
CP Violation. World Scientific Publishing, ISBN 9971505606, 2001. 9

[8] W. Heisenberg.
Über den anschaulichen Inhalt der quantentheoretischen Kinematik und Mechanik. Z.Physik 43 Nr.3:172, 1927. 11

[9] F. Wilczek.
Getting its from the Bits. Nature 397:303, 1999. 11

[10] J. Mnich.
Experimental tests of the standard model in $e^+e^- \to f\bar{f}$ *at the* Z *resonance.* Phys.Rep.271:181, 1996. 12

[11] The JADE Collaboration, *S. Hegner et al.*.
Final Results on Muon and Tau Pair Production by the JADE Collaboration at PETRA. Z.Phys.C43:547, 1990. 12

[12] The UA1 Collaboration, *G. Arnison et al.*.
Experimental Observation of Isolated Large Transverse Energy Electrons with Associated Missing Energy at $\sqrt{s} = 540\,\mathrm{GeV}$. Phys.Lett.B122:103, 1983. 12

[13] The UA2 Collaboration, *M. Banner et al.*.
Observation of Single Isolated Electrons of High Transverse Momentum in Events with Missing Transverse Energy at the CERN $\bar{p}p$ *collider.* Phys.Lett.B122:477, 1983. 12

[14] The UA1 Collaboration, *G. Arnison et al.*.
*Experimental Observation of Lepton Pairs of Invariant Mass Around 95*GeV/c^2 *at the CERN SPS Collider*. Phys.Lett.B126:398, 1983. 12

[15] The UA2 Collaboration, *P. Bagnaia et al.*.
Evidence for $Z^0 \to e^+e^-$ *at the CERN* $\bar{p}p$ *collider*. Phys.Lett.B129:130, 1983. 12

[16] LEP Design Report.
CERN-LEP/84-01.
R. Aßmann, M. Lamont, S. Myers for the LEP Team.
A brief history of the LEP Collider Nucl.Phys.B - Proceedings Supplements 109:17, 2002. 14

[17] *SLAC Linear Collider Conceptual Design Report*.
SLAC-R-229, Internal Report, SLAC 1980. 14, 54

[18] The ALEPH, DELPHI, L3, OPAL, SLD Collaborations,
The LEP Electroweak Working Group,
The Tevatron Electroweak Working Group,
The SLD Electroweak and Heavy Flavour Groups.
Precision Electroweak Measurements on the Z Resonance.
Phys.Rept.427:257, 2006, arXiv:hep-ex/0509008. 14, 16, 56

[19] The ALEPH, DELPHI, L3, OPAL, SLD Collaborations,
The LEP Electroweak Working Group,
The SLD Electroweak and Heavy Flavour Groups.
Precision Electroweak Measurements and Constraints on the Standard Model.
arXiv:0911.2604v1 [hep-ex]. 14, 25, 26, 48, 49

[20] The Particle Data Group, *W.M. Wao et al.*.
J.Phys.G.33:1, (2006) and 2007 partial upate for edition 2008.
`http://pdg.lbl.gov`. 17

[21] H1 and ZEUS Collaborations.
Combined Measurement and QCD Analysis of the Inclusive $e^{\pm}p$ *Scattering Cross Sections at HERA*. DESY 09-158, arXiv:0911.0884v1 [hep-ex]. 21

[22] The H1 Collaboration.
High Q2 Charged Current in polarised ep collisions. Contributed paper to ICHEP06 in Moscow.
`http://www-h1.desy.de/h1/www/publications/htmlsplit/H1prelim-06-041.long.html`. 20

[23] M. Jacquet.
Per mill level control of the Fabry-Perot cavity optical system for Precision Compton polarimetry. Memoire d'habilitation à Diriger des Recherches, LAL Orsay and Université Paris XI.

[24] F. Zomer *et al.*
A high precision Fabry-Perot Cavity polarimeter at HERA. Publication in preparation. 20

[25] Z. Zhang for the H1 and ZEUS Collaborations.
Electroweak Results from HERA. J.Phys.Conf.Ser.110:042034, 2008, arXiv:0801.4908v1 [hep-ph]. 20

[26] The H1 Collaboration, *A. Aktas et al.*.
Jet Production in ep Collisions at Low Q^2 and Determination of α_s. Submitted to Eur.Phys.J.C, arXiv:0911.5678 [hep-ex]. 19, 20

[27] The H1 Collaboration, *F. Aaron et al.*.
Jet Production in ep Collisions at High Q^2 and Determination of α_s. Accepted by Eur. Phys. J., arXiv:0904.3870 [hep-ex]. 21

[28] S. Bethke.
The 2009 World Average of $\alpha_s(m_Z)$ Eur.Phys.J.C 64:689, 2009 arXiv:0908.1135 [hep-ph]. 21

[29] S.W. Herb *et al.*.
Observation of a Dimuon Resonance at 9.5 GeV in 400-GeV Proton-Nucleus Collisions Phys.Rev.Lett.39:252, 1977. 22

24

[30] S.L. Glashow, J. Iliopoulos and L. Maiani.
Weak interactions with lepton-hadron symmetry. Phys.Rev.D2:1285, 1970. 24

[31] W.A. Bardeen.
Anomalous Ward Identities in spinor field theories. Phys.Rev.D2:1285, 1970. 24

[32] The CDF Collaboration, *F. Abe et al.*.
Observation of Top Quark Production in $\bar{p}p$ Collisions with the Collider Detector at Fermilab. Phys.Rev.Lett.74:2626, 1995, arXiv:hep-ex/9503002v2. 24

[33] The D0 Collaboration, *S. Abachi et al.*.
Observation of the Top Quark. Phys.Rev.Lett.74:2632, 1995, arXiv:hep-ex/9503003. 24

[34] The D0 Collaboration.
Measurement of the top quark mass in the lepton+jets channel using the matrix element method. D0 Note 5877-CONF, 2009. 25

[35] The D0 Collaboration.
Measurement of the W boson mass. Phys.Rev.Lett.103:141801,2009, arXiv:0908.0766v2 [hep-ex]. 25

[36] F. Mandl, G. Shaw.
Quantum Field Theory. J. Wiley & Sons Inc., ISBN 0-471-90650-6. 29

[37] M.W. Guidry.
Gauge field theories: An introduction with Applications. J. Wiley & Sons Inc., ISBN 0-471-90650-6. 29

[38] W.I. Mohar.
Gauge Theories, Solitons and Monopoles. Thesis for the degree of the Bachelor of Arts, Middlebury College, 2006. 31

[39] J. Goldstone, A. Salam and S. Weinberg.
Broken Symmetries. Phys.Rev.127, 965.
Y. Nambu. *Quasi-Particles and Gauge Invariance in the Theory of Superconductivity.* Phys.Rev.117, 648. 31

[40] K. Bleuler, Helv.Phys.Acta, v.23, rn.5, p.567-586, 1950
S. Gupta, Proc. Phys. Soc. v. A63, nr.267, p.681-691, 1950. 33

[41] P.W. Higgs.
Broken symmetries, massless particles and gauge fields. Phys.Letters.12:132, 1964. 33

[42] A. Djouadi.
The Anatomy of Electro-Weak Symmetry Breaking. I: The Higgs boson in the Standard Model. Phys.Rept.457:1-216, 2008, arXiv:hep-ph/0503172v2. 39, 43, 44, 45

[43] H. Georgi and S.L. Glashow.
Unity of All Elementary-Particle Forces. Phys.Rev.Lett.32:438, 1974. 38

[44] G.L. Kane.
Perspectives on Supersymmetry. World Scientific Publishing, ISBN : 981-02-35534, 1998. 40

[45] P. Binétruya and J.F. Grivaz.
Looking for physics beyond the Standard Model. C.R.Physique 3:1235, 2002. 40

[46] G.L. Kane.
Perspectives on Higgs Physics II. World Scientific Publishing, ISBN 981-02-3127, 1997. 40

[47] I. Simonsen.
A Review of Minimal Supersymmetric Electro-Weak Theory arXiv:hep-ph/9506369v2. 40

[48] M. Spira and P.M. Zerwas.
Electroweak Symmetry Breaking and Higgs Physics. Lect.Notes Phys.512:161 1998, arXiv:hep-ph/9803257v2. 43, 46

[49] B.W. Lee, C. Quigg and H.B. Thacker.
Strength of Weak Interactions at Very High Energies and the Higgs Boson Mass. Phys. Rev. Lett. 38:883, 1977. 46

[50] M. Carena, P.M. Zerwas (conv.) *et al.*.
Higgs Physics at LEP2. G. Altarelli, T. Sjöstrand and F. Zwirner (eds.), CERN Report 96–01 arXiv:hep-ph/9602250. 43

[51] J. Ellis *et al.*.
The Probable Fate of the Standard Model. Phys.Lett.B679:369, 2009, arXiv:0906.0954v2 [hep-ph]. 48

[52] V. Branchina and H. Faivre.
Effective potential (in)stability and lower bounds on the scalar (Higgs) mass. Physical Review D 72 (2005) 065017. 48

[53] The Higgs Working Group at Snowmass '05, *S. Heinemeyer et al.*.
Toward High Precision Higgs-Boson Measurements at the International Linear e^+e^- *Collider.* ECONF C0508141:ALCPG0214,2005; ECONF C0508141:PLEN0044,2005, arXiv:hep-ph/0511332v2. 48

[54] The ALEPH, DELPHI, L3, OPAL collaborations.
Search for the Standard Model Higgs Boson at LEP. Phys.Lett.B565:61 2003, arXiv:hep-ex/0306033.

[55] The CDF and D0 collaborations.
Combined CDF and D0 Upper Limits on Standard Model Higgs-Boson Production with 2.1 - 5.4 fb-1 of Data. FERMILAB-CONF-09-557-E, arXiv:0911.3930v1 [hep-ex]. 49

[56] K. Wille.
Physik der Teilchenbeschleuniger und Synchrotronstrahlungsquellen. Teubner Studienbücher Physik, ISBN 5-519-03087-X, 1992. 53

[57] A.W. Chao and M. Tigner.
Hanbook of Accelerator Physics and Engeneering World Scientific Publishing, ISBN 9810235005, 2002. 53

[58] W.R. Leo.
Techniques for Nuclear and Particle Physics Experiments Springer Verlag, ISBN 0-387-17386, 1992. 53

[59] C. Grupen.
Teilchendetektoren. B. I. Wissenschaftsverlag. 53

[60] International Technology Recommendation Panel.
Final International Technology Recommendation Panel Report. Available from
http://www.ligo.caltech.edu/~BCBAct/ITRP_home.htm. 54

[61] *TESLA Design Report.*
Available from
http://tesla.desy.de/new_pages/TDR_CD/start.html. 54, 58

[62] ILC Global Design Effort and World Wide Study.
International Linear Collider Reference Design Report. Available from
http://www.linearcollider.org/cms/?pid=1000437. 54, 56

[63] ILC Home Page.
http://www.linearcollider.org/. 56

[64] E166 Collaboration, *G. Alexander et al.*.
Observation of Polarized Positrons from an Undulator Based Source. Phys.Rev.Lett.100:210801, 2008. 56

[65] E166 Collaboration, *G. Alexander et al.*.
Undulator-Based Production of Polarized Positrons. Nucl.Instr.Math.A610:451, 2009. 56

[66] Discussion Session at TILC08. *Luminosity as function of L* – A.Seryi, and discussion of corresponding detector optimization – all.* http://ilcagenda.linearcollider.org/contributionDisplay.py?contribId=113&sessionId=9&confId=2432. 118

[67] M. Battaglia *et al.*.
Physics at the CLIC Multi-TeV Linear Collider : report of the CLIC Physics Working Group. CERN-2004-005, arXiv:hep-ex/0412251. 56

[68] M.A. Thomson.
Particle Flow Calorimetry and the PandoraPFA Algorithm. Nucl.Instrum.Meth.A611:25, 2009, arXiv:0907.3577v1 [physics.ins-det]. 58, 61

[69] J.C. Brient and H. Videau.
The calorimetry at the future e^+e^- *linear collider.* eConf C010630 E3047 2001, LLR-02-001, arXiv:hep-ex/0202004v1. 58

[70] V. Morgunov. *Private communication.* 58

[71] The ILD Concept Group.
The International Large Detector – Letter of Intent. Available from
http://www.ilcild.org/documents/ild-letter-of-intent/LOI.pdf. 59

[72] The International Detector Advisory Group.
IDAG Report on the validation of Letters of Intent for ILC detectors. Available from
http://ilcdoc.linearcollider.org/record/23970/files/IDAG_report_090816.pdf. 59

[73] The SiD Concept Group.
The Silicon Detector – Letter of Intent. Available from
http://silicondetector.org/download/attachments/46170132/SiliconDetectorLetterOfIntent.pdf?version=1. 59

[74] M. Reinhard and J.C. Brient.
GARLIC - Gamma reconstruction for the Linear Collider. Proceedings of LCWS08, arXiv:0902.3042v1 [hep-ex]. 61

[75] CALICE Collaboration.
https://twiki.cern.ch/twiki/bin/view/CALICE/WebHome. 63

[76] The CALICE Collaboration, *J. Repond et al.*.
Design and Electronics Commissioning of the Physics Prototype of a Si-W Electromagnetic Calorimeter for the International Linear Collider. JINST 3:P08001 2008, arXiv:0805.4833v1 [physics.ins-det]. 64, 71, 91

[77] The GEANT4 Collaboration.
GEANT4 - A Simulation Toolkit Nucl.Instr.Meth.A506:250, 2003.
IEEE Transactions on Nuclear Science 53 No. 1 (2006) 270. 64

[78] The CALICE Collaboration, *J. Repond et al.*.
Response of the CALICE Si-W Electromagnetic Calorimeter Physics Prototype to Electrons. Nucl.Instr.Meth A608:372, 2009, arXiv:0811.2354v1 [physics.ins-det]. 67

[79] H. Li.
Higgs Recoil Mass and Cross-Section Analysis at ILC and Calibration of the CALICE SiW ECAL Prototype. PhD Thesis Université Paris Sud XI and LAL Orsay, LAL 09-118. 70, 97

[80] M. Faucci-Giannelli.
Position and Angular Resolution of the SiW Ecal Prototype. Calice Analysis Note, in preparation. 70

[81] The Group within CALICE working on the SiW Ecal Technological Prototype, *M. Anduze et al.*.
JRA3 Electromagnetic Calorimeter Technical Design Report. EUDET-Report-2009-001. 76

[82] C.Y. Ho, R.W. Powell, P.E. Liley (NSRDS).
J.Phys.Chem.Ref.Data 1 (1972).
Update: http://www.wittrock-web.de/pse_leit_th.html. 80

[83] R. Cornat.
Design of a SiW electromagnetic calorimeter for the International Linear Collider and study of cross talk in silicon sensors. Proceedings of the NSS-MIC 2008 Conference, Dresden, Germany. 84

[84] J. Rouëne *in collaboration with V. Vandenbussche, M Faucci-Giannelli, R.Pöschl and the Omega Group at LAL.*
Analyse du Comportement de l'électronique frontale d'un Prototype pour le calorimètre électromagnétique du futur accélérateur lineaire (ILC). Rapport de Stage de L3. 87

[85] C. de la Taille.
Front End Electronics in Calorimetry: From LHC to ILC. Mémoire d'habilitation à encadrer des recherches. LAL-09-117. 87, 89

[86] The Higgs Working Group at Snowmass '05 *S. Heinemeyer et al.*.
Towards High Precision Higgs-Boson Measurements at the International Linear e^+e^- *Collider.* arXiv:hep-ph/0511332. 97

[87] W. Lohmann *et al.*.
Prospects to Measure the Higgs Boson Mass and Cross Section in $ee \to ZH$ *Using the Recoil Mass Spectrum.* arXiv:0710.2602v1 [hep-ex]. 97

[88] M. Ruan *et al.*.
A precision determination of Higgs mass using the fully simulated Higgs-strahlung process $e^+e^- \to hZ \to h\mu\mu$ *at ILC.* CARE-Note-2008-0013-ELAN 97

[89] M. Battaglia *et al.*.
Physics Benchmarks for the ILC Detectors. arXiv:hep-ex/0603010v1 (March 2006). 97

[90] H. Li *et al.*.
HZ Recoil Mass and Cross Section Analysis in ILD. LC-PHSM-2009-006.
Available from http://www-flc.desy.de/lcnotes/. 97

[91] W. Kilian, T. Ohl, J. Reuter.
WHIZARD: Simulating Multi-Particle Processes at LHC and ILC. arXiv:0708.4233 [hep-ph]. 98

[92] http://ilcsoft.desy.de. 98

[93] D. Schulte.
GUINEA-PIG - An e^+e^- *beam simulation program.* PhD Thesis University of Hamburg (1996). 98

[94] J.C. Brient.
Measurement of the Higgs Mass and $e^+e^- \rightarrow ZH$ *cross sections at Linear Colliders*. LC-PHSM-2000-049. 99

[95] K. S. Cranmer.
Kernel Estimation for Parametrization of Discriminant Variable Distributions. ALEPH 99-144, PHYSIC 99-05 (1999). 106

[96] K. S. Cranmer.
Kernel estimation in High-energy physics. Comput.Phys.Commun.136:198, 2001, hep-ph/0005309. 106

[97] The OPAL Collaboration.
Search for Neutral Higgs Bosons in e^+e^- *Collisions at* $\sqrt{s} \approx$ *192–202 GeV*. OPAL PHYSICS NOTE PN426 (2000). 106

[98] H. Li *et al.*.
Precision Measurements of SM Higgs Recoil Mass and Cross Section for Ecm of 230 GeV and 250 GeV at ILC. Proceedings of the Linear Collider Workshop 2008 at Chicago, arXiv:0901.4893v3 [hep-ex] (2009). 112

[99] P. Bambade and F. Richard.
Strategies to measure the Higgs mass, width and invisible decays at ILC. arXiv:hep-ph/0703173 (2007). 112

[100] P. Fuhrmann and V. Gülzow.
dCache Storage System for the Future. Conference Proceedings Europar, Dresden, 2006.
See also `http://www.dcache.org/manuals/index.shtml`. 120